

Origami Metamaterials:

Design, Symmetries, and Combinatorics

Proefschrift

ter verkrijging van
de graad van Doctor aan de Universiteit Leiden,
op gezag van Rector Magnificus prof. mr. C.J.J.M. Stolker,
volgens besluit van het College voor Promoties
te verdedigen op dinsdag 16 oktober 2018
klokke 15.00 uur

door

Peter Dieleman
geboren te Rotterdam
in 1990

PROMOTOR

Prof. dr. M.L. van Hecke

PROMOTIECOMMISSIE

Dr. A. Murugan (*Universiteit van Chicago, Chicago, VS*)

Dr. ir. J.T.B. Overvelde (*AMOLF, Amsterdam*)

Prof. dr. P.M. Reis (*EPFL, Lausanne, Zwitserland*)

Prof. dr. J. Aarts

Prof. dr. ir. S.J. van der Molen

Prof. dr. H. Schiessel

Casimir PhD Series, Delft-Leiden, 2018-32

ISBN 978-90-8593-361-8

An electronic version of this thesis can be found at openaccess.leidenuniv.nl

Supporting images and files can be found at http://bit.ly/supplemental_files or via the QR codes printed in the margin of this thesis.

The work described in this thesis was supported by the Stichting voor Fundamenteel Onderzoek der Materie (FOM), presently part of NWO.

The cover shows one of the combinatorial fold patterns described in this thesis (p. 60). Depending on how you fold it, this crease pattern folds up into the shape of the Greek letter ' α ', or the into the shape of the Greek letter ' ω '.

Contents

1	Introduction	1
1.1	Origami	1
1.2	Rigid Folding	5
1.2.1	Single Crease	5
1.2.2	Rigidly Folding Vertices	6
1.2.3	4-Vertex Fold Patterns	8
1.3	This Thesis	9
2	Discrete Origami Tiles	11
2.1	Introduction	11
2.2	Rigid Folding Conditions	12
2.3	Combinatorial Loop Condition	13
2.4	Tiles	16
2.5	Bricks	18
2.6	Summary and Outlook	23
3	Classification of Tile Patterns	25
3.1	Introduction	25
3.2	Triplet Completion and Classification	27
3.3	Counting Multiplicity of Tilings	29
3.4	Counting Supplementation Patterns	36
3.5	Counting Folding Branches	44
3.6	Summary and Outlook	48

CONTENTS

4	Rational Design of Origami Patterns	51
4.1	Introduction	51
4.2	Space-Filling Tilings	52
4.3	Designing Origami Strips with One Target Shape	53
4.4	Designing Origami Sheets with Two Target Shapes	57
5	Multistability of Non-Flat Vertices	63
5.1	Introduction	63
5.2	Non-Flat 4-Vertices	64
5.2.1	Phenomenology	64
5.2.2	Theoretical Energy Curves	69
5.3	3D Printed Tristable Vertices	71
5.4	Experimental Results	74
5.4.1	Tristable Vertex: Qualitative Results	74
5.4.2	Experimental Protocol for Torsion Experiments	75
5.4.3	Torsion Experiments - Results	79
5.4.4	Experimental Energy Curves	88
5.4.5	Vertex Pop-Through	92
5.5	Conclusion	98
A	Fold Angles	99
B	4-Vertex as a Spherical Mechanism	103
	Samenvatting	115
	Summary	119
	Publication List	123
	Curriculum Vitae	125
	Acknowledgments	127

INTRODUCTION

1.1 Origami

Folding paper for decorative purposes is an art that seems to have developed separately in different parts of the world [1, 2], but is now known worldwide by the Japanese word ‘origami’, meaning: ‘folding paper’. Origami in Japan is thought to originate from the folding of ceremonial wrappers during the 14th century [1], and evolved in complexity over the subsequent centuries (Fig. 1.1.A). Folding paper in Europe seems to stem from the 16th century, as a way to make baptismal certificates [1] (Fig. 1.1.B), and was later also used for decorative purposes, for example, to elaborately fold napkins (Fig. 1.1.C). Up until 1854, when the United States and Japan signed the Kanagawa treaty [6], there was very little mixing of the Western and Japanese traditions of paper folding [1, 2]. The modern day interpretation of ‘origami’ is a result of the mixing of these two traditions after the modernization of Japan during the second half of the 19th century [1].

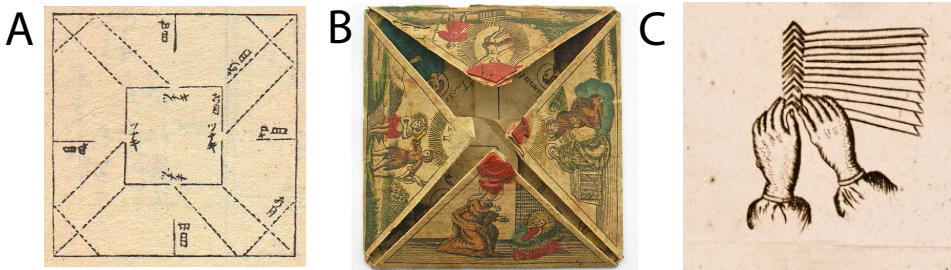


FIGURE 1.1: (A) Origami Fold pattern from a 1797 Japanese book [3]. (B) German ‘Patenbrief’ (baptism certificate), dated 1769. (C) Instructions on decoratively folding napkins from a 1754 Dutch cooking book [4]. Figures from [5].

In the 1950s, the development of a standard way to draw origami diagrams allowed for more efficient sharing of origami models [7]. At the same time, mathematicians started to get interested in the mathematics behind paper folding, starting with the 1949 book ‘Geometric Tools’ [8]. Since then, mathematicians have found a variety of necessary conditions which crease patterns should satisfy in order to fold, first at the level of single vertices [9, 10], and later at the level of folding patterns [11–16].

Building on these mathematical rules, and benefiting from the increasing popularity of computers, emerged the field of ‘computational origami’. The first major breakthrough in this field was an algorithm named ‘Treemaker’ developed by Robert Lang, first released in 1993 [17]. This program finds a two-dimensional fold pattern for a given three-dimensional shape, allowing for the design of very complex origamis. A different and more sophisticated algorithm was developed by Tomohiro Tachi [18, 19]. An example of the capability of this latter algorithm is shown in Fig. 1.2.A, where we depict a complicated two-dimensional folding pattern designed to fold into the shape of a ‘Stanford Bunny’, containing 374 triangles [19]. Fig. 1.2.B displays a three-dimensional, manually folded version of this crease pattern, made out of paper.

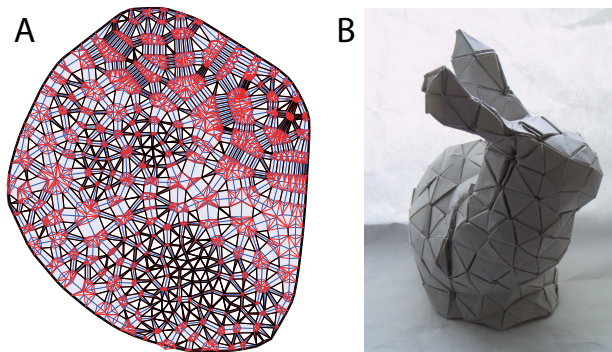


FIGURE 1.2: (A) 2D crease pattern, containing 374 triangles, designed to fold into the shape of a ‘Stanford Bunny’. (B) Paper folded into the shape of a Stanford Bunny according to the crease pattern in (A). Figure adopted from [19].

The most recent wave of interest in origami comes from the fields of physics and engineering. This interest can be traced back to the 1960s, when engineers started to consider origami based materials for structural

applications. Specifically, various patents were filed for so called ‘folded sandwich core’ panels [20, 21]. These panels consist of a sheet of material folded in a ‘double corrugated shape’, glued onto a skin on the top and the bottom (Fig. 1.3). Designs such as these promised to outperform ‘classic’ honeycomb sandwich core panels in terms of transversal shear stiffness for the same weight [22, 23], but proved impractical at the time, due to the sensitivity to fabrication imperfections [24, 25]. However, advances in fabrication processes have renewed interest in these materials, giving rise to a large number of experimental and numerical studies [23].

More recently, it has been shown that origami inspired materials can exhibit a variety of exotic properties, ranging from a negative Poisson’s ratio [26], to tuneable stiffness [27], to multistability [28]. In addition, origami can serve as a low-cost manufacturing platform for the fabrication of simple robots [29–31]. Here, we will show some examples of these exotic properties.

One example is the folded core of the panel in Fig. 1.3, which is also shown in Fig. 1.4.A. Here it is demonstrated that this sheet has a negative 2D-Poisson’s ratio, as it shrinks in both planar directions simultaneously. This property can be harnessed by stacking multiple sheets to make a 3D origami structure that can contract (or expand) in all three orthogonal directions simultaneously, which is impossible with a regular (positive Poisson’s ratio) solid [26, 32]. This pattern is now called the “Miura-ori” pattern, named after K. Miura, who proposed it as an effective way to pack and deploy large membranes for space-flight, as it can unfold with a single continuous motion, using a minimal amount of motors [33].

This Miura pattern –as well as derivatives– have since been extensively

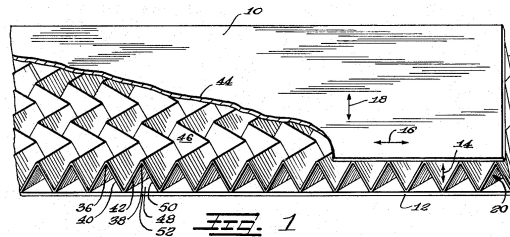


FIGURE 1.3: Patent filing for a folded core sandwich panel, figure adapted from [20].

studied, and a host of other interesting properties have been discovered; such as multistability [28], arbitrary shape change [34], and the ability to reversibly program the stiffness of a sheet [27, 35]. For example, in [27] it is shown that it is possible to pop-through a single unit cell of the Miura pattern in its folded configuration, introducing a so-called ‘pop-through defect’. The presence of these pop-through defects can change the compressive stiffness of the sheet, as the fold pattern is locally frustrated. In some cases however, two adjacent pop-through defects can interact in such a way as to generate a lattice vacancy. These lattice vacancies give rise to various crystallographic structures, such as grain boundaries, and edge dislocation – an example of the latter is shown in Fig. 1.7.B [27].

Additionally, fold patterns seem to be ubiquitous in nature, appearing naturally in leaves [37–39], insect wings [40, 41], and in embryonic gut tissue in chicks [36]. This natural occurrence is attributed to the material growing within a constrained environment [38, 42]. For example, when the gut-tube of an embryonic chick is developing it is initially smooth, but when the development of circumferentially oriented muscle tissue starts, inward buckling of the tube prompts the formation of ridges in the longitudinal direction. A second layer of *longitudinally* oriented muscle then starts to develop several days later, after which the longitudinal ridges themselves buckle into parallel zigzags [43], leading to the pattern shown in Fig. 1.4.C.

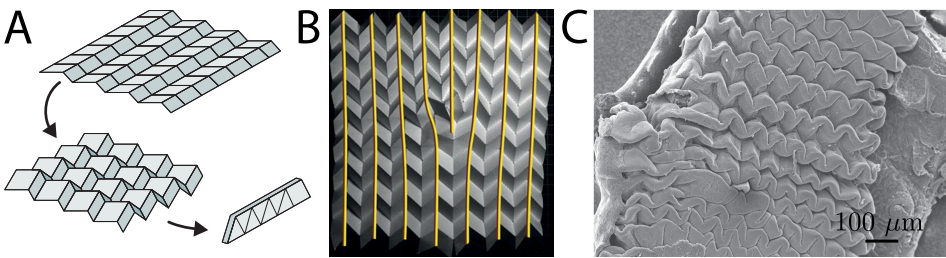


FIGURE 1.4: (A) A Miura-ori pattern shows auxetic (negative Poisson’s ratio) behavior. (B) Multiple pop-through defects in a column of a Miura-ori sheet give rise to an edge dislocation [27]. (C) SEM picture of turkey gut, showing a fold structure resembling the Miura-ori pattern. Panel (A) adapted from [32], panel (B) adapted from [27], panel (C) adapted from [36].

1.2 Rigid Folding

In this section I will explain the concept of *rigid* folding, which is central to understanding the work in this thesis. In addition, I will explain what this means in the case of a single 4-vertex, and for patterns consisting of multiple 4-vertices.

1.2.1 Single Crease

The simplest possible origami pattern that we can study is a single crease, which already turns out to have interesting mechanics. When applying a crease to a piece of material, we plastify some of the bonds in the paper, such that their rest positions are no longer flat. When we then pull the material outward we effectively open the crease, which then acts as a torsional spring. Additionally, the sheet itself may deform and bend. The length scale that determines which of these elastic effects dominates, is called the origami length scale [44]:

$$L^* = \frac{B}{\kappa}. \quad (1.1)$$

Here B is the bending modulus, $B = Eh^3/12(1 - \nu^2)$, E is the Young's modulus, ν is the Poisson's ratio, and h the thickness of the material. κ is defined as the effective torsional stiffness of the crease. Based on the energy stored in a single crease, it can be shown that the torsional stiffness should scale roughly as $\kappa = B/h$ [45]. The length scale L^* therefore linearly increases with the thickness of the material h . Experiments in [44] for Mylar sheets show that there is a large separation of scales between h and L^* .

This separation of scales can be explained by a separation of scales between the Young's modulus of the material, which sets B in Eq. 1.1, and the yield stress σ_Y , which sets κ in Eq. 1.1. The existence of this difference allows for the following two scenarios: sheets with a fold pattern where the length of the creases, l , is larger than L^* , and sheets whose crease length l is smaller than L^* . This difference can be demonstrated by folding a sheet of material into an accordion shape, such as shown in Fig. 1.5. In the case $l > L^*$ extending the sheet will not change the angle between the plate very much from its rest angle ($\phi \approx \phi_0$), but instead will bend the plates (Fig. 1.5.B). In the case $l < L^*$ the deformation is concentrated in the crease,

which acts as an approximately linear torsional spring, and the panels stay almost completely straight (Fig. 1.5.D) [44]. In the scenario where $l < L^*$ we can therefore approximate a fold pattern by a set of hinges, dressed with torsional springs, connecting rigid plates – this is the rigid folding limit.

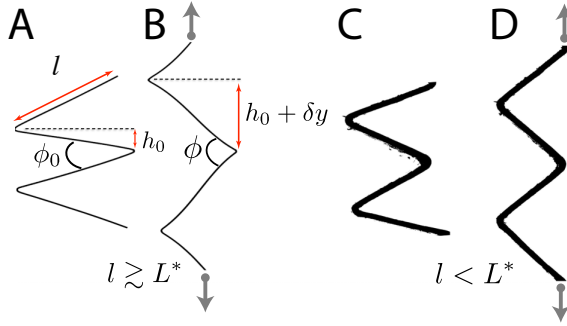


FIGURE 1.5: Side view of two sheets of Mylar with thickness $h = 130 \mu\text{m}$, folded into an accordion shape (A,C), and extended by pulling on the top and bottom (B,D). (A) Rest state with $l = 2.5 \text{ cm}$. (B) Deformed state. (C) Rest state with $l = 0.6 \text{ cm}$. (D) Deformed state. $L^* \approx 2.5 \text{ cm}$. Figure adapted from [44].

1.2.2 Rigidly Folding Vertices

The fold pattern shown in Fig. 1.5 is a very simple one, consisting of parallel lines. Most fold patterns are more complicated than this, and also contain *vertices*, i.e. points where multiple folds come together (see Fig. 1.4.A,B). It is therefore important to understand what happens at these vertices. If we assume the rigid folding condition, where the plates are perfectly rigid, we can use 3D Maxwell-Calladine constraint counting to count the number of floppy modes of a single vertex [46, 47].

In the case of a vertex where three lines come together (shown in blue in Fig. 1.6.A), we count $4 \times 3 = 12$ degrees of freedom (d.o.f.) for the 4 points in 3D space. These points cannot freely move, but are constrained by $3 \times 1 + 3 \times 1 = 6$ constraints: the 3 black bonds (which represent the fold lines), and 3 gray bonds (representing the rigid plates), which each represent one constraint. In total we therefore have $12 - 6 = 6$ degrees of freedom. These correspond to the 6 degrees of freedom (rotation and

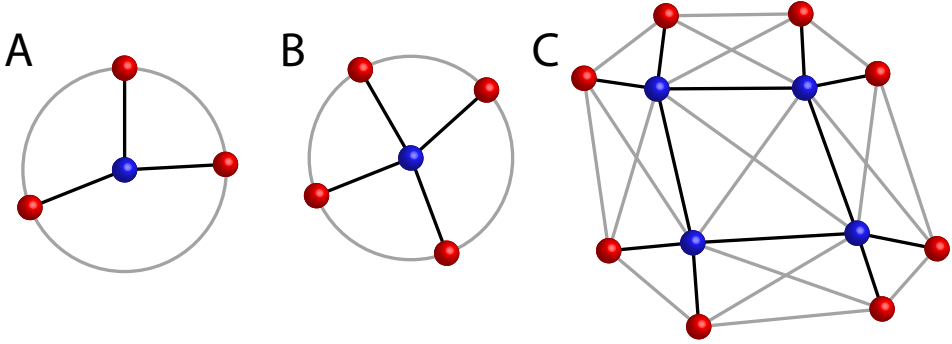


FIGURE 1.6: (A) A vertex where three folds come together can not fold rigidly. (B) A generic 4-vertex has a single degree of freedom. (C) A mesh consisting of four 4-vertices together is generically overconstrained, but can fold rigidly if the sector angles around each vertex are related by symmetries.

translation) of a rigid body in three dimensions; the number of internal d.o.f. thus equals $12 - 6 - 6 = 0$. A 3-vertex is therefore *overconstrained*, and can not fold rigidly.

For a single 4-vertex, where 4 lines come together, the same calculation tells us there is exactly $5 \times 3 - 4 \times 1 - 4 \times 1 - 3 - 3 = 1$ internal d.o.f. A single 4-vertex can therefore fold rigidly. We note, in passing, that flat 4-vertices have two distinct continuous folding branches, each with a single degree of freedom [28]. We now ask what happens when we add multiple 4-vertices together into a pattern, such as in Fig. 1.4.A? This scenario is depicted in Fig. 1.6.C, where four 4-vertices surround a single rigid quadrilateral plate. In this case, we count $12 \times 3 = 36$ d.o.f. for the 12 points, 12×1 constraints for the bonds that represent the creases, $5 \times 2 = 10$ d.o.f. for the bonds that rigidify the 5 quadrilateral plates, and 8 d.o.f. for the bonds around the periphery. This results in $36 - 12 - 10 - 8 - 6 = 0$ non-trivial d.o.f. We therefore see that, even though a single 4-vertex can generically fold, patterns consisting of multiple 4-vertices are generically rigid. In order to construct rigidly foldable 4-vertex patterns such as the one shown in Fig. 1.4.A, it is necessary to exploit symmetries and *non-generic* vertices, so that degeneracies in the constraints generate non-trivial degrees of freedom.

1.2.3 4-Vertex Fold Patterns

As shown in the previous section, 4-vertex patterns are generically over-constrained, and can not fold rigidly unless the vertices that constitute the pattern are in some way related. Here we will give a few examples of rigidly foldable 4-vertex patterns known from literature, such as the Miura-ori pattern in Fig. 1.4.A, which *do* rigidly fold.

One of the first known quadrilateral fold patterns is the so called ‘Huffman’ pattern, named after Huffman [48], although it was A. Kokotsakis who first published this pattern as rigidly foldable [49]. This pattern, shown in Fig. 1.7.A, is based on the well known tessellation in which a single generic quadrilateral, with inner angles α_i ($i = 1, 2, 3, 4$), is used to tile the plane, by alternating copies of itself by copies that are rotated by 180° . Remarkably, the shape into which this pattern folds was not described until very recently. In [50] it was shown that this flat pattern can fold into a cylindrical shape in two different ways: one along the vertical direction and one along and the horizontal direction. Here columns, respectively, rows of quadrilaterals in the flat pattern trace out a helical path on the surface of the circumscribed cylinder.

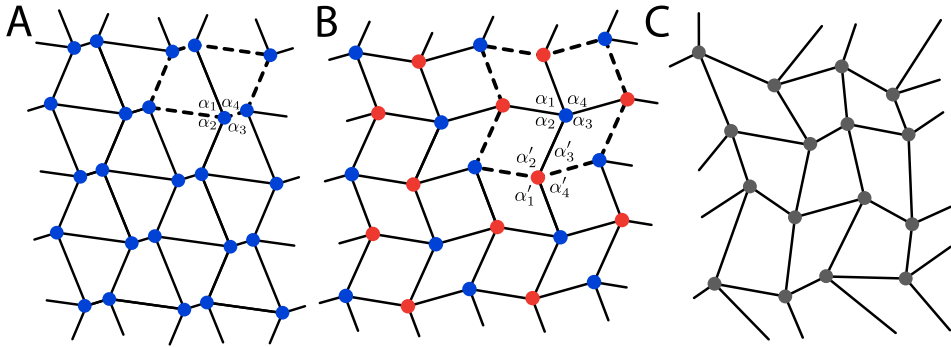


FIGURE 1.7: Three different quadrilateral patterns that are rigidly foldable. (A) Huffman pattern [48]. All vertices have identical sector angles α_i , and are oriented in the same direction. (B) Generalized version of Barreto’s MARS pattern [28, 51]. Pattern contains CW oriented vertices with sector angles α_i , and CCW oriented vertices with sector angles $\alpha'_i = \pi - \alpha_i$ (red). (C) Non-periodic pattern designed using Origamizer software [16, 19]. Fold pattern from [52]. Dashed lines in panel A and B indicates unit cell.

Another example of a rigidly foldable pattern can be obtained by modifying the Miura-Ori pattern shown in Fig. 1.4, such that it no longer has any straight lines. This variation is shown in Fig. 1.7.B, and was first described by Barreto [51]. A generic version of this pattern was later described by Waitukaitis et al. [28]. The unit cell of this tiling (indicated by the dashed line) consists of 4 different parallelograms surrounding a vertex (in blue) with angles α_i , where $i = 1, 2, 3, 4$. When this unit cell is tiled, it therefore results in a pattern with two types of vertices: the blue vertices with sector angles α_i , oriented in a counterclockwise direction, and the red vertices with *supplemented* sector angles $\alpha'_i = \pi - \alpha_i$, oriented in a clockwise direction.

Finally, it was shown by Tachi in 2009, that rigidly foldable quadrilateral patterns do not necessarily have to be periodic [16]. The pattern shown in Fig. 3.1.C folds rigidly, despite the fact that the sector angles at every vertex are different. However, the sector angles in this pattern are tuned by a computer algorithm, such that each of the nine internal quadrilaterals can fold rigidly with a single degree of freedom [19]¹. As a result, the whole pattern can fold rigidly with a single degree of freedom.

The patterns shown in Fig. 3.1 are just three examples of rigidly foldable 4-vertex patterns. Other variations on these patterns exist, many of which are based on the Miura-ori pattern, these include: modular tubular structures [53, 54], semi rigidly-foldable patterns with arbitrary curvature [34], superimposed fold patterns that allow for hierarchical folding [55], trapezoidal fold patterns with double curvature [56], and fold patterns where each vertex is replaced by a ‘corner-gadget’ [57].

1.3 This Thesis

This thesis starts with chapter 2, where we describe the necessary conditions under which a two by two 4-vertex mesh can fold rigidly. We show how to precisely count the number of rigidly foldable two by two vertex meshes one can construct using four symmetry-related vertices: those with sector angles α_i , those with sector angles $\pi - \alpha_i$, and their respective mirror images. Furthermore, we show how to depict all of these meshes as a combinatorial puzzle pieces, which allows for the construction of rigidly foldable meshes of arbitrary size. In chapter 3 we show how to construct

¹The same computer algorithm as used to design the fold pattern in Fig. 1.2.

rigidly foldable 4-vertex patterns using these puzzle pieces. We find that the patterns can be classified into four different classes, and for each class count the number of m by n vertex patterns. Furthermore, we show that fold patterns constructed using this methodology have multiple folding branches, which all have a single degree of freedom, and count the number of folding branches for each of the four classes. In chapter 4 we then focus on one of these classes, which has two folding branches regardless of the size of the pattern, and show that we can design m by n vertex patterns with two folding branches that have a pre-programmed curvature, resulting in a multishape material.

In chapter 5 we once again focus on single 4-vertices, and study non-Euclidean 4-vertices, i.e. vertices of which the sector angles no longer add up to 2π . In such a case it is no longer possible to access the flat configuration by rigidly folding the vertex, which results into two disconnected folding branches. By 3D-printing 4-vertices with a slight angular deficit (or surplus), and dressing these with a torsional spring, we show that we can harness these two folding branches to create tristable vertices.

DISCRETE ORIGAMI TILES

2.1 Introduction

Origami based metamaterials, comprised of stiff plates connected by flexible hinges, are specified by two-dimensional crease patterns composed of vertices connected by straight creases. 4-vertices are ideal building blocks of such crease patterns as they exhibit two distinct folding motions [28, 58]. In this section we will combine 4-vertices to make rigidly foldable meshes. In particular, we will focus on two by two 4-vertex meshes as their foldability is a necessary and sufficient condition for foldability of larger meshes. The general problem of the flexibility of such a 4-vertex mesh was first discussed by Kokotsakis [49], and has recently received renewed interest due to advances in the field of discrete differential geometry [59–61]. However, these efforts concentrate on the symmetries that need to be present in order for a two by two 4-vertex mesh –which is generically overconstrained– to fold rigidly.

In this chapter, we will instead aim to answer the question: how many different rigidly foldable meshes can we construct by combining a generic vertex, its mirror image, and their supplements. We will show that these 4 vertices can be represented as 140 discrete ‘bricks’ which can be combined in different ways to form larger tilings, and ultimately crease patterns. Here, we will show how we obtain these 140 bricks, and list which properties they have. In the chapter 3 we will show how these building blocks can be combined to form crease patterns. We will classify the resulting patterns, and count them. In chapter 4, we will show that these bricks can be used to design unique, multishape origami crease patterns which can be folded into two different, pre-programmed shapes.

2.2 Rigid Folding Conditions

A 4-vertex fold pattern can be divided into 2×2 vertex sub-meshes (Fig. 2.1.A), which are also named Kokotsakis meshes. A quadrilateral crease pattern is only rigidly foldable when each of these sub-meshes are rigidly foldable. In Fig. 2.1.B we show such a 2×2 vertex sub-mesh, consisting of four 4-vertices, $\{W, X, Y, Z\}$, with sector angles $\{\alpha_i, \beta_i, \gamma_i, \delta_i\}$ in red. Furthermore, we indicate the out-of-plane fold angles ρ_i (in grey), where $\rho_i = 0$ corresponds to the flat state. In order for this 2×2 vertex mesh to be rigidly foldable, we now require the following sum condition [16, 49, 62]:

$$\alpha_1 + \beta_4 + \gamma_3 + \delta_2 = 2\pi, \quad (2.1)$$

in order for the central plate to be flat, which is a necessary, but not a sufficient condition for rigid foldability. Furthermore, we have the necessary condition,

$$\begin{aligned} \rho_1^W &= \rho_3^X, \\ \rho_4^X &= \rho_2^Y, \\ \rho_3^Y &= \rho_1^Z, \\ \rho_1^Z &= \rho_2^W, \end{aligned} \quad (2.2)$$

in order for any collective out of plane folding motion to be geometrically compatible. As 4-vertices have one degree of freedom [28], it is possible to express every fold angle as function of another (see Appendix A), for example: $\rho_2^Z(\rho_1^Z)$. Using this, we can rewrite the conditions in Eq. 2.2 in a single equation,

$$\rho_2^Z(\rho_3^Y(\rho_4^X(\rho_1^W(\rho_1^Z)))) = \rho_2^Z, \quad (2.3)$$

which can further simplify by defining operators, $\rho_{21}^Z = \rho_2^Z(\rho_1^Z)$,

$$\rho_{21}^Z \circ \rho_{32}^Y \circ \rho_{43}^X \circ \rho_{12}^W = \mathbf{I}. \quad (2.4)$$

This *loop condition* needs to be satisfied on every internal quadrilateral of a quadrilateral mesh in order for it to be rigidly foldable [16, 62]. Furthermore, as the exact form of e.g. the non-linear operators –e.g. ρ_{ij}^W – depends on the in-plane sector angles $\{\alpha_i, \beta_i, \gamma_i, \delta_i\}$, Eq. 2.4 will not be satisfied when choosing arbitrary $\{\alpha_i, \beta_i, \gamma_i, \delta_i\}$.

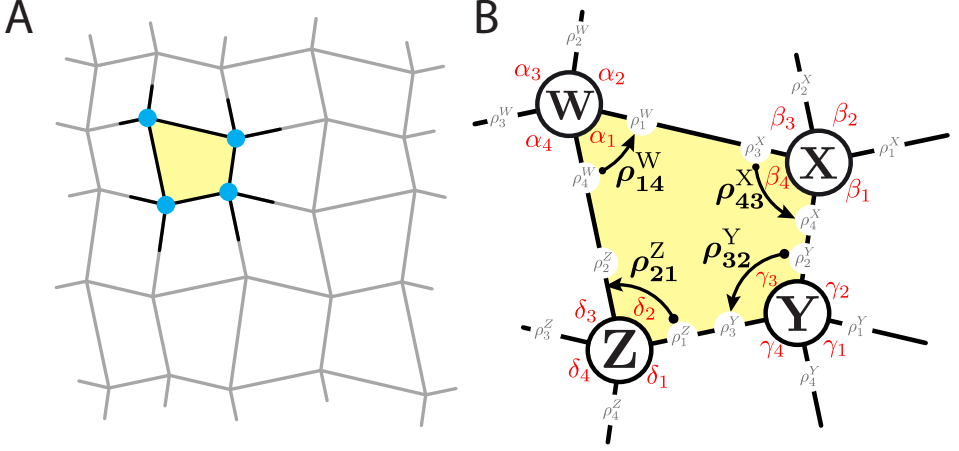


FIGURE 2.1: (A) Quadrilateral crease pattern (gray) composed of Kokotsakis submeshes (black), consisting of four 4-vertices (light blue) around central plates (yellow). (B) A Kokotsakis mesh is rigidly foldable if and only if the compatibility conditions Eqs. 2.1 and Eq. 2.4) are satisfied. The red labels indicate the in-plane sector angles of the 4 vertices W, X, Y, Z, whereas the gray labels indicate the out-of-plane angles. The four black labels in the middle indicate the fold operators (see text).

2.3 Combinatorial Loop Condition

In this section we aim to find 2×2 vertex meshes which simultaneously solve Eq. 2.1 and Eq. 2.4. Our strategy is to replace vertices W-Z in Fig. 2.1 by one of the four following vertices: (i) a 4-vertex with angles α_i (Fig. 2.2.i), (ii) its mirror image (Fig. 2.2.ii), (iii) the supplement of vertex (i) with angles $\alpha'_i = \pi - \alpha_i$ (Fig. 2.2.iii), and (iv) the mirror image of vertex (iii) (Fig. 2.2.iv). We denote the out-of-plane fold-angles ρ_i for vertices (i) and (ii), and ρ'_i for the two supplemented vertices (iii) and (iv). Furthermore we define operators that relate one fold angle to another, $\rho_{i+1,i}(\rho_i) = \rho_{i+1}$ (or $\rho'_{i+1,i}$ for the supplemented vertices). These operators are defined to operate in a counterclockwise fashion (Fig. 2.2).

For each vertex in the 2×2 mesh we can choose whether to pick vertex (i)-(iv). Once this choice is made, each vertex can be oriented in four different manners. Together this leads to a total of $4 \times 4 = 16$ possible options for a given vertex. For a 2×2 vertex mesh this leads to a total number of $16^4 = 65536$ meshes.

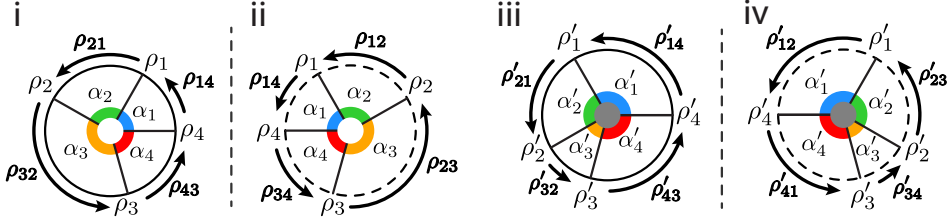


FIGURE 2.2: (i) Counterclockwise oriented vertex with sector angles α_i . (ii) Mirror image of vertex (i). (iii) The supplement of vertex (i), with sector angles $\pi - \alpha_i$. (iv) Mirror image of vertex (iii). Note the colors are identical for α_i and α'_i , and the white/gray dot in the center of the vertex indicates whether the vertex is supplemented.

Most of these violate either condition Eq. 2.1 or Eq. 2.4 (or both), but a significant number of combinations satisfy both conditions. These can be found by brute force, but to gain more insight, we make use of three relations. First, an operator and its inverse annihilate each other,

$$\rho_{ij} \circ \rho_{ji} = I. \quad (2.5)$$

Second, we note that the operators are odd, such that we have,

$$\rho_{ij}(-\rho) = -\rho_{ij}(\rho). \quad (2.6)$$

Third, we have,

$$\rho_{ij} = -\rho'_{ij}, \quad (2.7)$$

which we derive explicitly in appendix A. This is the most critical ingredient to construct rigidly foldable quadrilateral meshes.

In order to find all possible rigidly foldable 2 by 2 vertex meshes based on the four vertices (i)-(iv) of Fig. 2.2, we can now write down a general version of the loop condition of Eq. 2.4:

$$\rho_{i,i\pm 1} \circ \rho_{j,j\pm 1} \circ \rho_{k,k\pm 1} \circ \rho_{l,l\pm 1} = I, \quad (2.8)$$

and ask ourselves which combination of indices $\{i, j, k, l\} \in \{1, 2, 3, 4\}$ and signs satisfy this condition, making use of relations Eq. 2.5, Eq. 2.6, and Eq. 2.7. We note that Eq. 2.7 allows us to supplement an even number of operators (zero, two, or four) in Eq. 2.8 without affecting the loop condition,

as the operators are odd (Eq. 2.6). This property allows us to decouple the problem of satisfying the loop condition from the problem deciding which (pairs of) vertices should be supplemented. Moreover, as we will see, for each operator quad that satisfies Eq. 2.8, there are at least two supplementation patterns that satisfy the sum rule (Eq. 2.1). The solutions to Eq. 2.8 presented below are therefore at least twofold degenerate, as we can always invert the supplementation of all four operators. Some solutions however, are fourfold or sixfold degenerate, we will come back to this in detail in section 2.5.

Firstly, note that:

$$\rho_{4,3} \circ \rho_{3,2} \circ \rho_{2,1} \circ \rho_{1,4} = I, \quad (2.9)$$

and,

$$\rho_{1,2} \circ \rho_{2,3} \circ \rho_{3,4} \circ \rho_{4,1} = I, \quad (2.10)$$

as these cyclic operations simply describe the folding operation of a single vertex, see Fig. 2.2.ii and Fig. 2.2.i respectively. In addition we find the following nine additional combinations of operators that yield identity:

$$\rho_{i,i-1} \circ \rho_{i-1,i} \circ \rho_{i,i-1} \circ \rho_{i-1,i} = I, \quad (2.11)$$

$$\rho_{i,i-1} \circ \rho_{i-1,i} \circ \rho_{i-1,i} \circ \rho_{i,i-1} = I, \quad (2.12)$$

$$\rho_{i,i-1} \circ \rho_{i-1,i} \circ \rho_{i+1,i} \circ \rho_{i,i+1} = I, \quad (2.13)$$

$$\rho_{i,i-1} \circ \rho_{i-1,i} \circ \rho_{i,i+1} \circ \rho_{i+1,i} = I, \quad (2.14)$$

$$\rho_{i-1,i} \circ \rho_{i,i-1} \circ \rho_{i+1,i} \circ \rho_{i,i+1} = I, \quad (2.15)$$

$$\rho_{i-1,i} \circ \rho_{i,i-1} \circ \rho_{i,i+1} \circ \rho_{i+1,i} = I, \quad (2.16)$$

$$\rho_{i,i-1} \circ \rho_{i-1,i} \circ \rho_{i+2,i+1} \circ \rho_{i+1,i+2} = I, \quad (2.17)$$

$$\rho_{i,i-1} \circ \rho_{i-1,i} \circ \rho_{i+1,i+2} \circ \rho_{i+2,i+1} = I, \quad (2.18)$$

$$\rho_{i-1,i} \circ \rho_{i,i-1} \circ \rho_{i+1,i+2} \circ \rho_{i+2,i+1} = I, \quad (2.19)$$

where $i = 1, 2, 3, 4$, and it is understood that the indices are defined modulo 4, i.e. $\text{mod } (i - 1, 4) + 1$. Additionally, we left multiply the operators, which corresponds to evaluating the loop condition in a clockwise fashion, and starting in the top left corner (also see Fig. 2.1.B). Varying i , Eqs. 2.11-2.16, 2.18 lead to four different configurations each, for a total of $6 \cdot 4 = 28$ different configurations. Eq. 2.17 and Eq. 2.19 each only lead to two

different configurations, as these equations are identical for $i = 1, 3$ and $i = 2, 4$ ¹, for a total of $2 \cdot 2 = 4$ different configurations. Last, Eqs. 2.9, 2.10 each contribute only 1 configuration. All in all there are therefore $24 + 8 + 2 = 34$ different operator quads which satisfy Eq.2.8. Without appropriate supplementation, only Eq. 2.9 and Eq. 2.10 satisfy both the ‘sum-rule’ (Eq. 2.1) and the ‘loop-equation’ (Eq. 2.8). We state again that, all operator quads admit at least two supplementation patterns that *both* satisfy the sum rule (Eq. 2.1) *and* the loop equation (Eq. 2.8), leading to a multitude of rigidly foldable 2×2 vertex meshes+ for details see section 2.5.

2.4 Tiles

Quadrilateral meshes larger than 2×2 vertices can only fold rigidly when Eq. 2.4 is satisfied for every 2×2 vertex submesh [16]. To facilitate creating larger meshes based on the 34 different configurations of Eq. 2.9, Eq. 2.10, and Eqs. 2.11–2.19, we devise a graphical representation of each of these equations. In Fig. 2.3.A we depict a diagram of a counterclockwise oriented vertex, where the sector angles α_i correspond to specific colors. Furthermore, the profile of each protrusion uniquely corresponds to a specific fold angle ρ_i , where the protrusions point in the same orientation as the vertex itself. The clockwise oriented mirror image of the vertex in Fig. 2.3.A is shown in Fig. 2.3.B - note that the protrusions in this case also point in the clockwise direction.

When we now use the counterclockwise oriented vertex of Fig. 2.3.A and the clockwise oriented vertex of Fig. 2.3.B to make a diagram of a 2×2 vertex mesh, we naturally obtain a square tile with four protrusions and four indentations. An example of such a tile is shown in Fig.2.3.C, where we combined four (rotated) copies of the vertex shown in Fig.2.3.B. The shape outlined by the dashed line –including the colored corners– is what we now define as a ‘tile’. In this case it depicts a two by two vertex mesh that is described by Eq. 2.10 ($\rho_{12} \circ \rho_{23} \circ \rho_{34} \circ \rho_{41} = I$); this can be seen by following the fold angles in Fig.2.3.B, and applying the operators in a counterclockwise fashion, starting from the bottom left vertex.

This graphical representation can extended to each of the equations

¹After allowing for a cyclical permutation of the operators, as the loop condition in Fig. 2.1.B can be evaluated starting from any of the four vertices.

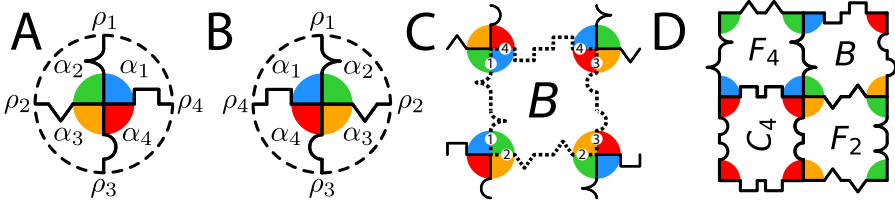


FIGURE 2.3: (A) Symbolic depiction of 4-vertex where the sector angles α_i are represented by colors. (B) Mirror image of the 4-vertex depicted in (A). (C) Four (rotated) copies of the vertex in (B), representing a two by two vertex mesh. The dashed shape is an example of a ‘tile’. Numbers indicate the index of the respective fold. (D) Tiles can be combined to represent larger meshes.

Eq. 2.9, Eq. 2.10, and Eqs. 2.11–2.19; the resulting 34 tiles are shown in Fig. 2.4. We note that each tile can be rotated. The orientation here will be referred to as horizontally oriented. Rotating clock- or counterclockwise by 90° we obtain vertically oriented tiles; rotating by 180° yields a horizontally oriented tile. These tiles can be combined to represent bigger meshes, provided they fit together. When an appropriate supplementation pattern is chosen –which is always possible– these meshes are guaranteed to correspond to real space crease patterns which fold rigidly. An example a tiling is shown in Fig. 2.3; where we show a two by two tile pattern, consisting of tiles F_4, B, C_4 and F_2 . Note that the C_4 tile is rotated a quarter turn counterclockwise with respect to its position in table 2.4 in order to fit the three other tiles. This two by two tile pattern can be converted into a three by three 4-vertex mesh², once we specify sector angles α_i , mesh lengths, and which vertices are supplemented to satisfy Eq. 2.1.

To construct such tilings, we make use of two discrete characteristics of the tile edges. First, we note the parity of the number of different shapes on opposite edges; the four edges (N/E/S/W) of every tile either consist of the same shape (parity: odd), or two different shapes (parity: even). Here it is understood that each protrusion/indentation has one of four shapes: cusp, triangle, semicircle, rectangle. Opposite edges of each tile have the same parity. A second quantity that is equal at opposite edges is the parity

²Due to our schematic depiction using tiles, we do not show the four vertices positioned on the top-left, top-right, bottom-right, and bottom-left corners. However, they are uniquely determined by the colors in the tiling and direction of the protrusions.




























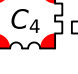






	Eq. 2.9	Eq. 2.10	Eq. 2.13	Eq. 2.14	Eq. 2.15	Eq. 2.16	Eq. 2.17	Eq. 2.18	Eq. 2.19	Eq. 2.20	Eq. 2.21
i=1											
i=2											
i=3											
i=4											

FIGURE 2.4: Table with all 34 tiles corresponding to Eq. 2.9, Eq. 2.10, and Eqs.2.11–2.19.

(odd/even) of the number of outward facing protrusions. The values of these quantities are indicated in Table. 2.1.

As an example, consider the *A*-tile, where both the north- and southside of the tile consist of only one type of shape (parity: odd), as well as the east- and westside (parity: odd). Furthermore, the north- and the southside –as well as the east- and westside– of the *A*-tile both have one outward facing protrusion (parity: odd). The edge characteristic of the *A* tile is therefore: odd/odd/odd/odd, or *oooo* for short; where we first indicate the parity of the shape of the north-southside, then the parity of the number of outward facing protrusions on the north-southside, then the parity of the number of shapes on the east-westside, and finally the number of outward facing protrusions on the east-west side. Crucially, as edge-characteristics are equal for opposite sides, these characteristics are conserved along the connecting edges of each column and row of a tiling. As we will see in chapter 3 this property limits the orientations of some tiles when constructing larger patterns, and is crucial to understand the allowed supplementation patterns.

2.5 Bricks

The tiles listed in Fig. 2.4 can not directly be converted to real space meshes, as we first need to decide which vertices are supplemented and

	North-South		East-West	
	No. of different shapes	No. of outward facing protrusions	No. of different shapes	No. of outward facing protrusions
A	odd	odd	odd	odd
B	odd	odd	odd	odd
C_i	odd	even	odd	even
D_i	odd	even	even	odd
E_i	odd	even	even	even
F_i	odd	even	odd	odd
G_i	odd	even	even	odd
H_i	odd	even	even	even
I_i	odd	even	even	even
J_i	odd	even	even	odd
K_i	odd	even	even	even

TABLE 2.1: Overview of the edge characteristics of the different tiles displayed in Fig. 2.4.

which are not. As discussed, this supplementation is needed to satisfy the sum rule, and when (appropriate) pairs are supplemented, does not change the loop rule. A picture of a three by two pattern is shown in Fig. 2.5.A. This particular pattern can be supplemented in several ways, one of which is shown in Fig. 2.5.B; here we indicate supplemented vertices by a gray dot, and unsupplemented vertices by a white dot. We now see that the units of which the pattern in Fig. 2.5.B is composed, constitute a building block of their own. We define such building blocks as ‘bricks’, and one example is shown in Fig. 2.5.C, where the gray corners indicate supplemented angles, and white corners indicate unsupplemented angles. Because a brick encodes the supplementation on its corners, there is a one-to-one correspondence with a real-space mesh, once the sector angles and mesh lengths are fixed.

Note the brick in Fig. 2.5.C carries a superscript index, E_4^2 which indicates that the two leftmost vertices of this brick (in its ‘upright’ orientation) are supplemented. The number of distinct supplementation patterns depends on the tile, and are summarized in the table shown in Fig. 2.6. Here the eight possible supplementation patterns are shown on the top, labeled 0–7, where the gray corners indicate supplemented vertices. These eight supplementation patterns correspond to the eight possible ways in which

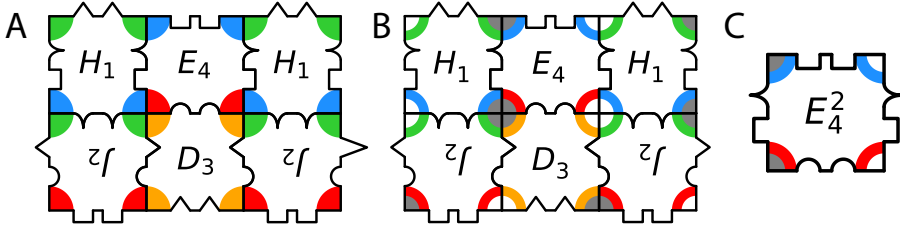


FIGURE 2.5: (A) A 3×2 tile pattern. (B) The same 3×2 tiling as in (A), with a particular choice of supplemented vertices, which are indicated by the gray or white circles. (C) A ‘brick’, taken from the tiling in (B). Note the superscript 2 in E_4^2 indicates which vertices of the brick are supplemented (see text for details).

we can supplement an even number of vertices within a tile. However, not all of these eight options satisfy the sum-rule (Eq. 2.1). For example, a C_1 tile can be supplemented in six different ways: C_1^1 , C_1^2 , C_1^3 , C_1^4 , C_1^5 , and C_1^6 , as we can choose any pair of vertices to supplement and still satisfy Eq. 2.1. Supplementing all (C_1^0) or none (C_1^7) of the vertices within this brick is impossible, as both $4 \cdot \alpha \neq 2\pi$ and $4 \cdot \alpha'_i \neq 2\pi$. Likewise, all D_i tiles can be supplemented in six different ways.

Bricks $\{E_i - K_i\}$ need one supplemented vertex on the top, and one on the bottom in order to satisfy Eq. 2.1. As these can be chosen independently, this produces four different supplementation patterns (see Fig. 2.6). Finally, tiles $\{A, B\}$ can be supplemented in only two different ways. These are the only tiles for which the loop condition does not rely on the annihilation of pairs of operators, and the only for which we use all four sector angles α_i . As such, we can only supplement all of the (A^0 and B^0), or none (A^7 and B^7).

Analogous to Fig. 2.4 we now list all unique bricks. In order to accurately count the number of unique bricks, we have to keep track of bricks which are identical under rotations. We find that such rotation symmetries only occur for the C_i tiles, where for example C_1^3 is identical to C_1^5 when flipped upside down, and likewise for C_1^4 and C_1^6 . This is not the case for D_i bricks, for which all six supplementations are unique, nor for any other brick. All in all we therefore find $2 \times 2 + 4 \times 4 + 4 \times 6 + 24 \times 4 = 140$ unique bricks, all of which are shown in Fig. 2.7.



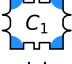











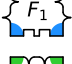


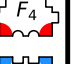



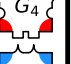












	Supplementation							
	0	1	2	3	4	5	6	7
 A	0							7
 B	0							7
 C_1		1	2	3	4	5	6	
 C_2		1	2	3	4	5	6	
 C_3		1	2	3	4	5	6	
 C_4		1	2	3	4	5	6	
 D_1		1	2	3	4	5	6	
 D_2		1	2	3	4	5	6	
 D_3		1	2	3	4	5	6	
 D_4		1	2	3	4	5	6	
 E_1		1	2		4		6	
 E_2		1	2		4		6	
 E_3		1	2		4		6	
 E_4		1	2		4		6	
 F_1		1	2		4		6	
 F_2		1	2		4		6	
 F_3		1	2		4		6	
 F_4		1	2		4		6	
 G_1		1	2		4		6	
 G_2		1	2		4		6	
 G_3		1	2		4		6	
 G_4		1	2		4		6	
 H_1		1	2		4		6	
 H_2		1	2		4		6	
 H_3		1	2		4		6	
 H_4		1	2		4		6	
 I_1		1	2		4		6	
 I_2		1	2		4		6	
 J_1		1	2		4		6	
 J_2		1	2		4		6	
 J_3		1	2		4		6	
 J_4		1	2		4		6	
 K_1		1	2		4		6	
 K_2		1	2		4		6	

FIGURE 2.6: Table indicating which of the eight supplementation patterns are valid for each tile, such that we can convert them into bricks. Supplementation patterns 5 and 6 are grayed out for the C_i tiles, due to symmetry – see text. The resulting 140 bricks are shown in Fig. 2.7.



FIGURE 2.7: Table listing all 140 possible bricks.

2.6 Summary and Outlook

In this chapter, we aimed to count the number of rigidly foldable, two by two 4-vertex meshes that can be constructed using the four symmetry related vertices shown in Fig. 2.2. We were able to answer this question using the language of operators. Furthermore, we developed a graphical representation for each of the 140 possible meshes, depicting each mesh as a combinatorial puzzle piece. In the next chapter we will make extensive use of this combinatorial representation to construct larger meshes. We will first categorize which puzzle pieces fit together in one and the same pattern, giving rise to four different classes of patterns. We will count the number of patterns of a given size within each class, and examine the properties of patterns within each class.

2.6. SUMMARY AND OUTLOOK

CLASSIFICATION OF TILE PATTERNS

3.1 Introduction

In this chapter we will show how tiles and bricks can be combined to form larger tilings and brick patterns, how the latter can be translated to crease patterns, and how we can determine their corresponding mountain-valley configurations. In particular, we formulate and solve the three combinatorial problems that govern tilings, brick patterns, and mountain-valley configurations.

An example of a 4×4 tile pattern is shown in Fig. 3.1.A. As all tiles fit, all vertex colors are consistently defined. This *tile pattern* or *tiling* can be converted into a *brick pattern*, as shown in Fig. 3.1.B. Here each tile has acquired an allowed supplementation pattern (Fig. 2.6, Fig. 2.7), and supplementations are consistent between adjacent bricks. All vertices are now uniquely defined, as we know their supplementation, their orientation, and their clockwise or counterclockwise character. If we then choose a set of angles α_i , as well as lengths t_i and l_i , we can convert this brick pattern into a crease pattern, as shown in Fig. 3.1.C. Note that an $m \times n$ brick pattern defines a $3 + m + n$ -parameter family of crease patterns. Finally, we can determine a specific mountain-valley pattern for this crease pattern (Fig. 3.1.D). This mountain valley pattern is not unique as all crease patterns obtained by our method allow at least two different mountain valley patterns (not related by trivial mountain \leftrightarrow valley symmetry).

In this chapter we will count the number of tilings, the number of supplementation patterns for each tiling, and finally, the number of mountain-valley patterns. In section 3.2 we start by showing how to define four distinct tiling classes (I, II, III, and IV). For a given class, each tiling contains one or more necessary tiles and an arbitrary number of optional

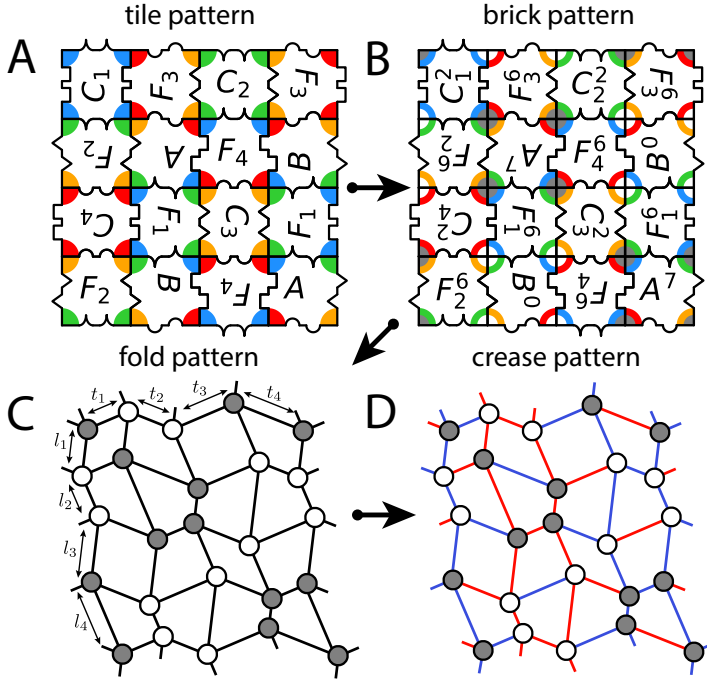


FIGURE 3.1: (A) A tile pattern (or tiling). (B) The same pattern with a specific supplementation pattern yields a definite brick pattern. (C) Crease pattern corresponding to the brick pattern in (B), with a choice of angles of $\alpha_1 = 60^\circ, \alpha_2 = 90^\circ, \alpha_3 = 135^\circ, \alpha_4 = 75^\circ$, and mesh lengths t_i and l_i . (D) One corresponding mountain (red) valley (blue) configuration.

tiles - other tiles do not fit. We show that an important property of this classification is that within each class, each L-shaped triplet of tiles admits precisely one fitting fourth tile. In section 3.3 we show how this last property allows us to exactly count the number of $m \times n$ tile patterns. We verify by brute force that the tilings in class-I-IV cover all possible tilings, up to $m = 6, n = 6$. For $m = 6, n = 6$ there are already to 4226048 distinct tilings. In section 3.4, we show in how many ways we can choose the supplementation of a pattern, i.e. in how many ways can we convert an $m \times n$ tile pattern into an $m \times n$ brick pattern. We show that there are *at least* two valid ways in which we can turn a tile-pattern into a brick pattern. However, some classes of tiling have exponentially many ways in which we

3.2. TRIPLET COMPLETION AND CLASSIFICATION

specify the fourth vertex (up to supplementation) and thus *uniquely* specify a potential tile. In this case, this corresponds to tile ‘ X ’ shown in Fig. 3.2.B. However, tile X does not occur within the set of 34 tiles shown in Fig. 2.4, as the four corresponding operators do not satisfy the loop condition. In contrast, the triplet of tiles shown in Fig. 3.2.C *does* admit a tile that occurs within the set of 34 tiles shown in Fig. 2.4.

We now define tiling classes as follows. If a triplet does not admit a fourth tile, the three tiles cannot be in the same class. If a triplet admits a fourth tile, all tiles are in the same class. By considering all triplets, we find that these two rules define four distinct classes, labeled I-IV. A given tiling can easily be identified as belonging to one of these classes by inspecting the presence of certain tiles (see Fig. 3.3). In tilings in each class, at least one tile out of a subset of tiles has to be present; in addition, some classes contain a group of *optional* tiles, which may or may not be present in a tiling.

Each tile is a necessary tile in precisely one class. It can be checked that for each triplet of tiles within a class, there always is a unique fourth fitting tile. This property, which we will refer to as *triplet completion*, greatly simplifies the construction and enumeration of tilings: once a single row and column of a $m \times n$ tiling is specified, the full tiling can trivially be constructed by iteratively applying the triplet completion rule (Fig. 3.2.D).

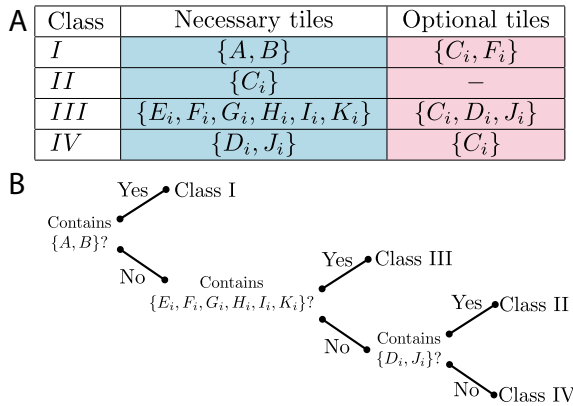


FIGURE 3.3: (A) Tiling classes. (B) Decision tree to determine whether a given tiling created using the tiles of Fig. 2.4 is a class-I, class-II, class-III, or class-IV tiling.

3.3 Counting Multiplicity of Tilings

In this section we will derive expressions for the number of tilings that can be constructed within each class. To do this, we first define the concept of *connection numbers*. In each class, we define for each side of a tile, the number of distinct sides of necessary tiles and the number of distinct sides of optional tiles that fit. To facilitate discussions about the tiles, we define the orientation of the tiles as shown Fig. 2.4 as the ‘horizontal’ orientation, and refer to their sides by the four cardinal directions (north, east, south, and west). We note that for all tiles, the connection numbers at opposite sides are equal, allowing us to capture the connections by four integers (Fig. 3.4.A). The necessary connection numbers along the north/south and east/west sides are, respectively, x and v (in blue). The optional connection numbers along the north/south and east/west sides are, respectively y , w (in pink).

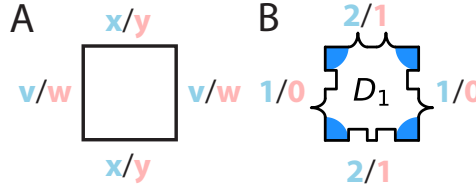


FIGURE 3.4: (A) For every side of every tile we can define a connection number within a given glass (blue: necessary, red optional tiles). (B) Example of connectivity of D_1 tile in class-IV.

An example of a tile and its connection numbers is given in Fig. 3.4.B for tile $\{D_1\}$, which is a necessary class-III tile. Within this class it connects to necessary tiles $\{D_4, J_2\}$ on its northside, necessary tile $\{J_4\}$ on the westside, necessary tiles $\{D_2, J_2\}$ on its southside, and necessary tile $\{J_4\}$ on its eastside. Additionally it connects to optional class-III tile $\{D_4\}$ on its southside, and optional tile $\{D_2\}$ on its northside. Therefore the connection numbers are as indicated in Fig. 3.4.B. We observe that opposing sides have identical *total* connection numbers. As a result, the total connection number at the sides within a row or column of tiles is conserved. This simplifies the counting of configurations.

Counting Class-I Tilings

All tiles in class-I and their connection numbers are shown in Fig. 3.5.A. Class-I tilings contain at least one *necessary* $\{A, B\}$ -tile. Either of these can be used to form a periodic tiling which maps to the Huffman quadrilateral crease pattern (see Fig. 1.7.A). However, a vast number of additional tilings can be generated by mixing these necessary tiles with optional tiles $\{C_i\}$ and $\{F_i\}$.

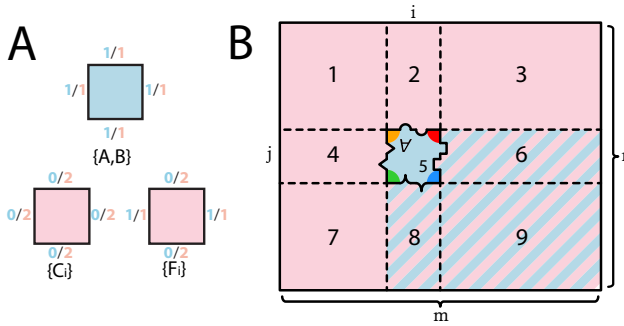


FIGURE 3.5: (A) Class-I tilings contain up to three different types tiles. The *necessary* class-I tiles are tiles $\{A, B\}$. Furthermore there are two different sets of optional class-I tiles: $\{C_i\}$, and $\{F_i\}$. The connection numbers of these sets of tiles are indicated. (B) When counting the number of class-I tilings, we divide a tiling into nine sectors, and assume the first *necessary* class-I tile we encounter is in sector 5, there are eight choices for this tile. Pink sectors contain only optional tiles, hatched blue-pink sectors can contain both optional as well as necessary tiles.

We now illustrate how to construct and count all possible $m \times n$, class I tilings. We make use of two general properties of the adjacencies of tiles within one class: (I) the number of necessary and optional adjacent tiles on opposite sites is equal, and (II) once a single row and column of a tiling are specified, the full tiling can trivially be constructed by triplet completion (Fig. 3.2.D). We label the columns and rows from $i = 1$ to $i = m$, and $j = 1$ to $j = n$ (Fig. 3.5). To construct and count the number of class I tilings, we define the first necessary tile as the necessary tile with the lowest value of $i + j$, denote its location as (i, j) , and partition the tiling in nine sectors 1 – 9 as indicated in Fig. 3.5.B. Sectors 1, 2, and 4 must consist of optional tiles. As the optional connection number for the necessary tile in sector 5

is 1 on all sides, this determines a unique pattern (of F_i tiles) for sectors 2 and 4. In turn, these F tiles uniquely determine sector 1 by applying triplet completion. For the tiles in sectors 6 and sector 8, there are two potential choices for each tile: these tiles can be either an optional type-1 tile, or a necessary type-1 tile. To indicate this, these positions are therefore pink-blue hatched, and these choices lead to $2^{m-i+n-j}$ options in total. For any given choice of tiles in sector 6 and sector 8, the sectors 3, 7 and 9 are again uniquely determined by triplet completion.

Summing over all locations (i, j) , and taking into account there are 8 choices for the first necessary tile (A or B , each in one of four rotations), we obtain that the number of class-I, $m \times n$ tilings equals,

$$N_t^I(m, n) = 8 \cdot \sum_{i=1}^m \sum_{j=1}^n 2^{m-i} \cdot 2^{n-j} = 8 \cdot (2^n - 1) \cdot (2^m - 1). \quad (3.1)$$

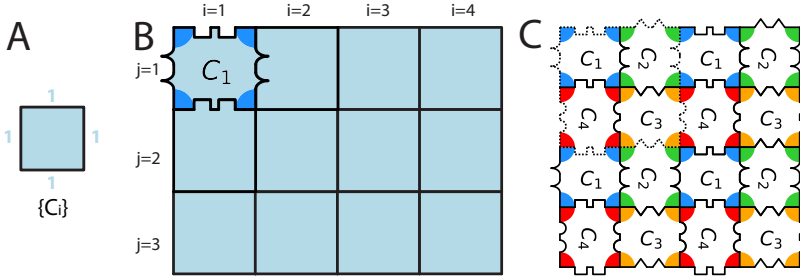


FIGURE 3.6: (A) Class-II tilings only contain tiles $\{C_i\}$. (B) Choosing the type and orientation of the $(1,1)$ tile fixes the whole pattern. (C) Periodic 4×4 type-II tiling, where a 2×2 unit cell is indicated by the dashed line.

Counting Class-II Tilings

Class-II tilings consist exclusively of C_i tiles. These tiles are highly symmetric, and occur as optional tiles in all other classes (see table in Fig. 3.3.A). For class-II tilings, the connection number of the C_i tiles on all sides is 1 (see Fig. 3.6.A). This ensures that, when we determine the tile in position $(i, j) = (1, 1)$, all tiles in the first column, $i = 1$, and the first row, $j = 1$, are fixed. Repeated application of the triplet completion rule (see Fig.

3.2), then fixes the whole tiling (Fig. 3.6.B). The multiplicity of class-II tilings is thus specified by the four possible tiles (C_1, C_2, C_3, C_4), and the two orientations of the $(1, 1)$ tile, yielding,

$$N_t^{\text{II}}(m, n) = 8, \quad (3.2)$$

class-II tilings, independent of m and n . We note that as the tiles form periodic patterns, all m by n tilings can be seen as subtilings of an infinite periodic tiling, where the number of choices of the $(1, 1)$ tile corresponds to the translational and rotational symmetries of the periodic tiling. For an example of a four by four tile periodic class-II tiling, see Fig. 3.6.C.

Counting Class-III Tilings

Class-III tilings contain at least one *necessary* class-III tile $\{E_i, F_i, G_i, H_i, I_i, K_i\}$. Additionally, we can add two different sets of optional tiles, $\{C_i\}$, and $\{D_i, J_i\}$. Together, the connection numbers of these tiles are shown in Fig. 3.7.A. The necessary tiles in class-III only admit a single fitting tile along their east and west sides, and this tile is always a necessary tile. This significantly simplifies the construction of class-III tilings, as necessary tiles can therefore only occur as full columns or rows – but not both. Hence, class-III tilings come in two flavors. Either the necessary tiles are horizontally oriented, and occur in rows with the first one occurring in column 1 (Fig. 3.7.B), or the necessary tiles are vertically oriented, occur in columns, with the first one occurring in row 1 (Fig. 3.7.C).

We now first count the horizontally oriented tilings (Fig. 3.7). The first necessary tile at location $(1, j)$, sector 3, uniquely determines a pattern of necessary tiles in sector 4. There are 20 distinct necessary tiles in class-III, which can be in two horizontal orientations² at location $(1, j)$. For the optional tiles in sector 1 the relevant connection number is three, leading to 3^{j-1} choices, and once sector 1 and 4 are chosen, sector 2 is fixed. Finally for sector 5 we can use either optional or necessary tiles, with a combined connection number of 8, leading to 8^{n-j} options; sector 6 is then determined by triplet completion. Therefore the number of horizontally

²Either the tiles are oriented as in Fig. 2.4, or flipped upside down.

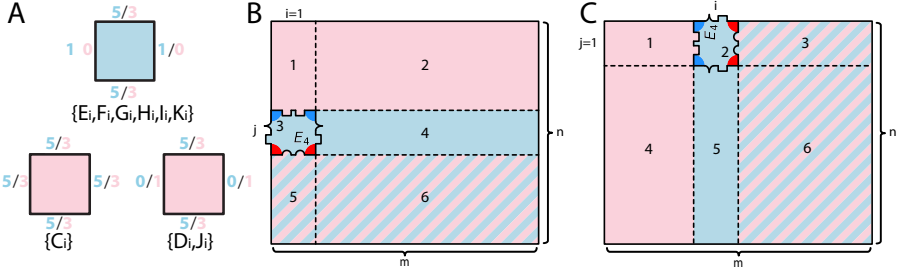


FIGURE 3.7: (A) Class-III tilings contain up to three different sets of tiles: a set of *necessary* class-III tiles: $\{E_i, F_i, G_i, H_i, I_i, K_i\}$, and two sets of optional class-III tiles: $\{C_i\}$, and $\{D_i, J_i\}$. The connection numbers of these three sets of tiles are indicated. (B) A horizontally oriented class-III pattern, divided into six sectors. (C) A vertically oriented class-III pattern, divided into six sectors.

oriented class-III tilings is,

$$N_{\text{t-horizontal}}^{\text{III}}(m, n) = 40 \cdot \sum_{j=1}^n 8^{n-j} \cdot 3^{j-1} = 8 \cdot (8^n - 3^n), \quad (3.3)$$

where m is the number of columns, and n the number of rows. The same holds for vertically oriented patterns, for which the necessary tiles are rotated a quarter turn (either clockwise or anticlockwise) with respect to their orientation as depicted in Fig. 3.7.C. A schematic for this scenario is shown in Fig. 3.7.C. The total number of class-III tilings is,

$$\begin{aligned} N_{\text{t}}^{\text{III}}(m, n) &= 40 \cdot \sum_{i=1}^m 8^{m-i} \cdot 3^{i-1} + 40 \cdot \sum_{i=1}^n 8^{n-i} \cdot 3^{i-1} \\ &= 8 \cdot (8^m - 3^m) + 8 \cdot (8^n - 3^n). \end{aligned} \quad (3.4)$$

Counting Class-IV Tilings

Class-IV tilings contain at least one *necessary* class-IV tile $\{D_i, J_i\}$, and optional tiles, $\{C_i\}$, see Fig. 3.8.A. As in class-III, the necessary tiles only admit one other necessary tile along their east- and westside. The counting is therefore very similar to class-III. In Fig. 3.8.B we show a class-IV tiling, divided into six sectors (1–6). Here we assume the necessary class-IV tiles

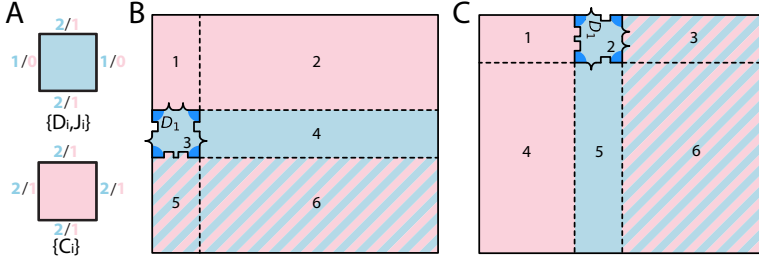


FIGURE 3.8: (A) Class-IV tilings consist out of two sets of tiles. The *necessary* class-IV tiles, $\{D_i, J_i\}$, and the *optional* class-IV tiles $\{C_i\}$. The connection numbers of these two sets of tiles are indicated in the figure. (B) Class-IV tilings are either horizontally or vertically oriented. In this case we show a horizontally oriented pattern, where the necessary tile is horizontally oriented. (C) Vertically oriented class-IV tiling. Pink sectors contain only optional class-IV tiles, blue sectors contain only necessary class-IV tiles, and hatched blue-pink sectors correspond to sectors in which we can find both optional and necessary tiles.

are oriented horizontally, so that the necessary tiles occur in rows. The first sector where we encounter necessary class-IV tiles is sector 3, at location $(1, j)$. The necessary connection number for all tiles in sector 4 is one, the whole row of tiles consisting of sector 3 and 4 together is fixed by choosing the tile (and its orientation) at position $(1, j)$, leading to 16 choices. For the optional tiles in sector 1, the connection number is one, which fixes sector 2. In sector 5 we do have a choice of tiles, as we can choose from two necessary, and one optional tile at every position, for a total of 3^{n-i} options. Summing over all possible initial positions of sector 3, we therefore find,

$$N_{\text{t-hor}}^{\text{IV}}(m, n) = 16 \cdot \sum_{i=1}^n 3^{n-i}, \quad (3.5)$$

horizontally oriented class-IV tilings, where m is the number of rows, and n the total number of columns. The same logic holds for vertically oriented patterns (Fig. 3.8.C), so in total we find,

$$N_{\text{t-hor}}^{\text{IV}}(m, n) = 16 \cdot \sum_{i=1}^m 3^{m-i} + 16 \cdot \sum_{i=1}^n 3^{n-i} = 8 \cdot (3^m - 1) + 8 \cdot (3^n - 1), \quad (3.6)$$

class-IV patterns.

Counting Total Number of Patterns

If we consider the total number of m, n tilings, $N_t(m, n)$, we find, by summing the results in Eq.3.1, Eq.3.2, Eq.3.4, and Eq.3.6, that:

$$N_t(m, n) = 2^{m+3}(4^m - 1) + 2^{n+3}(4^n - 1) + 8 \cdot 2^{m+n}, \quad (3.7)$$

Here we note that $N_t(m, n)$ counts all configurations that are possible when placing the tiles of Fig. 2.4 on an m by n array. Hence, we double count tilings that are related by global rotations and translations³. We note in addition that class-III and class-IV could be combined in one super-class, that satisfies the triplet completion rule, and for which the counting is somewhat simpler, yielding a total of $N_t^{III+IV} = 8 \cdot (8^m + 8^n - 2)$ tilings (summing Eq. 3.4 and Eq. 3.6). However, class-III and class-IV are significantly different in their supplementation patterns, as we will see below.

We have numerically counted all tilings by brute force by using a backtracking algorithm where as only input we use a Boolean matrix that indicates which sides of which tiles fit to which other sides – without any knowledge of classes, edge characteristics etc – up to $m = 6, n = 6$. The resulting numbers exactly correspond to our analytical expression for the number of $m \times n$ tilings (see Table 3.1), thus illustrating that the tilings in class I–IV cover all possible tilings that can be made constructed out of our 34 tiles.

n	$m = 1$	$m = 2$	$m = 3$	$m = 4$	$m = 5$	$m = 6$
1	128					
2	592	1088				
3	4208	4768	8576			
4	32944	33632	37696	67328		
5	262448	263392	267968	298624	531968	
6	2097712	2099168	2104768	2137472	2374912	4226048

TABLE 3.1: Numerically obtained number of possible $m \times n$ -tilings are consistent with our analytical expression (Eq. 3.7).

³The local rotation symmetry of the C_i tiles does not artificially increase the count N_t however, note that $N_t^{II} = 8$ and not 16.

3.4 Counting Supplementation Patterns

In this section we will count the number of different ways in which we can convert (supplement) tile patterns into brick patterns. We show that there are always at least two ways in which we can do this, but for classes II, III, IV there are exponentially many.

Counting Supplemented Angles for Class-I Tilings

Here, we will show that each class-I tiling has two valid supplementation patterns. We recall that class-I tilings contain tiles A , B , C_i and F_i . The supplementation patterns of tile A and B (0 and 7), and the supplementation patterns of tiles C_i (1-6) will be easy to deal with. However, the situation is more complex for tiles F_i , which admit patterns 1, 2, 4, 6, but not 3 or 5. Hence, the admissible supplementation patterns could potentially depend on the orientation of the F_i tiles, which requires a closer inspection of the structure of class-I tilings.

Assume that we specify a pattern of necessary and optional tiles in row 1 and column 1 as in Fig. 3.9.A⁴. First, using triplet completion we

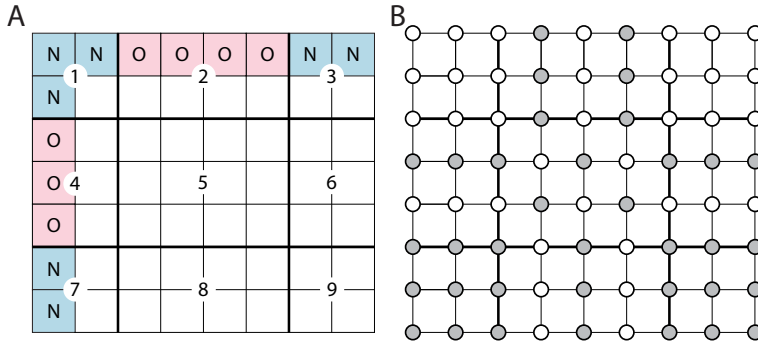


FIGURE 3.9: (A) A generic example of a class-I tiling-pattern: N indicate necessary $\{A, B\}$ -tiles (in blue), O indicates optional tiles $\{C_i, F_i\}$ (in pink). (B) Example of one of the two valid supplementation patterns for the tile pattern in (A).

can show that the missing tiles in sector 1 are necessary tiles, so that

⁴The case that these rows or columns are purely optional can easily be dealt with by focusing on the first rows and columns where necessary tiles occur.

the supplementation pattern of sector 1 is either fully empty (no vertices supplemented) or fully filled (all vertices supplemented); below we assume the former to be the case. In addition it is also easy to show that all necessary tiles in sector 1 are either horizontally or vertically oriented. Finally, triplet completion can be used to show that the tiles in sector 2,4,5,6 and 8 are all optional.

Second, the choice of the supplementation pattern in sector 1 fixes the supplementation pattern of the whole system, as demonstrated by the example in Fig. 3.9.B; i.e. the necessary sectors are ‘monocolor’, the sectors 2, 4, 6, and 8 that separate the necessary sectors are striped (as the optional bricks have always 2 supplemented vertices), and the sector 5 is checkerboard-like.

Third, the supplementation patterns in the necessary sectors are clearly compatible with the necessary tiles, and the supplementation pattern in sector 5 is clearly compatible with all optional tiles - we note in passing that sector 5 exclusively consists of C_i tiles. The potential mismatch between tile pattern and supplementation pattern might occur in the striped sectors: vertically (horizontally) oriented F_i tiles in sector 2, 8 (4, 6) would be incompatible with the supplementation pattern. However, the conservation of edge characteristic prevents this: in rows or columns where A or B tiles are present, all edges have opposite bumps, and this immediately orients the F tiles in sector 2 and 8 horizontally, and in sector 4 and 6 vertically.

Hence: once the supplementation of *one* necessary tile is specified, a unique and compatible supplementation for the whole system arises. Since there are two choices for the supplementation pattern of necessary tiles, this construction yields precisely two (complementary) supplementation patterns for each class-I tiling. Therefore, the number of supplementation patterns in class I, N_s^I , equals:

$$N_s^I = 2. \quad (3.8)$$

Counting Supplemented Angles for Class-II Tilings

Class-II tilings contain only $\{C_i\}$ tiles, which can all be supplemented in six different ways, as is shown in Fig. 2.6. In Fig. 3.10.A we show a class-II brick pattern, where we choose the supplementation of the left-most column of vertices. Doing so fixes the supplementation of all the vertices in the whole pattern, as every column has the opposite pattern of

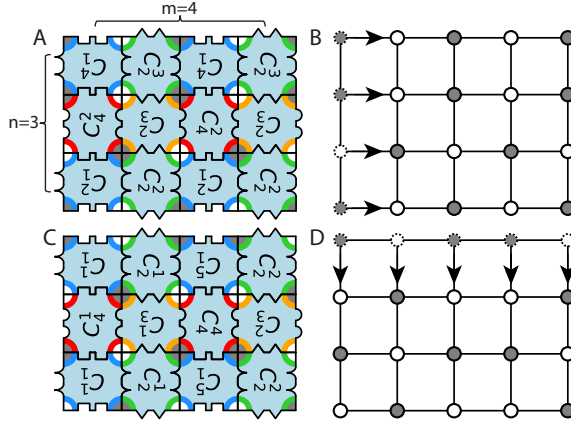


FIGURE 3.10: (A) A 4 by 3 class-II tiling, where we arbitrarily choose the supplementation of the leftmost column of vertices. (B) Supplementation pattern of the brick pattern in (A), the arrows indicate how the left column uniquely determines the adjacent columns. (C) The same 4 by 3 tile pattern, but with a different supplementation pattern. (D) Supplementation pattern of the brick pattern in (C).

its neighbors. In total there are 2^{n+1} ways to choose a supplementation pattern of the leftmost column. The same holds when we choose the supplementation pattern of the top row of vertices, as we did in the example shown in Fig. 3.10.C. In that case every row of vertices has the opposite supplementation pattern of its neighbor (Fig. 3.10.D), and there are 2^{m+1} ways to choose a supplementation pattern on the top row.

We therefore find that we can supplement the vertices in class-II tilings in

$$N_s^{\text{II}} = 2^{m+1} + 2^{n+1} - 2, \quad (3.9)$$

different ways. Here the -2 is necessary to prevent double counting patterns where both the columns and the rows follow alternating patterns.

Counting Supplemented Angles for Class-III Tilings

Class-III tilings can either be horizontally or vertically oriented (see section 3.3), and contain necessary tiles $N = \{E_i, F_i, G_i, H_i, I_i, K_i\}$, and optional tiles $O = \{C_i, D_i, J_i\}$. Let us assume that the tiling is horizontally oriented,

as in Fig. 3.7.B. We conjecture that we can choose the supplementation pattern freely on the left edge of the left column, and then take the supplementation of adjacent columns to alternate. To allow this, we require that tiles with only supplementation patterns 1, 2, 4, 6 (all necessary tiles $\{E_i, F_i, G_i, H_i, I_i, K_i\}$ -tiles, and optional $\{J_i\}$ -tiles) are horizontally oriented. Optional $\{C_i, D_i\}$ -tiles have supplementation pattern 1, 2, 3, 4, 5, 6 and can be oriented arbitrarily.

To show that all $\{E_i, F_i, G_i, H_i, I_i, K_i\}$ -tiles are horizontally oriented in a horizontally oriented class-III tiling, we start by noting that the necessary tile at sector 3 (Fig. 3.7.B) is by definition horizontally oriented, and as all N -tiles have connection numbers $c_n = 1$ and $c_o = 0$ along their East/West edges, sector 4 consists solely of N tiles as well. The orientation of the tiles in sector 4 is also horizontal, which can be seen by considering the edge characteristics of the necessary $\{E_i, F_i, G_i, H_i, I_i, K_i\}$ -tiles, which are $\{oeoe, oeoo, oeeo, oeee, oeee, oeee\}$ respectively (see Table 2.1). Inspection reveals that none of their North/South and East/West sides are compatible, and since the tile in sector 3 is horizontally oriented and these edge characteristics are conserved in every row (and column), all tiles in sector 4 are as well.

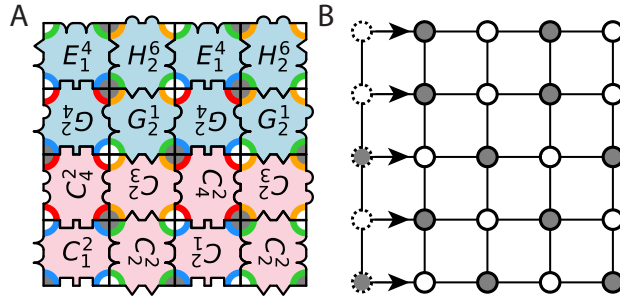


FIGURE 3.11: (A) A horizontally oriented class-III tiling, where we choose the supplementation of the vertices on the left boundary. (B) Supplementation pattern of the brick pattern shown in (A).

When we now look at the North/South edge characteristic of the horizontally oriented tiles in sector 3 and 4, we see that these are all equal to oe . As these edge characteristics are conserved in every column, that means all tiles in sectors-1,2,5,6 also have North/South edge characteristic

oe. Comparison with Table. 2.1 then shows that all optional and necessary tiles in sectors 1,2,5,6 must also be horizontally oriented, except for the C_i -tiles, which can also be vertically oriented. We conclude that the resulting orientations are compatible with the conjectured supplementation pattern, where we can arbitrarily choose the supplementation of the vertices on the right boundary (see Fig. 3.11). This therefore yields,

$$N_{\text{s-hor}}^{\text{III}} = 2^{n+1}, \quad (3.10)$$

supplementation patterns for horizontally oriented class-III patterns. Likewise, we find

$$N_{\text{s-ver}}^{\text{III}} = 2^{m+1}, \quad (3.11)$$

possible supplementations for vertically oriented class-III patterns.

Counting Supplementation Patterns for Class-IV Tilings

Class-IV tilings contain necessary D_i and J_i tiles, and optional C_i tiles. The necessary tiles are either horizontally or vertically oriented, similar to class-III. However, unlike the necessary class-III tiles, which can all be supplemented in only four different ways, the D_i and C_i tiles allow six different supplementations, whereas the J_i tiles are only compatible with the four supplementation patterns where the E and W sides have opposite supplementations (see Fig. 2.6). As a result, the location of the J_i tiles determines the number of allowed supplementation patterns for type-IV tilings.

We now first consider the location and orientation of the various tiles in horizontally oriented class-IV tilings. Consider the leftmost column of such a tiling, filled with a combination of necessary and optional tiles. As shown in Fig. 3.8, the necessary tiles only connect to a single other, necessary, tile along their E/W sides: a necessary tile in the leftmost column thus uniquely determines a row of necessary tiles. Specifically, D_i tiles only connect to J_i tiles and vice versa, so each row of necessary tiles consists of alternating D_i and J_i tiles, each of these oriented horizontally. In addition, optional rows consist of C_i tiles only. As a result, we can distinguish two types of columns: those with J_i tiles, and those without. This allows us to distinguish four subclasses of class-IV tilings, depending on which columns contain J_i tiles:

- Subclass 1: Here J_i tiles occur in all columns. This is the most

common situation, and arises whenever the leftmost column has at least one D_i and J_i tile.

- Subclass 2-4: Here J_i tiles occur in alternating columns; subclass 2 corresponds to even m , where J tiles occur in either the leftmost or rightmost column; subclass 3 and 4 correspond to odd m , with J tiles occurring in neither the left nor rightmost column (subclass 3) or in both columns (subclass 4).

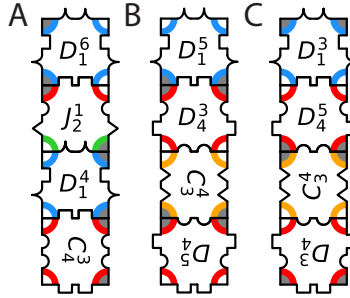


FIGURE 3.12: (A) A column containing at least *one* J_i -tile leads to an alternating supplementation pattern in the horizontal direction. This scenario occurs in subclass-1. (B,C) A column containing no J -tiles allows identical supplementation patterns on the left and right side, as long as the supplementation pattern alternates in the vertical direction. This scenario occurs in subclasses-2,3,4.

We first consider the supplementation pattern of individual columns. For columns containing J_i tiles, the four allowed supplementation patterns of J_i tiles correspond to opposite supplementations at their E and W sides. It is easy to show that adjacent tiles therefore also need opposite supplementation patterns (Fig. 3.12.A), and by iteration, we find that the only allowed supplementation patterns are precisely opposite at E and W sides, leading to 2^{n+1} allowed supplementation patterns for such a column. We note that two of these correspond to patterns where the supplementation of the left and right columns are strictly alternating in the vertical direction, and $2^{n+1} - 2$ where they do not strictly alternate in the vertical direction. In contrast, columns that are free of J_i tiles, allow two additional ‘ladder’ configurations, where the vertices on the left and right side have identical supplementation and are strictly alternating, see Fig. 3.12.B,C. This leads to $2^{n+1} + 2$ supplementation patterns; 4 of these correspond to patterns

where the supplementation of vertices is strictly alternating in the vertical direction, and $2^{n+1} - 2$ to patterns where this is not the case. Hence, the presence of J_i tiles, both determines the subclass and the number of supplementation patterns:

- Subclass 1: J_i tiles occur in each column. This occurs when the left column contains at least one J_i and one D_i tile. Once the supplementations of the left most column of vertices are fixed, adjacent vertex columns have alternating signs, yielding precisely,

$$N_s^{\text{IV-1}} = 2^{n+1}, \quad (3.12)$$

supplementation patterns.

- Subclass 2: Every second column is free of J_i tiles and m is even. This occurs when the left column does not contain both D_i and J_i tiles. To count the number of supplementations, suppose only the odd columns contains J_i , and the even columns do not. Then the left column allows $2^{n+1} - 2$ non-alternating supplementation patterns, and 2 alternating patterns. For each of the non-alternating patterns, the supplementation pattern of all other columns are fixed, yielding $2^{n+1} - 2$ configurations. For each of the 2 alternating patterns, each of the $m/2$ J_i -free columns allow 2 strictly alternating supplementation patterns, yielding $2 \cdot 2^{m/2}$ supplementation patterns. Hence the total number of horizontally oriented subclass-2 supplementation patterns yields:

$$N_{\text{s-hor}}^{\text{IV-2}} = 2^{n+1} - 2 + 2^{m/2+1}. \quad (3.13)$$

- Subclass 3: For odd m with J_i tiles absent from the left and right column, we find $(m + 1)/2$ columns with ladder configurations, leading to:

$$N_{\text{s-hor}}^{\text{IV-3}} = 2^{n+1} - 2 + 2^{(m+1)/2+1}. \quad (3.14)$$

- Subclass 4: For odd m with J_i tiles present from the left and right column, we find $(m - 1)/2$ columns with ladder configurations, leading to:

$$N_{\text{s-hor}}^{\text{IV-4}} = 2^{n+1} - 2 + 2^{(m-1)/2+1}. \quad (3.15)$$

We now count the number of horizontally oriented tilings of each subclass. For even m , we encounter both subclass 1 and subclass 2, for a

total of:

$$N_{\text{t-hor}}^{\text{IV-1,2}} = 8 \cdot (3^n - 1), \quad (3.16)$$

tilings, see Eq. 3.6. The left column of a subclass-2 tiling contains either D_i and C_i tiles, or J and C tiles. Suppose we only have D and C -tiles, then (following the same argument as that leads to Eq. 3.5) we find a total of:

$$8 \cdot \sum_{i=1}^n 2^{n-i} = 8 \cdot (2^n - 1) \quad (3.17)$$

tilings; and the same amount when we have only J_i and C_i tiles in the first column. Hence the total number of horizontally oriented subclass-2 tilings is:

$$N_{\text{t-hor}}^{\text{IV-2}} = 16 \cdot (2^n - 1). \quad (3.18)$$

As the sum of the number of subclass-1 and subclass-2 tilings is given by Eq. 3.16, we readily obtain that:

$$N_{\text{t-hor}}^{\text{IV-1}} = 8 \cdot (3^n - 1) - 16 \cdot (2^n - 1) = 8(3^n + 1 - 2^{n+1}). \quad (3.19)$$

For odd m , we encounter subclass 1, 3 and 4. The left column of a subclass-3 tiling can only contain D_i and C_i tiles, with at least one D_i -tile, leading to:

$$N_{\text{t-hor}}^{\text{IV-3}} = 8 \cdot \sum_i^n 2^{n-i} = 8 \cdot (2^n - 1). \quad (3.20)$$

Similarly, the left column of a subclass-4 tiling only contains J_i tiles and C_i -tiles, and cannot consist of C_i tiles only, leading to:

$$N_{\text{t-hor}}^{\text{IV-4}} = 8 \cdot (2^n - 1). \quad (3.21)$$

Hence, the number of subclass-1 tilings for odd m equals:

$$N_{\text{t-hor}}^{\text{IV-1}} = 8 \cdot (3^n - 1) - 2 \cdot 8 \cdot (2^n - 1) = 8 \cdot (3^n + 1 - 2^{n+1}). \quad (3.22)$$

We finally combine the results for the number of tilings and supplementation patterns per subclass to obtain $H_{\text{b-hor}} = N_{\text{t-hor}} \cdot N_{\text{s-hor}}$, the number of horizontally oriented brick patterns in each subclass:

- subclass-1 (even m),

$$H_{\text{b-hor}} = 8 \cdot (3^n + 1 - 2^{n+1}) \times 2^{n+1}; \quad (3.23)$$

- subclass-1 (odd m),

$$H_{\text{b-hor}} = 8 \cdot (3^n + 1 - 2^{n+1}) \times 2^{n+1}; \quad (3.24)$$

- subclass-2 (even m),

$$H_{\text{b-hor}} = 16 \cdot (2^n - 1) \times (2^{n+1} - 2 + 2^{m/2+1}); \quad (3.25)$$

- subclass-3 (odd m),

$$H_{\text{b-hor}} = 8 \cdot (2^n - 1) \times (2^{n+1} - 2 + 2^{(m+1)/2+1}); \quad (3.26)$$

- subclass-4 (odd m),

$$H_{\text{b-hor}} = 8 \cdot (2^n - 1) \times (2^{n+1} - 2 + 2^{(m-1)/2+1}). \quad (3.27)$$

The total number of class-IV $m \times n$ tilings and brick patterns can be obtained by adding the horizontal and vertically oriented patterns, distinguishing different subtypes depending on the parity of both m and n .

3.5 Counting Folding Branches

A single flat 4-vertex has two distinct folding branches, which each have a single, continuous degree-of-freedom. On each of these folding branches one of the four fold angles is opposite in sign to the other three. These two folds are called ‘odd folds’, and they straddle a common ‘odd plate’, for which the corresponding sector angle satisfies the inequality: $\alpha_i + \alpha_{i+1} < \alpha_{i+2} + \alpha_{i+3}$ [28]. Analytical expressions for the relations between the fold angles on these two fold branches are given in appendix A.

In this section we will determine how the two folding branches of a single vertex determine the number of independent folding branches per tile, and ultimately, the number of folding branches of crease patterns in class I–IV. We start by counting the folding branches per tile, by reconsidering the underlying operator quads (Eq. 2.9–2.19). So far, we have assumed that all operators refer to folding motion on the same branch, but now dress these operators with a superscript I or II, to indicate their respective folding branch. The number of folding branches per tile is now equal to the number of combinations of I and II labels in the operator quads that lead

to identities. We can group all operator quads in three groups: the first group contains the C_i -tiles (Eq. 2.11) which combine the operators $\rho_{i,i-1}^{I,II}$. To obtain an identity, we need to pair adjacent operators. For example,

$$\rho_{14}^I \rho_{41}^I \rho_{14}^{II} \rho_{41}^{II} = I, \quad (3.28)$$

which corresponds to tile $\{C_1\}$, which represents a rigidly foldable configuration as $\rho_{14}^I \rho_{41}^I = \pm I$, and $\rho_{14}^{II} \rho_{41}^{II} = \pm I$.⁵ Conversely,

$$\rho_{14}^I \rho_{41}^{II} \rho_{14}^I \rho_{41}^{II} \neq I \quad (3.29)$$

does not represent a rigidly foldable configuration, as the folding operators on different branches do not ‘annihilate’ in pairs. There are six distinct choices for the folding branches of C_i tiles where ‘adjacent operators’ are on the same branch - tiles $\{C_i\}$ can therefore be folded into six different configurations. We show these six configurations in Fig. 3.13.A.

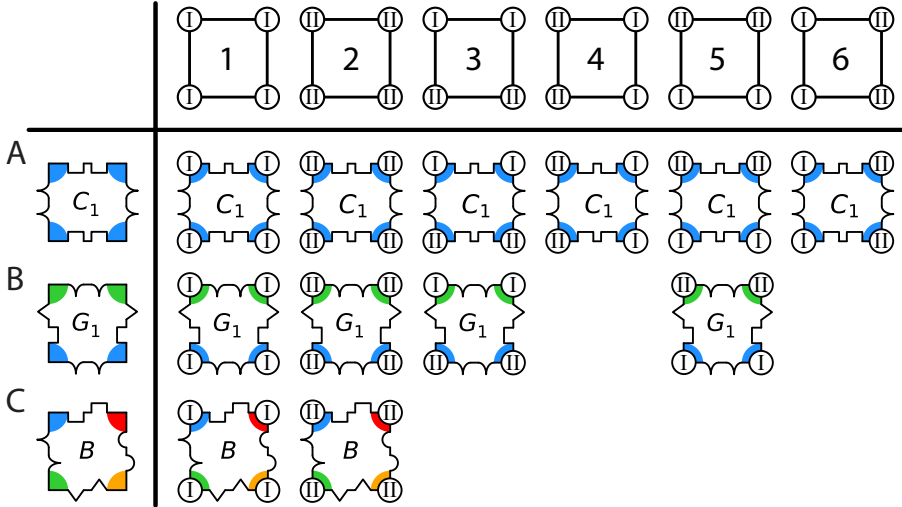


FIGURE 3.13: The allowed folding branches for all tiles. (A) The branches of tile C_1 can take six different configurations. (B) For tiles $\{D_i, E_i, F_i, G_i, H_i, I_i, J_i, K_i\}$ the branches of their vertices take four different configurations. (C) Tiles $\{A, B\}$ can only take two configurations.

⁵Here the \pm sign reflect the fact we left out which operators are supplemented, we will come back to this on the next page.

Second, there are tiles $\{D_i, E_i, F_i, G_i, H_i, I_i, J_i, K_i\}$, which contain pairs of distinct operators, and which only allow four choices of the vertex branches. These correspond to the choices of branch I or II for each pair of vertices. These Kokotsakis meshes can thus be folded into four different configurations. For example, Eq. 2.15 with $i = 1$,

$$\rho_{41}^{II} \rho_{14}^{II} \rho_{21}^I \rho_{12}^I = I, \quad (3.30)$$

but,

$$\rho_{41}^{II} \rho_{14}^I \rho_{21}^I \rho_{12}^{II} \neq I. \quad (3.31)$$

The four possible configurations are shown in Fig. 3.13.B.

Third, there remain the tiles $\{A, B\}$ related to Eq. 2.9 and Eq. 2.10, which can only be folded into two different configurations for the identity of Eq. 2.9 or Eq. 2.10 to hold, as all of the vertices need to be in the same folding branch. For example,

$$\rho_{43}^I \rho_{32}^I \rho_{21}^I \rho_{14}^I = I, \quad (3.32)$$

see Fig. 3.13.C.

We note here that the supplementation pattern is not relevant for counting the number of branches, although it is important for the corresponding mountain valley pattern. Similarly, the choice of the odd folds (i.e. the choice of the numerical values of $\alpha_i - \alpha_4$) determines the specific M-V patterns. Examples of these are shown in Fig. 3.14. This illustrates the power of separately solving for the choice of branches for each vertex that solve the loop condition, Eq. 2.8, and the supplementation patterns which satisfy the sum rule, Eq. 2.1.

Counting Folding Branches for Class-I Tilings

Class-I tilings exhibit two distinct folding branches:

$$N_b^I = 2. \quad (3.33)$$

This is because the choice of supplementation patterns and the choice of branches are identical combinatorial problems in class I. Hence, the branches of one of the necessary class-I tiles ($\{A\}$ or $\{B\}$) immediately determines the folding branch of all other vertices.

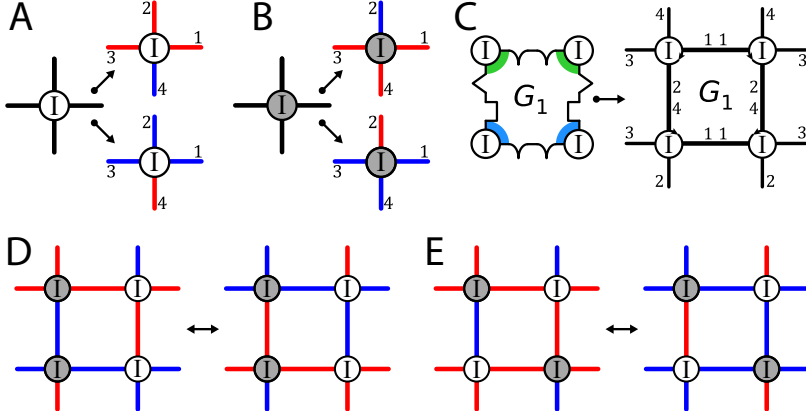


FIGURE 3.14: Mountain-Valley patterns. (A) Assuming that ρ_4 is the odd fold at branch I, a single vertex can be in two M-V configurations. (B) The odd fold on branch I of the supplemented vertex is ρ_2 (opposite to ρ_4). (C) The folding angle configuration for tile G_1 . (D) For a given supplementation pattern, two corresponding and opposite M-V patterns exist. (E) A different supplementation pattern yields two different M-V patterns.

Counting Folding Branches for Class-II Tilings

The total number of folding branches of an $m \times n$ class-II tiling is:

$$N_{\text{b}}^{\text{II}} = 2^{m+1} + 2^{n+1} - 2. \quad (3.34)$$

This is because the choice of supplementation patterns and branches are identical combinatorial problems in class II: C_i tiles have identical configurations for the choice of supplementation and the choice of folding branch at each vertex.

Counting Folding Branches for Class-III and Class-IV Tilings

For class-III we again observe that the number of supplementation patterns equals the number of folding branches. We find,

$$N_{\text{b-hor}}^{\text{III}} = 2^{m+1}, \quad (3.35)$$

for a horizontally oriented class-III pattern, analogous to Eq. 3.10.

Class-IV contains the only tiles for which the number of supplementation patterns differs from the number of branch patterns: tiles D_i . These can be supplemented in six different ways, but have only four possible branch configurations. The combinatorial problem of choosing the branches of a class-IV tiling is therefore identical to the problem of counting branches for class-III tilings. This means that for an $m \times n$ class-IV pattern we have:

$$N_{\text{b-hor}}^{\text{IV}} = 2^{m+1}. \quad (3.36)$$

Conversely, when a class-III or class-IV pattern is vertically oriented, we have:

$$N_{\text{b-ver}}^{\text{III}} = N_{\text{b-ver}}^{\text{IV}} = 2^{n+1}. \quad (3.37)$$

3.6 Summary and Outlook

We summarize the results of this chapter, in Table 3.2. Here we show the classification of the 34 tiles into four classes, the number of tile patterns N_t within each class, the number of possible supplementations into brick patterns N_s , and the number of possible folding branches N_b . Note that for class-III and class-IV, the expressions in the table are for horizontally oriented patterns. Expressions for vertically oriented patterns can be found by interchanging m and n .

In the next chapter, we aim to design bipotent crease patterns where we can change the folded shape of two folding branches *independently*. Table 3.2 shows that class-II patterns can not be used with this goal in mind, as the number of tilings is fixed at 8. The number of supplemented angles $N_s = 2^n + 2^m - 2$ also does not form a large enough design space to facilitate this, as any changes in the supplementation pattern always occur along either the horizontal, or the vertical direction. Class-III and class-IV patterns have a larger design space, where the number of possible patterns scales exponentially with n (m). However, this still only allows us to change the tiles on the left (top) side of the pattern, which does not allow us to independently tune the folding shape of two or more branches. The only remaining class is therefore class-I, where we see that the number of tilings scales as $N_t \sim 2^{m+n}$. This reflects the fact that we can independently choose the tiles on the top row and left column of the pattern; where the choice of tiles in these locations directly changes the shape of the two folding branches. In the next chapter we will show how to design the two

folded shapes of class-I patterns, by changing the composition of the top row and left column.

Class	Necessary Tiles	Optional Tiles	Tilings (N_t)	Sup. Angles (N_s)	Branches (N_b)
I	$\{A, B\}$	$\{C_i, F_i\}$	$8(2^m - 1)(2^n - 1)$	2	2
II	$\{C_i\}$	—	8	$2^{m+1} + 2^{n+1} - 2$	$2^{m+1} + 2^{n+1} - 2$
III [†]	$\{E_i, F_i, G_i, H_i, I_i, K_i\}$	$\{C_i, D_i, J_i\}$	$8(8^n - 3^n)$	2^{n+1}	2^{n+1}
IV-1 (m even) [†]	$\{D_i, J_i\}$	$\{C_i\}$	$8(3^n + 1 - 2^{n+1})$	2^{n+1}	2^{n+1}
IV-1 (m odd) [†]	$\{D_i, J_i\}$	$\{C_i\}$	$8(3^n + 1 - 2^{n+1})$	2^{n+1}	2^{n+1}
IV-2 (m even) [†]	$\{D_i, J_i\}$	$\{C_i\}$	$16(2^n - 1)$	$2^{n+1} - 2 + 2^{\frac{m+2}{2}}$	2^{n+1}
IV-3 (m odd) [†]	$\{D_i, J_i\}$	$\{C_i\}$	$8(2^n - 1)$	$2^{n+1} - 2 + 2^{\frac{m+3}{2}}$	2^{n+1}
IV-4 (m odd) [†]	$\{D_i, J_i\}$	$\{C_i\}$	$8(2^n - 1)$	$2^{n+1} - 2 + 2^{\frac{m+1}{2}}$	2^{n+1}

TABLE 3.2: Table summarizing the results of sections 3.3, and 3.4, 3.5. The symbol [†] indicates the pattern is horizontally oriented, expressions for vertically oriented patterns can be obtained by $m \leftrightarrow n$

3.6. SUMMARY AND OUTLOOK

RATIONAL DESIGN OF ORIGAMI PATTERNS

4.1 Introduction

In the previous chapters we showed that by converting the problem of rigid foldability into a discrete tiling problem, we can fully characterize and count all the possible crease patterns which can be made using a single vertex, its supplement, and their two mirror images. Doing so we uncovered new, space-filing periodic tilings –e.g. the tiling in Fig. 3.1– as well as a vast array of aperiodic tilings.

In this section we aim to rationally design origami patterns using the same discrete tiling strategy. We first show that we can create periodic or non-periodic crease patterns, starting from a periodic class-I tiling in section 4.2. Then we focus on class-I patterns, which allow the greatest design space of the four different classes, as the number of class-I patterns ($N_t^I = 8 \cdot (2^m - 1) \cdot (2^n - 1)$) scales exponentially with both m and n . In section 4.3 we show how to program class-I patterns such that we obtain strips that can be folded into shapes with a pre-programmed curvature. In section 4.4 we then show how to extend this design strategy to $m \times n$ sheets, which can be folded into two different, pre-programmed shapes. The result is a multishape material – this is unique for origami, where one usually designs structures with only one target shape in mind. Finally, we show experimental realizations of such multishape sheets, in the form of lasercut Mylar™ sheets.

4.2 Space-Filling Tilings

In this section we will address the issue of space-filling tilings, where we will focus specifically on class-I patterns. The first requirement for a crease pattern to be space-filling is for its corresponding tile pattern to be space filling. In Fig. 4.1.A we show a tile-pattern of which the top and bottom fit together, but the left and right side do not – this pattern therefore can not be turned into a space-filling crease pattern. In Fig. 4.1.B we replaced the leftmost columns with tiles which create a space filling tile pattern.

In Fig. 4.2.A we convert the 4×4 pattern of Fig. 4.1.B into a 12×12 crease pattern using nine unit cells. To do so, we fix 11 degrees of freedom: the crease lengths $\{t_i\}$ and $\{l_i\}$ (8 d.o.f.) and the sector angles $\{\alpha_i\} = \{60^\circ, 90^\circ, 135^\circ, 75^\circ\}$ (3 d.o.f., as $\sum \alpha_i = 2\pi$). We can clearly see that the resulting pattern is not space-filling. This is because the lengths of the top and left side of the crease pattern, do not match those of the bottom and right side. To ensure matching lengths, we require that $b_i = t_i$ and $r_i = l_i$; fixing $\{\alpha_i\}$. These yield eight equations for the eight degrees of freedom $\{t_i\}$ and $\{l_i\}$. We solve these nonlinear coupled equations numerically (by means of a Python script with standard minimization libraries, `scipy.optimize.minimize`, using the Nelder-Mead method). The result is shown in Fig. 4.1B, yielding a periodic, space filling crease pattern.

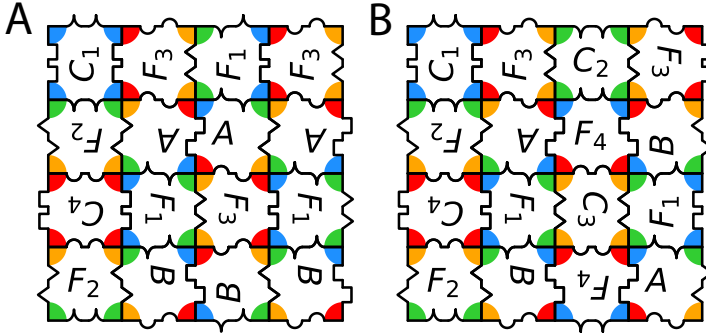


FIGURE 4.1: (A) A class-I pattern that does not tile the plane: although the top and bottom side of this tiling fit together, the left and right side do not. (B) A class-I pattern which tiles the plane, and can potentially also tile the plane once converted into a real-space crease pattern, see Fig. 4.2.

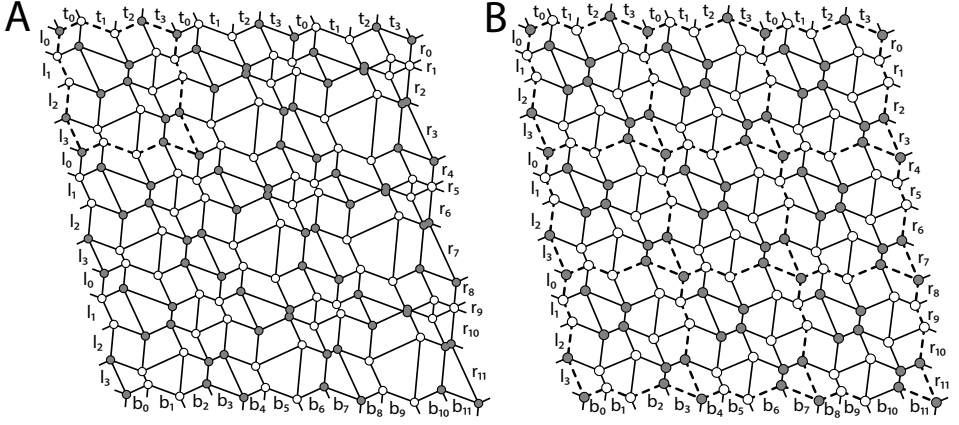


FIGURE 4.2: (A) Real space version of the tile pattern shown in Fig. 4.1, where the lengths of the top (t_i), and the left side (l_i) are not specifically tuned, which leads to a non-space filling pattern. (B) Real space version of the tile pattern shown in Fig. 4.1b, where the lengths of the top (t_i), and the left side (l_i) are tuned such that the pattern is space-filling. Dashed lines indicate unit cells. Both patterns have $\{\alpha_1, \alpha_2, \alpha_3, \alpha_4\} = \{60^\circ, 90^\circ, 135^\circ, 75^\circ\}$ for the unsupplemented vertex (indicated in white).

4.3 Designing Origami Strips with One Target Shape

In this section we will show that we can design one of the two folding-branches of a class-I tiling in such a way such that it folds into a sheet with a predefined curvature along one direction. The other folding branch folds into a cylinder. To illustrate how we construct origami patterns which lead to certain predefined shapes, we depicted an $m = 13, n = 5$ class-I tiling in Fig.4.3.A. The columns in this pattern consist solely of A -tiles, B -tiles, or F_i -tiles, and have a periodicity of 2 in the vertical direction. The colors purple and orange in this figure indicate curvature for the non-cylindrical folding branch. Here purple indicates the sheet curving upward, and orange indicates the sheet curving downward (or vice versa). This is demonstrated in Fig.4.3.B, where a realization of the tiling of Fig.4.3.A is shown with sector angles $\alpha_i = \{60^\circ, 75^\circ, 120^\circ, 105^\circ\}$, which is the base vertex used for all the subsequent crease patterns in this section. This corresponds to a flat foldable vertex, but one our approach works equally well for generic vertices. The red lines indicate mountain folds, whereas

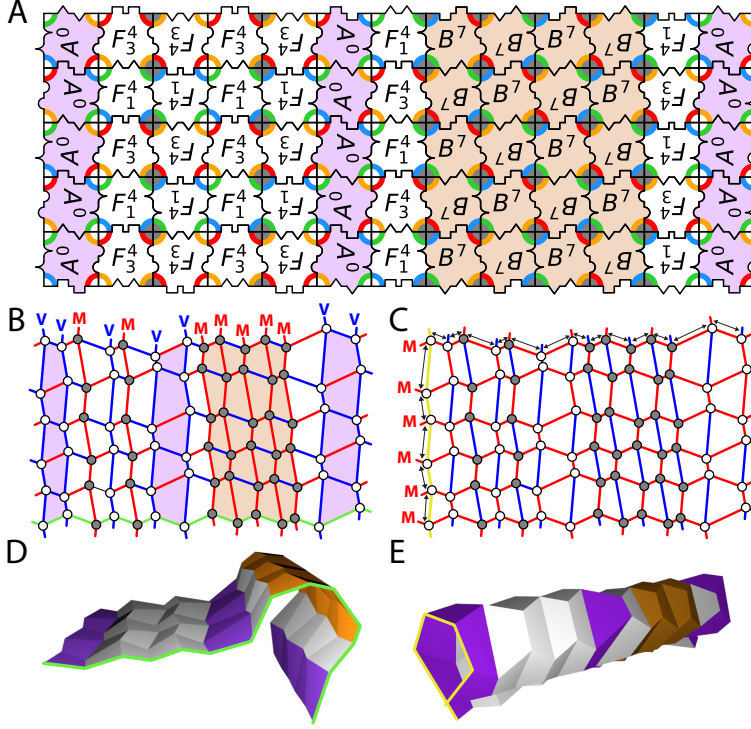


FIGURE 4.3: (A) Class-I tiling, with columns consisting out of bricks with identical letters. Purple columns contain A -tiles, whereas orange columns contain B -tiles. These determine the curvature of the pattern when folded along the vertical direction, see (B,D). (B) MV pattern associated with the pattern in (A), when folded along the vertical direction. (C) MV pattern associated with the pattern in (A), when folded along the horizontal direction. (D,E) 3D shapes of folded states of the patterns depicted in (B,C) were calculated using software from [63].

the blue lines indicate valley folds. A 3D visualization of this pattern is depicted in Fig.4.3.D, showing that we can adjust the curvature of the sheet by programming the sequence of bricks in the horizontal direction.

We see that the purple columns, consisting out of A -tiles, are lined left and right by valley folds (V). On the contrary, we see that the orange columns, consisting out of B -tiles, are lined left and right by mountain folds (M). Consecutive columns of B tiles, such as in the middle of the

pattern, therefore induce a downward curvature, whereas consecutive columns of A -tiles induce a positive curvature (or the other way around, as every MV-pattern has a mirrored counterpart). Furthermore we notice that the F -tiles always have opposite fold signs left and right. Multiple adjacent columns of F -tiles do not induce curvature, but form a corrugated sheet, like many origami patterns do (such as Miura-ori). Lastly, we observe from Fig.4.3.A that when mixing F tiles with A and B tiles, an even number of consecutive F -tiles is surrounded left and right by the same kind of tile (either A or B), this can be seen in column 2–5 in Fig.4.3.A. An odd number of consecutive F -tiles is surrounded left and right by both an A -tile and a B tile.

Altogether we then see that class-I tilings can be used to program any arbitrary code of fold signs along the vertical (or horizontal) direction. We do this by choosing the right combination of A , B , and F -tiles. In this case the pattern can be written as,

$$VVMVMVMVMVMVMVV. \quad (4.1)$$

Different combinations of tiles can result in nearly any of the 2^{m+1} different patterns, where n is the number of columns of tiles. The only patterns that can not be created within class-I itself are the ones where mountains and valleys alternate throughout the sheet ($VMBM \dots$). The corresponding tiling would be comprised solely of F tiles, and therefore is not a class-I, but a class-III tiling. The total number of possible MV patterns that we can choose from is therefore,

$$2^{m+1} - 2. \quad (4.2)$$

Using the design strategy of alternating columns (or rows) of A , B , and F -tiles ensures that one of the two branches still folds into a cylinder, which is shown in the MV pattern of Fig.4.3.C, and the 3D visualization of Fig.4.3.E. Note that the left edge of the pattern in Fig.4.3.C is colored green, corresponding to the green edge in Fig.4.3.E. In the next section we will show that we can also modify this cylindrical folding branch, by adding C tiles.

First however, we will extend on the principle of using A and B -tiles to introduce curvature into certain places to target a more complicated shape. In Fig.4.4.A we show a 67 by 4 vertex quadrilateral mesh, converted from a 66 by 3 tile pattern. Note that here we count the *internal* vertices and

internal tiles, as we can arbitrarily reshape the quadrilaterals on the edge of the this pattern without affecting the folding motion. Fig.4.4.B reveals that the mesh depicted in Fig.4.4.A folds into the Greek-letter β . Note that the green edge in Fig.4.4.A corresponds to the green edge in Fig.4.4.B. We designed the pattern in Fig. 4.4.A to consist of flat areas when folded, corresponding to columns of F -tiles. These are interspersed with A and B -tiles to create curves with varying radius of curvature. For example, the ratio of B to F columns in the top loop of the β is 1 : 2, whereas the ratio of B to F tiles in the bottom loop of the letter β is 1 : 4. The resultant 3D shape therefore shows that the radius of curvature of the bottom loop is approximately twice as big as the radius of curvature of the top loop, throughout the folding motion of the sheet. This can also be seen in Fig.4.5. Here several snapshots of the crease pattern depicted in Fig.4.4.A are taken throughout its folding motion, as seen from the side. Note that the folding motion is restricted, as eventually the sheet comes into contact with itself. In principle this strategy –varying the ratio of A and B to F -tiles– can be

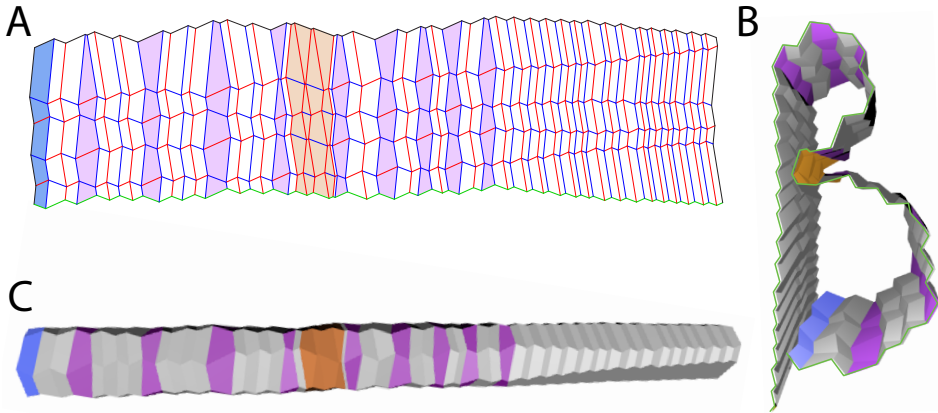


FIGURE 4.4: (A) A 67 by 4 (internal) vertex quadrilateral mesh, which is a realization of 66 by 3 internal tile pattern (not shown here). By choosing the position of the A , B , and F tiles we can program the curvature of the sheet when folded. (B) 3D visualization of the MV pattern depicted in (A), revealing this mesh folds into the shape of the letter β . (C) 3D visualization of the mesh shown in (A) when folded into the cylinder configuration (MV pattern not shown here). 3D folded shapes in figures (B,C) calculated using software from [63].

extended to achieve any kind of ratio between the curved parts of the 3D shape. Furthermore, we can tune the $m + n$ continuous degrees of freedom of the mesh, which are indicated in Fig.4.3.D.

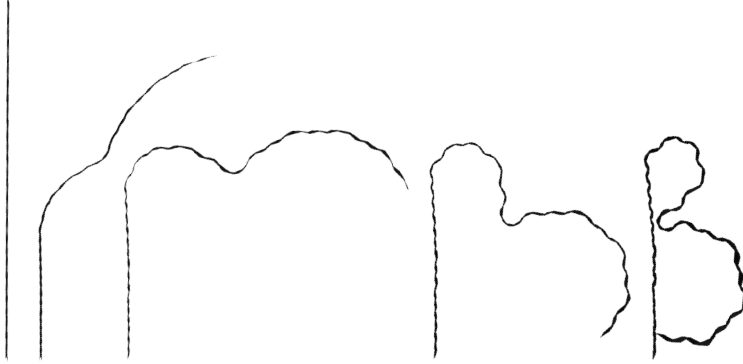


FIGURE 4.5: Side-view of the folding process leading up to the final 3D shape depicted in Fig. 4.4.B, 3D folded shapes calculated using software from [63]. A movie illustrating the folding process can be found online.



4.4 Designing Origami Sheets with Two Target Shapes

The strategy explained in the previous section can be extended to tune the shape of both folding branches of a class-I tiling. An example of this is shown in Fig.4.6.A, where we show a class-I brick tiling. We can choose any pattern of A , B and F tiles on both the top and the left edge. The rest of the $(m - 1)(n - 1)$ tiles in the pattern, masked by a partially translucent layer, are fixed by this choice. Note that the resultant pattern also contains C tiles in the interior. These are located wherever we find a F tile on the left edge in the corresponding row, and top edge in the corresponding column.

In Fig.4.6.B we show a realization of the tiling of Fig.4.6.A. The mountain valley pattern here is the one that corresponds to the vertically corrugated folding branch. A 3D visualization of this MV pattern is depicted in Fig.4.6.C. Contrastingly, Fig.4.6.D depicts the same quadrilateral mesh as in Fig.4.6.B, but with the mountain valley pattern of the horizontally corrugated folding branch. A 3D visualization of the folded state of this

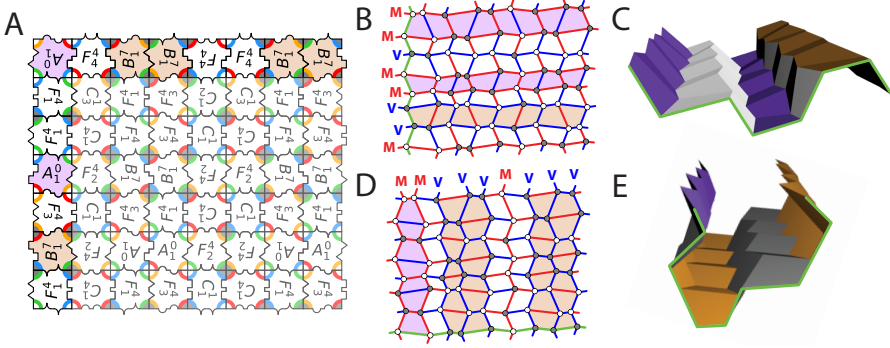


FIGURE 4.6: (A) A 7 by 8 tile class-I tiling, containing all 10 A , B , C_i , and F_i tiles. (B) Horizontally corrugated shape, where the sign of the folds along each row is identical. (C) 3D visualization of the mesh shown in (B). (D) Vertically corrugated shape, where the sign of the folds along each column is identical. (E) 3D visualization of the mesh shown in (D). 3D folded shapes in (D,E) calculated using software from [63]. Green lines in (B,C) and (D,E) are a visual aid to indicate the orientation of the patterns in their flat and folded configurations.

MV pattern is depicted Fig.4.6.E. Clearly, the pattern of tiles along the left edge determines the curvature pattern of one folding branch; the pattern along the top edge determines the curvature pattern of the other folding branch. Hence, this strategy allows to independently design two 3D shapes.

To illustrate the possibilities of this combinatorial origami design, we designed a 38×38 class I brick pattern, shown in Fig. 4.7. Here the A and B -tiles are highlighted in purple and orange (respectively), to indicate the areas where the corresponding crease pattern will develop curvature. In Fig. 4.8.A we show the resulting crease pattern, using a base vertex with angles $\alpha_i = \{60^\circ, 105^\circ, 120^\circ, 75^\circ\}$. This pattern was designed with two target shapes: the letter α , and the letter ω . The bottom edge of this pattern (indicated in red) folds into the shape of the letter ' α ' when folded along the horizontal direction, as can be seen in the computer visualization in Fig. 4.8.B, and the rest of sheet is an extrusion of this shape. When folded along the vertical direction, the left edge of this pattern (indicated in green) folds into the shape of the letter ' ω ', as can be seen in the computer visualization in Fig. 4.8.D.

To demonstrate that this strategy works to fold sheets of material into

multiple different target shapes, we lasercut the pattern in Fig. 4.8 into two 50 cm by 60 cm Mylar™ sheets, with a thickness of 0.2 mm. Here we program the laser cutter to scorch the crease pattern 0.1 mm deep into the sheet. These two identical sheets are then manipulated by hand to into

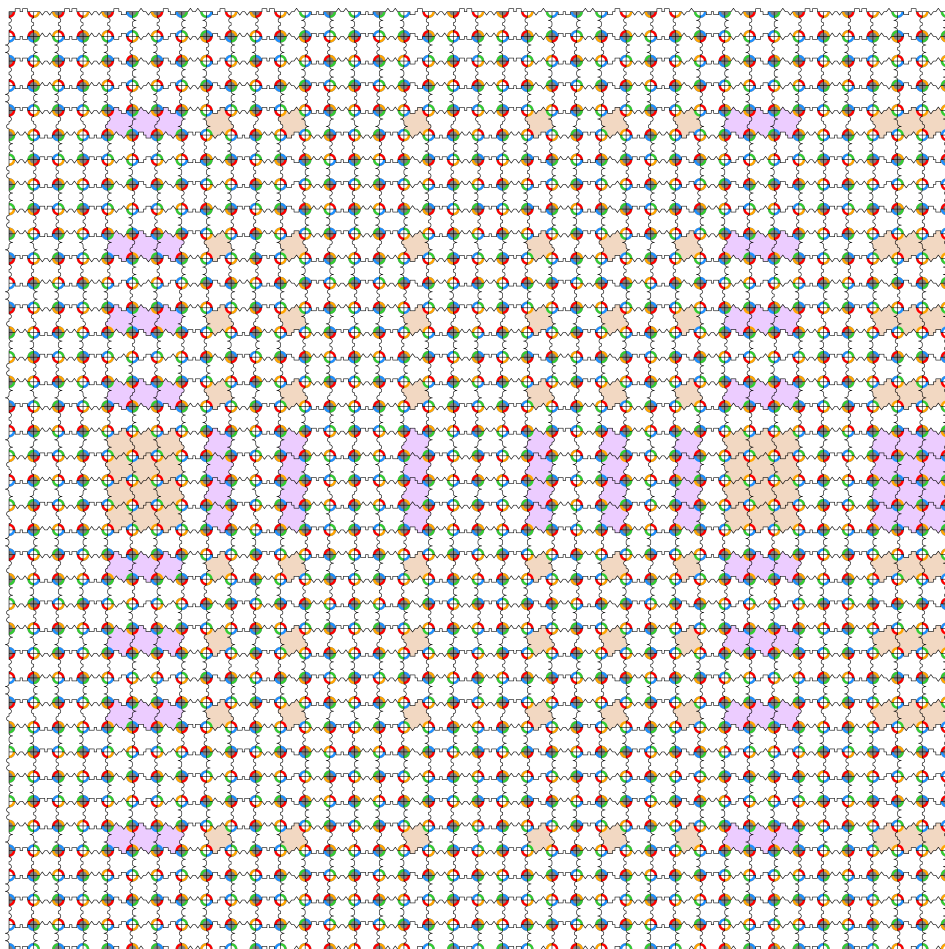


FIGURE 4.7: Brick pattern corresponding to the crease pattern shown in Fig. 4.8.A, where the letters indicating the brick type are omitted. *A*-tiles are highlighted in purple, whereas *B*-tiles are highlighted in orange. We encourage the reader to download the high-resolution version of this image.



the two different target shapes. Final folded shapes are shown in Fig.4.8.C and Fig.4.8.E. We note the close resemblance to the shapes in the computer simulations of Fig.4.8.B,D. Finally, we note that the shapes depicted in Fig. 4.8.C,E share the same underlying 2D structure, and it is therefore

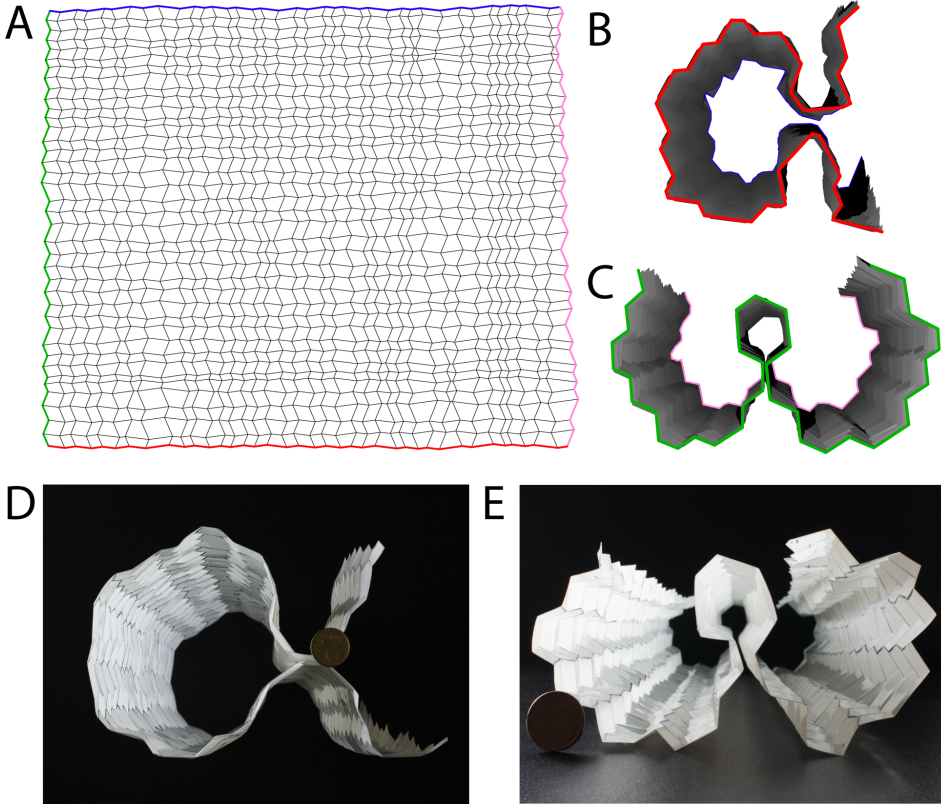


FIGURE 4.8: (A) A 38 by 38 tile class-I (37 by 37 internal vertices) class-I tiling, created from the brick pattern shown in Fig. 4.7, with $\alpha_i = \{60^\circ, 105^\circ, 120^\circ, 75^\circ\}$. (B) 3D visualization of the final folded state of the pattern displayed in (A) when folded in the horizontal direction, representing the letter ‘ α ’. (C) Lasercut Mylar™ sheet, folded into the same shape as in (B). Five cent euro coin for scale. (D) 3D visualization of the final folded state of the pattern displayed in (A) when folded in the vertical direction, representing the letter ‘ ω ’. (E) Lasercut Mylar™ sheet, folded into the same shape as in (D). Five cent euro coin for scale. 3D folded shapes in (B,D) calculated using software from [63].

in principle possible for the shape of Fig. 4.8.B to morph continuously into the shape depicted in Fig. 4.8.C (via the flat, unfolded state). Movies illustrating the folding process of both shapes are available for download.



We conclude that our design strategy allows us to create a single 2D crease pattern, which has two mountain valley patterns with corresponding 3D shapes. Both of these shapes can be tuned such that they have an arbitrary mountain-valley arrangement along one direction. This allows for the creation of multishape origami patterns, which is new in origami design, where usually one only targets a single shape [17–19, 34, 64, 65].

MULTISTABILITY OF NON-FLAT VERTICES

5.1 Introduction

One appealing feature of many origami patterns is that they readily exhibit multistable behavior. For example: a simple waterbomb pattern, consisting of folds of alternating sign coming together at a vertex is generically bistable [66, 67]. Here the flexibility of the folds and the flexibility of the material work together to create one stable shape at zero elastic energy, and one stable shape at finite energy. Other examples of bistability also exploit the finite stiffness of the plate material to achieve bistable structures [68, 69], whereas yet other studies focus on strictly rigid folding structures dressed by linear or torsional springs [28, 34, 70, 71]. Both of these approaches however, generally consider only bistable behavior [28, 34, 66, 67, 70].

A Euclidean 4-vertex which is made out of paper –or any other flat material– has two folding branches, which connect at the flat state [28]. As a consequence, when one of the fold angles is fixed, the vertex can be in two distinct configurations. It is therefore straightforward to make a bistable element out of a 4-vertex mechanism, by putting a single torsional spring on any of the four folds. When additionally putting springs on the three remaining folds, it is theoretically possible to create tri-, quad-, penta-, and hexa-stable vertices [28]. However, these more complex energy landscapes only occur in a small region of the phase space spanned by the sector angles of the vertex and the spring rest angles and stiffnesses. Moreover, most of

the energy minima are shallow. It is therefore difficult to turn these designs into actual tri-stable vertices.

In this chapter we aim to create experimentally robust *tristable* 4-vertices. To do so, we opt for a novel approach, based on non-flat, non-Euclidean 4-vertices. For these, the sum of sector angles $\sum \alpha_i$ is unequal to 2π . Such non-flat vertices occur in non-developable origami structures, which typically consist of cells which are glued together, such as eggbox patterns [72], tubular origami structures [54], as well as 3D-origami stackings [26].

For a non-Euclidean vertex, the flat state is no longer accessible by rigidly folding the vertex. As a consequence, the two folding branches split apart [73], as we discuss below, and the only way to switch from one branch to another is by ‘popping through’ the vertex. This branch splitting will be harnessed to create a vertex with two global ($E = 0$) minima on one folding branch, and one additional *local* minimum ($E > 0$) on the other folding branch.

In this chapter we experimentally demonstrate these tristable vertices. In section 5.2 we explain the theory behind non-flat 4-vertices, and under which conditions they are tristable. In section 5.3 we show how we fabricate the vertices by means of 3D printing, as well as our experimental setup. In section 5.4 we show our results. Based on these experiments, we calculate energy curves, which show clear tristable behavior. We compare these to our theoretical predictions in section 5.4.4 and find good agreement. Hence we present a generic and robust route to fabricate tristable vertices.

5.2 Non-Flat 4-Vertices

In this section we will show how the two branches of a flat 4-vertex separate when the four sector angles of the vertex add up to slightly less, or slightly more, than 2π . The separation of the two folding branches effectively creates an energy barrier between the two folding branches, which we harness to design tristable 4-vertices.

5.2.1 Phenomenology

In order to understand the folding behavior of a non-flat vertex, we first consider the two folding branches of a flat vertex. In Fig. 5.1.A we show

a flat 4-vertex with sector angles α_i for a vertex with sector angles $\alpha_i = \{\pi/3, \pi/2, 3\pi/4, 5\pi/12\}$ for $i = 1, 2, 3, 4$, which is the same geometry as the vertex in Fig. 5.1.A. When we fold this 4-vertex it can be modeled as a mechanism which has a single continuous degree of freedom, and two folding branches that meet in the flat state. Spherical trigonometry can be used to derive the relationships $\rho_i(\rho_j)$ on the two principal folding branches, which we name branch-I and branch-II. On branch I, the sign of ρ_4 is opposite to all others, whereas on the branch II the sign of ρ_1 is opposite to all others. These two folds, ρ_4 and ρ_1 are so called ‘odd-folds’, which are found on either side of the ‘odd plate’, which is defined as the plate for which the corresponding sector angle satisfies [28],

$$\alpha_i + \alpha_{i+1} < \alpha_{i+2} + \alpha_{i+3}, \quad (5.1)$$

$$\alpha_i + \alpha_{i+3} < \alpha_{i+1} + \alpha_{i+2}. \quad (5.2)$$

We further subdivide these in branches I^+ and II^+ , for which three out of the four folds are positive in sign, as well as I^- and II^- , for which three out of the four folds are negative in sign. In Fig. 5.2.A we plot the relationships $\rho_i(\rho_1)$.

From the folding branches in Fig. 5.2.A it is evident that putting a torsional spring on any of the four folds ρ_i results in a bistable vertex. A

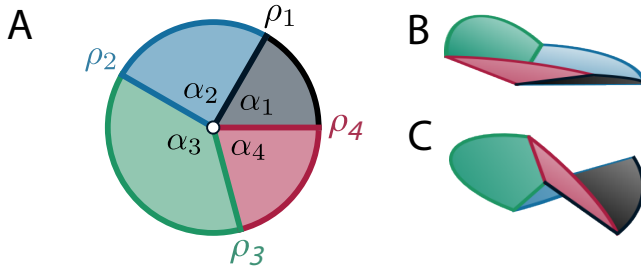


FIGURE 5.1: (A) Flat 4-vertex with sector angles $\alpha_i = \{\pi/3, \pi/2, 3\pi/4, 5\pi/12\}$ (B) Vertex where the α_i of A are uniformly shrunk by a factor $f < 1$ ($\alpha'_i = f \cdot \alpha_i$) such that $\sum \alpha_i < 2\pi$. As depicted, this vertex has assumed a ‘hat-shape’, where all the ρ_i are identical in sign, which is not possible with flat vertices. (C): Vertex where the α_i of A are uniformly expanded by a factor $f > 1$ such that $\sum \alpha_i > 2\pi$. As depicted, this vertex has assumed a ‘saddle-shape’ where the ρ_i alternate in sign. This alternation is not possible with flat vertices. Figure from [74].

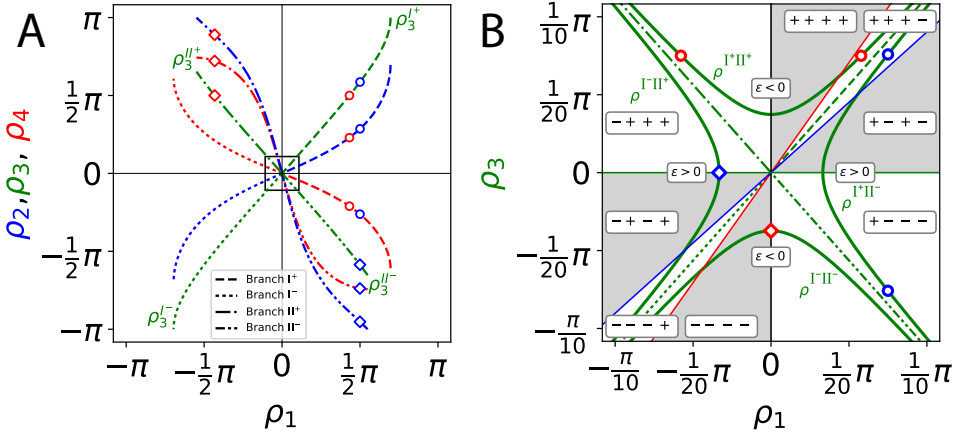


FIGURE 5.2: (A) Folding branches $\rho_i^{I+}(\rho_1)$, $\rho_i^{I-}(\rho_1)$, $\rho_i^{II+}(\rho_1)$, and $\rho_i^{II-}(\rho_1)$ for $i = 2, 3, 4$, for a flat vertex with sector angles as in Fig. 5.1.A. (B) Plot of ρ_3 as a function of ρ_1 for the small area around the origin shown in A. The dashed, and double dashed lines through the origin correspond to $\rho_3^{I+/-}(\rho_1)$ and $\rho_3^{II+/-}(\rho_1)$ as in A, for $\epsilon = 0$. The curved green lines indicate the merged folding branches ρ^{I-II+} and ρ^{I+II-} (for $\epsilon > 0$), and ρ^{I+II+} and ρ^{I-II-} (for $\epsilon < 0$). The solid black, blue, green, and red lines indicate where the folding angles ρ_1 , ρ_2 , ρ_3 , and ρ_4 change sign, and divide the plot in eight sectors, with the signs of their fold angles as indicated.

spring with rest angle ϕ placed on fold i results in stable states with $\rho_i = \phi$, of which there are always two, provided $\phi \neq 0$ and ϕ is not too large (not all ρ_i reach $\pm\pi$ along their folding branches). We show two specific examples. First, we consider a torsional spring with a positive rest angle $\rho_{\text{spring}} = \pi/2$ on the ρ_1 fold. As this single spring wants to relax to its rest angle, this results in two stable configurations: one on the I^+ branch, and one the II^- branch. The blue dots (for branch I^+) and blue diamonds (for branch II^-) at $\rho_1 = \rho_{\text{spring}}$ on these two branches indicate the ρ_i values for the two equilibrium configurations. Second, when we choose to put the same torsional spring on ρ_3 , we again find two stable states: one on the I^+ branch as before, and one on the II^+ branch. Here the red dots (for branch I^+) and red diamonds (for branch II^+) on these two branches indicate the two equilibrium configurations for which $\rho_3 = \rho_{\text{spring}}$. For convenience, we summarize the signs of the folding angles on the four different branches in table 5.1. From this, we deduce that a single spring on one of the two odd

	ρ_1	ρ_2	ρ_3	ρ_4
I^+	+	+	+	-
I^-	-	-	-	+
II^+	-	+	+	+
II^-	+	-	-	-

TABLE 5.1: Overview of the signs of the folding angles on the four $\epsilon = 0$ folding branches.

folds yields stable states at branch I^+II^- or I^-II^+ ; a single spring on one of the other folds yields stable states at branch I^+II^+ or I^-II^- .

This picture changes completely when we uniformly shrink or expand all the sector angles α_i by a factor f , such that the vertex is no longer euclidean. To describe these vertices we define the surplus angle, $\epsilon = f \sum \alpha_i - 2\pi$. Here $\epsilon < 0$, $f < 1$, corresponds to a vertex for which $\sum \alpha_i < 2\pi$, which results in a hat shaped vertex, as depicted in Fig. 5.1.B. Conversely, $\epsilon > 0$, $f > 1$, corresponds to a vertex for which $\sum \alpha_i > 2\pi$, which results in a saddle shaped vertex, as depicted in Fig. 5.1.C. For a flat vertex, where $\epsilon = 0$, the branching point of the two branches I and II is the flat state, where all $\rho_i = 0$. For a vertex where $\epsilon \neq 0$ this branching point disappears, resulting in disjoint folding branches.

We now explain what happens to the folding branches for $\epsilon \neq 0$, by focusing on the relation $\rho_3(\rho_1)$ in the area around the origin corresponding to the black square in Fig. 5.2.A, shown in large in Fig. 5.2.B¹. Here the four curves $\rho_3^{I^+}(\rho_1)$, $\rho_3^{I^-}(\rho_1)$, $\rho_3^{II^+}(\rho_1)$, and $\rho_3^{II^-}(\rho_1)$ for $\epsilon = 0$ are shown by the four green lines meeting at the origin. When we introduce a small angular offset, such that $\epsilon \neq 0$, we find that for $\epsilon < 0$ the two branches I^+ and II^+ merge together. This creates a new folding branch, which we shall indicate by I^+II^+ . In Fig. 5.2.B this corresponds to the $\rho_3^{I^+II^+}(\rho_1)$ curve. Similarly, we find that for $\epsilon < 0$ and $\rho_3 < 0$, the two branches $\rho_3^{I^-}(\rho_1)$ and $\rho_3^{II^-}(\rho_1)$ merge to form $\rho_3^{I^-II^-}(\rho_1)$. We note that for $\epsilon < 0$, the signs of the fold angles ρ_i vary as $(+++-) \mapsto (++++)$ or $(-+++)$ or $(- - - +) \mapsto (- - - -)$ or $(+ - - -)$. Hence, these vertices can form a ‘cone’ $(++++)$, or ‘bowl’ $(+ - - -)$ shape (see Table 5.2).

For the $\epsilon > 0$ case we find that the branches $\rho_3^{I^-}(\rho_1)$ and $\rho_3^{II^+}(\rho_1)$ merge to form $\rho_3^{I^-II^+}(\rho_1)$ when $\rho_1 < 0$. For $\epsilon > 0$ and $\rho_1 > 0$ we find that $\rho_3^{I^+}(\rho_1)$

¹We here explicitly calculated the branches, but this scenario is generic [74].

and $\rho_3^{II^-}(\rho_1)$ merge to form $\rho_3^{I^+II^-}(\rho_1)$. Along these branches, the signs of the fold angles vary as $(- - -+) \mapsto (- + -+) \mapsto (- + ++)$, or as $(+ + +-) \mapsto (+ - +-) \mapsto (+ - --)$. Hence, these vertices can form a ‘saddle’ $(+ - + -)$ or $(- + - +)$ shape (see Table 5.2). As illustrated in Fig. 5.2 there are still two possible folding branches for both $\epsilon > 0$ and $\epsilon < 0$. However, they are no longer connected by a common branching point.

		ρ_1	ρ_2	ρ_3	ρ_4
$\epsilon < 0$	I^+II^+	+	+	+	-
		+	+	+	+
		-	+	+	+
	I^-II^-	-	-	-	+
		-	-	-	-
		+	-	-	-
$\epsilon > 0$	I^-II^+	+	+	+	-
		+	-	+	-
		+	-	-	-
	I^+II^-	-	-	-	+
		-	+	-	+
		-	+	+	+

TABLE 5.2: Overview of the signs of the folding angles on the four folding branches for $\epsilon \neq 0$.

In this chapter we will harness the disconnectedness of the two folding branches for $\epsilon \neq 0$ to create tristable origami vertices. For example, the separation of the $\rho_3^{I^-II^-}$ and the $\rho_3^{I^+II^+}$ branches in the $\epsilon < 0$ case means that we can not change the sign of ρ_3 by rigid folding. However, real vertices have finite stiffness, and can be elastically deformed, by bending and stretching the plates and hinges. This enables us to ‘pop-through’ the vertex from branch $\rho_3^{I^+II^+}$ to $\rho_3^{I^-II^-}$ or vice versa. The angular surplus ϵ effectively creates an energy barrier between a cone with folding angles $- - -$, and a cone with folding angles $+ + +$. Similarly, the $\epsilon > 0$ case exhibits a saddle-to-saddle transition when popping the vertex through such that we force the vertex from the folding branch $\rho_3^{I^+II^-}$, with sign configuration $- + - +$, into folding branch $\rho_3^{I^-II^+}$ with sign configuration $+ - + -$.

We now show that a vertex with an angular offset $|\epsilon| > 0$, combined with a single torsional spring, allows us to make a tristable vertices. To demonstrate this, imagine attaching a single torsional spring with a rest angle of $\rho_{\text{spring}} = 3\pi/40$ on the ρ_1 fold of a $\epsilon > 0$ vertex. As we can see in Fig. 5.2.B, this results in two stable ($E = 0$) configurations on the $\rho_3^{I^+II^-}$ branch, one where $\rho_3 > 0$, and one where $\rho_3 < 0$, indicated by the blue dots. When we pop this vertex through to the folding branch $\rho_3^{I^-II^+}$, one additional *local* minimum can be found on the $\rho_3^{I^-II^+}$ branch, indicated by the blue diamond. Here $E \neq 0$, as the spring cannot reach its relaxed state, as the torsional spring wants to minimize its energy, the energy minimum is located as close to $\rho_1 = \rho_{\text{spring}}$ as possible. This minimum, which is not present when $\epsilon = 0$, is stable provided that the energy necessary to ‘pop-through’ the vertex from the I^-II^+ branch to the I^+II^- is sufficiently high compared to the energy stored in the spring. Conversely, we can make a tristable $\epsilon < 0$ vertex by putting a $\rho_{\text{spring}} = 3\pi/40$ on the ρ_3 fold. In Fig. 5.2.B we see this results in two stable states on the $\rho_3^{I^+II^+}$ folding branch, as indicated by the two red dots. A third, local minimum can be found on the $\rho_3^{I^-II^-}$ folding branch when we pop the vertex through from the I^+II^+ branch to the I^-II^- branch, as is indicated by the red diamond.

Inspecting the signs of the fold angles on the $\epsilon \neq 0$ branches as summarized in table 5.2, as well as the generic sketch of these branches in Fig. 5.2, we conclude that $\epsilon < 0$ vertices can be made tristable by putting a single spring on ρ_2 or ρ_3 , i.e. a fold opposite to the odd folds (ρ_4, ρ_1) of the corresponding flat vertex. On the contrary, $\epsilon > 0$ vertices can be made tristable by putting a single spring on one of the two odd folds of the corresponding flat vertex.

5.2.2 Theoretical Energy Curves

In this section we compute the elastic energy as a function of fold angle, for non-Euclidean 4-vertices, augmented with a single torsional spring. We focus on the scenarios outlined in the previous section that potentially lead to tristable vertices. We consider vertices with sector angles $\alpha_i = (1 + \frac{\epsilon}{2\pi})\{\pi/3, \pi/2, 3\pi/4, 5\pi/12\}$, and angular surplus of $\epsilon = \sum \alpha_i - 2\pi = \pm\{0.001, 0.01, 0.03, 0.001\}$ rad.

For the cone-like, $\epsilon < 0$ vertices we choose to put the spring on the ρ_4 fold of the vertices. As discussed in the previous section this leads to two stable states on the I^+II^+ branch, and one stable state on the I^-II^-

branch. Assuming a torsional spring with a stiffness k_{spring} , and a rest angle $\rho_{\text{spring}} > 0$, the energy curves can then be calculated as,

$$E_{\text{bistable}}^{\epsilon < 0}(\rho_1, \epsilon) = \frac{1}{2} \cdot k_{\text{spring}} \left(\rho_3^{I^+ II^+}(\rho_1, \epsilon) - \rho_{\text{spring}} \right)^2 \quad (5.3)$$

for the bistable branch, and

$$E_{\text{monostable}}^{\epsilon < 0}(\rho_1, \epsilon) = \frac{1}{2} \cdot k_{\text{spring}} \left(\rho_3^{I^- II^-}(\rho_1, \epsilon) - \rho_{\text{spring}} \right)^2 \quad (5.4)$$

for the monostable branch. The corresponding energy curves as a function ρ_1 are displayed in Fig. 5.3.A.

For the saddle-like, $\epsilon > 0$ vertices we choose to put a torsional spring on the ρ_2 fold of the vertices, which leads to one bistable branch ($I^+ II^-$), and one monostable branch ($I^- II^+$), when viewed as a function of ρ_3 (see Fig. 5.2.B). The energy curves can then be calculated as,

$$E_{\text{bistable}}^{\epsilon > 0}(\rho_3, \epsilon) = \frac{1}{2} \cdot k_{\text{spring}} \left(\rho_1^{I^+ II^-}(\rho_3, \epsilon) - \rho_{\text{spring}} \right)^2 \quad (5.5)$$

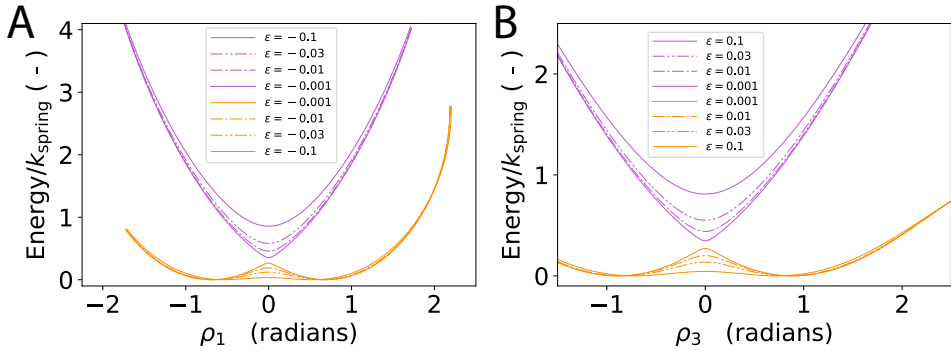


FIGURE 5.3: (A) Bistable energy curve on branch $I^+ II^+$ (pink), and monostable energy curve on branch $I^- II^-$ (orange), for a cone-like, $\epsilon < 0$ vertex with a spring on ρ_4 , and controlling ρ_2 , for various values of ϵ (see legend). (B) Bistable energy curve (pink) on branch $I^+ II^-$, and monostable energy curve on branch $I^- II^+$ (orange), for a saddle-like, $\epsilon > 0$ vertex with a spring on ρ_2 , and controlling ρ_4 , for various values of ϵ (see legend).

and,

$$E_{\text{monostable}}^{\epsilon > 0}(\rho_3, \epsilon) = \frac{1}{2} \cdot k_{\text{spring}} \left(\rho_1^{I-II+}(\rho_3, \epsilon) - \rho_{\text{spring}} \right)^2 \quad (5.6)$$

respectively. These energy curves are plotted in Fig. 5.3.B as function of ρ_3 .

In both the $\epsilon < 0$, and the $\epsilon > 0$ case we clearly have three minima. We note that the separation of the energies at $\rho_3 = 0$ between the upper and lower branches grows as $\sqrt{\epsilon}$, which is expected for the unfolding of a transcritical scenario (the intersection of the I and II branches at $\epsilon = 0$). In addition, we notice that the depth of the two minima on the lower branch diminishes with ϵ . The experimental challenge is therefore to find a value of ϵ for which the upper and lower branch are sufficiently separated by means of the ‘pop-through’ barrier, but which does not wash out the two minima on the lower branch.

5.3 3D Printed Tristable Vertices

Here we describe the manufacturing of non-flat 4-vertices. Specifically, we aim to create vertices where the two branches have one, respectively two energy minima at corresponding stable states, and where the energy barrier between these branches is in the right range to allow “popping” from one branch to the other, without destroying the three energy minima on the two branches. We discuss how we make these vertices by use of 3D printing, and how we turn them into tristable vertices by dressing them with a torsional spring.

We first discuss the experimental fabrication of non-flat 4-vertices. The

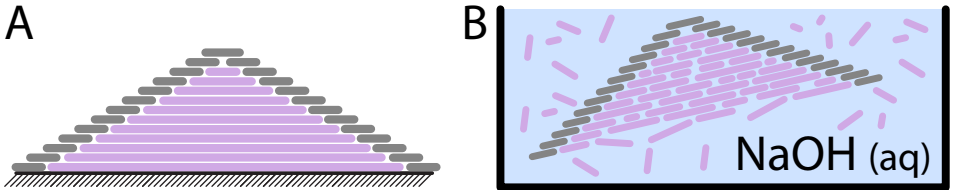


FIGURE 5.4: (A) Schematic side view of the 3D printing process, using two different materials. Vertices are built up layer by layer (in gray), and arbitrary geometries can be created by use of a scaffold material (in lilac). (B) We dissolve the scaffold in an 70° C aqueous NaOH solution, which leaves the plate material intact.

5.3. 3D PRINTED TRISTABLE VERTICES

vertices we use for our experiment are 3D printed with a Stratasys Fortus 250 MC, which is capable of printing ABS plastic, as well as a sacrificial ABS-like plastic, with a layer thickness of 0.18 mm and an xy-resolution of better than 0.24 mm. The sacrificial material serves as a scaffold, and allows us to print non-flat vertices, see Fig. 5.4.A. This scaffold is subsequently dissolved by putting the structure in a 70° C sodium hydroxide (NaOH, pH 9.0) solution for 7 hours, see Fig. 5.4.B. This printing technique therefore allows us to print non-flat vertices with an arbitrary angular surplus ϵ .

We design our vertices to be 150 mm in diameter, consisting of four plates which are 3.0 mm thick, see Fig. 5.5.A. The four plates of the vertex

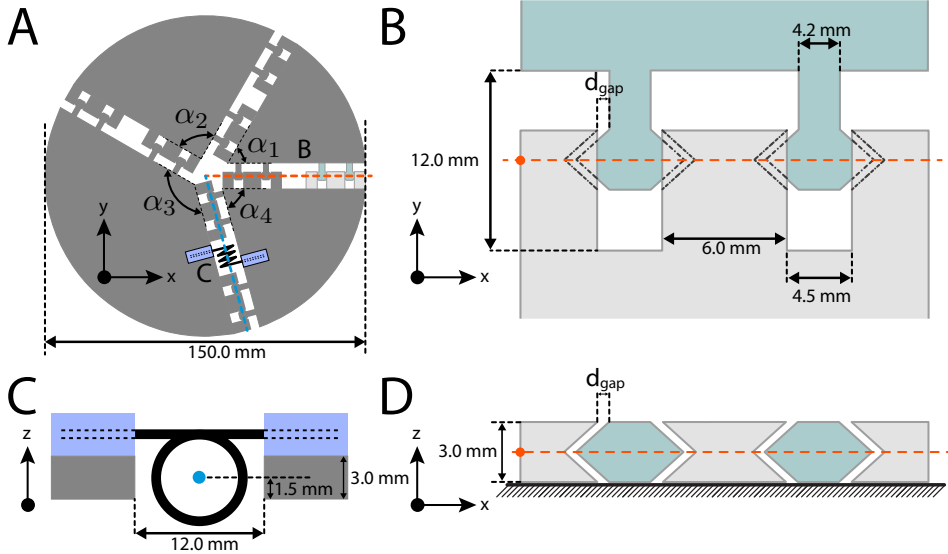


FIGURE 5.5: (A) Top view of the design of a 3D printed, (flat) 4-vertex with sector angles $\alpha_i = \{\pi/3, \pi/2, 3\pi/4, 5\pi/12\}$. This vertex is 150 mm in diameter and 3 mm thick. The plates are connected by four conically shaped hinges (detailed view in B,D). A torsional spring can be put on one of the folds (see C for a detailed side view). (B) Detailed top view of the hinges in A, where the dotted orange line indicates the axis of rotation of the conical hinges. (C) Side view of the torsional spring in A. The spring is offset from the plates of the vertex such that its axis of rotation aligns with the axis of rotation of the hinges (see blue line in B). (D) Side view cut through of the hinges in A,B. The dotted orange line indicates the axis of rotation of the conical hinges as in A,B.

are connected to each other by four hinges, and the axes of rotation of all these hinges meet at the center of the vertex. The hinges consist of two disconnected conical holes attached to one plate, and two opposing conical pins attached to the opposing plates (Fig. 5.5.B). This design allows us to closely emulate a perfect hinging fold. The main experimental limitation is the finite maximal folding angle, of approximately $|\rho_i| \approx 2.65$ rad, due to the formation of self contacts between the plates that occur for high folding angles. A detailed view of the design is shown in Fig. 5.5.B and Fig. 5.5.D. This hinge design allows us to print the vertex in its assembled state, including the hinges. However, it does require careful tuning of the d_{gap} parameter that sets the separation between the conical holes and the conical pins (Fig. 5.5.B,D). When we set d_{gap} too low, the hinges get stuck to each other after the printing process, which was found to be the case for $d_{\text{gap}} = 0.05$ mm and $d_{\text{gap}} = 0.1$ mm. Setting d_{gap} too high results in a vertex with excessive play in the hinges, which leads to significant deviations from rigid folding. The gap d_{gap} was therefore chosen to be $d_{\text{gap}} = 0.15$ mm, which is roughly equal to the layer resolution of the 3D printer (at 0.18 mm).

The vertex is designed to allow to incorporate a torsional spring on one of the folds, as is shown in Fig. 5.5.A. We do this by including cylindrical holes of diameter 1.14 mm in the design of the 3D-printed vertex, which allows us to attach an Amatec T045-270-312 torsional spring. These holes are offset from the plate material such that the center of rotation aligns with that of the center of the hinges, see Fig. 5.5.C. In order to create a tristable vertex by adding a single torsional spring, we choose to print cone-like vertices such that we can attach the spring to the ρ_1 fold, and the saddle-like vertices such that we can attach the spring to the ρ_3 fold (see section 5.2). Furthermore we note that the torsional springs are not irreversibly attached to the vertices, and can be taken out to perform control experiments.

For the sector angles of the vertices we choose $\alpha_i = (1 + \frac{\epsilon}{2\pi})\{\pi/3, \pi/2, 3\pi/4, 5\pi/12\}$. Our goal is to fabricate vertices which we can reversibly pop-through. This puts an upper limit on $|\epsilon|$, as the maximal stresses on the hinges during the pop-through grows with increasing $|\epsilon|$. In practice, we found that vertices for which $|\epsilon| > 0.105$ rad readily fail at the hinges after popping it through ten or less times. Conversely, vertices for which $|\epsilon| < 0.026$ rad barely show any pop-through behavior at all, presumably due to the small but finite play in the hinges. This makes such vertices

unsuitable to our end goal of making tristable vertices, which requires an energy barrier between the two branches. We therefore focus on vertices with an angular surplus of $|\epsilon| = 0.052$ rad. These vertices do not break at the hinges after popping them through numerous times, yet the pop-through energy barrier of these vertices is large enough for the two folding branches to remain separated, as we will show.

5.4 Experimental Results

In this section we will first demonstrate that the 3D printed vertices of section 5.3 can be made tristable by adding a single torsional spring to one of the folds (section 5.4.1). After this, we characterize the tristable energy landscape by use of an Instron MT-1 torsion tester. We first explain the experimental protocol (section 5.4.2), then we show our experimental results (section 5.4.3), and last we convert our torsion data into experimental energy curves, in order to compare them to theoretical predictions (section 5.4.4). Finally, we show that we can control the separation between the bistable and monostable folding branches of the vertices by carefully tuning the angular surplus ϵ (section 5.4.5).

5.4.1 Tristable Vertex: Qualitative Results

In the previous section we showed that we settled on a vertex with an angular surplus of $\epsilon = \pm 0.052$ rad, which allowed for reversible pop-through behavior. To turn the 3D printed vertices into a tristable vertex, we now attach an Amatec T045-270-312 torsional spring, with a torsional stiffness of 46(1) mNm/rad, and rest angle $\rho_{\text{spring}} \approx 0.69(2)$. We will show that the combination of spring and vertex geometry ensures that the energy needed to pop-through the vertex, E_{pop} , is sufficiently high in comparison to the barriers of the mono- and bi-stable branches, E_{min} and E_{barrier} respectively. We can qualitatively verify that $E_{\text{min}} < E_{\text{pop}}$ by taking one of the experimentally realized vertices including the torsional spring, popping it through manually, and leaving it untouched. This is shown in Fig. 5.6.A and Fig. 5.6.D for the $\epsilon = -\pi/60 \approx -0.052$ rad and the $\epsilon = \pi/60 \approx 0.052$ rad vertex respectively. Furthermore, we can show that $E_{\text{barrier}} < E_{\text{pop}}$ by showing that the two minima on the bistable branch are stable; this is shown in Fig. 5.6.B,C and Fig. 5.6.E,F. This shows that the combination of angular surplus and torsional spring chosen here leads to a

tristable vertex, both for $\epsilon < 0$ and $\epsilon > 0$.

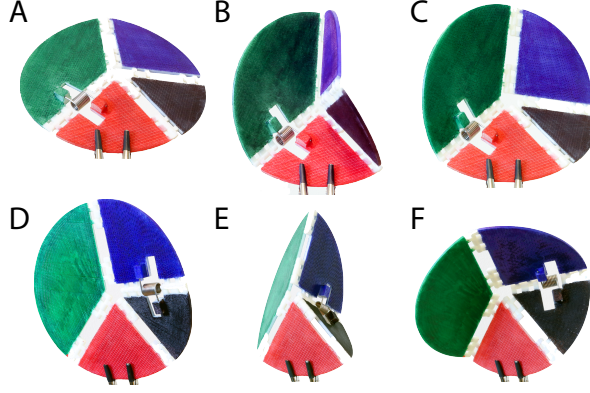


FIGURE 5.6: (A,B,C) The three stable states we found for an $\epsilon = -\pi/60$ vertex. Here (A) represents a state corresponding to a local energy minimum; (B) and (C) represent states corresponding to global energy minima, where $\rho_1 < 0$ and $\rho_1 > 0$ respectively. (D,E,F) The three stable states we found for an $\epsilon = \pi/60$ vertex. Here (D) represents a state corresponding to a local energy minimum; (E) and (F) represent states corresponding to global energy minima, where $\rho_3 < 0$ and $\rho_3 > 0$ respectively.

5.4.2 Experimental Protocol for Torsion Experiments

To quantify the multistability of these experimentally realized, non-flat 4-vertices, we aim to obtain the elastic energy as a function of one of the fold angles, on both branches, as well as the energy of the pop-through. While in principle these can be measured straight forwardly by measuring the torque as function of fold angle, in practice there are several experimental complications, due to the effect of gravity, and friction, that require special care. To measure the torque as function of fold angle, we clamp two plates of the vertex in an Instron MT-1 torsion tester with a 2.25 N·m load cell, which allows us to measure torques with an accuracy of 0.01 N·m, and angular displacement with a resolution of $5 \cdot 10^{-5}$ rad; a picture of this setup is shown in Fig. 5.7.A. In Fig. 5.7.B we depict a schematic side-view of the setup used to measure the torque as a function of the folding angle. On the left side we see the drive side of the torsion tester, which can rotate the red plate plate by means of a center-offset clamp. On the right side we see the load cell, which is stationary. In order for the load cell to measure

the torque exerted on the green plate, we made a custom U-shaped clamp, which has enough clearance for the vertex to fold, and can attach on the other side of the vertex (see Fig. 5.7.B).

Protocol: (i) The first step in measuring the energy landscape of the vertex is to characterize the torsional spring by probing its spring constant k_{spring} , and rest angle ρ_{spring} . We do this by attaching the spring to the vertex and by manipulating the fold on which the spring is attached, which is fold ρ_3 for the $\epsilon < 0$ vertices, and fold ρ_1 for the $\epsilon > 0$ vertices (see section 5.3). (ii) Second, we attach the vertex differently, so as to measure the torque required to change the fold angle opposite to the spring, which is fold ρ_1 for the cone-like vertices, and fold ρ_3 for the saddle-like vertices. Here, we make sure that the vertex is on the bistable branch. (iii) Third, while the vertex is still attached to the clamps of the torsion tester, we manually force the vertex to pop-through the fold where the spring is attached, which moves the vertex to the monostable folding branch. For the cone-like vertices this means changing the sign of the ρ_3 fold from positive to negative; for the saddle-like vertices this means changing the sign of ρ_1 from positive to negative. To probe the energy landscape on the monostable branch we then measure the torque required to change fold ρ_1 for the cone-like vertices, and fold ρ_3 for the saddle-like vertices. The three torque measurements (i)-(iii) can be converted to energy landscapes by integration, and in principle yield the energy curves that can be compared to the theoretical prediction (see Fig. 5.3). However, friction and gravity also play a role, and require careful attention.

First, the hinges of the vertices are not frictionless, even though they are thoroughly sprayed with silicone oil. The resulting frictional forces show up in our measurements as an offset to the signal that we want to measure. Our approach is to “average out” the friction signal, as frictional forces are always oriented opposite to the direction of movement, and are roughly rate-independent. We therefore perform cyclic experiments, where we first increase the fold angle ρ_i to its maximum value, and then decrease ρ_i to its minimum value. For every measurement we then average the signal of the upward and downward ρ_i to suppress frictional forces. Second, even without any springs attached to the vertices, there is a non-constant torque signal due to gravitational forces. This is explained schematically in Fig. 5.7.C, and 5.7.D. As the drive shaft rotates the red plate, three of the plates change position relative to the gravitational field, which leads to a

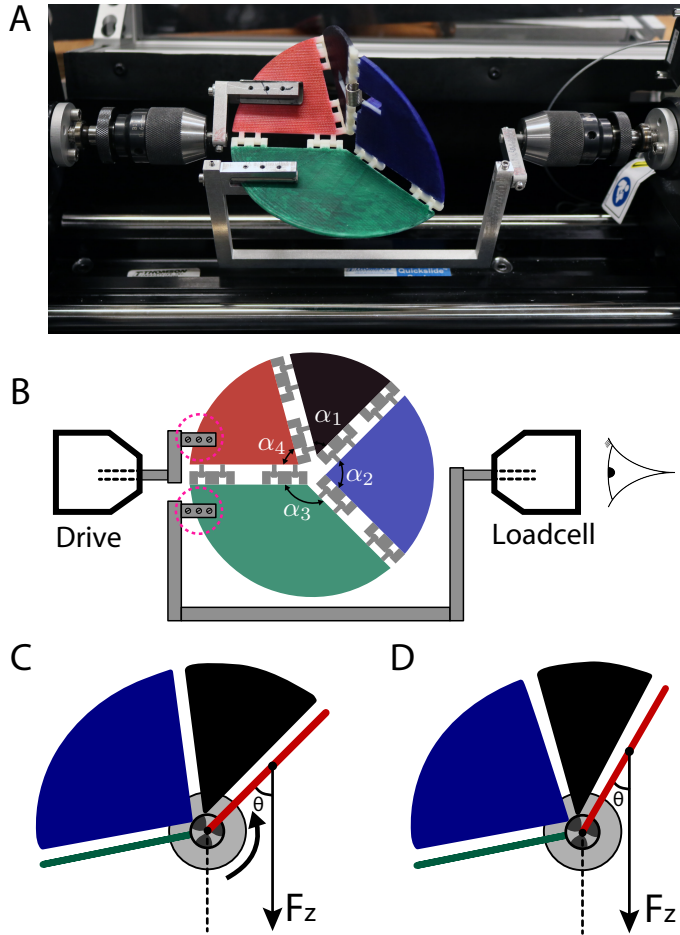


FIGURE 5.7: (A) Picture of the vertex shown in Fig. 5.6.D-F, clamped in the Instron MT-1 torsion tester. See (B) for a schematic of the setup. (B) Side view schematic of how the Instron torsion tester is connected to the 4-vertex. One plate (here plate α_4) is attached to the drive side of the tester (on the left) by means of a center-offset clamp. Another clamp is attached to the load cell side of the tester (on the right), by means of a U-shaped clamp. Note that when actuated, plates 1, 2, and 4 move, while plate 3 is kept stationary. (C,D) Cut-through schematic when looking from the side of the load cell, in the direction of the drive shaft, as indicated in panel A. The three moving plates change position in the gravitational field, which results in a non-zero torque signal, even without any spring attached to the vertex.

corresponding torque, T_{gravity} . In order to suppress this signal, we do two separate experiments: one with the torsional spring attached to the vertex, and one where we take the spring off. By subtracting these two signals, we effectively suppress the T_{gravity} signal.

By averaging the signal obtained from cyclic experiments, as well as pairing every measurement *with* spring to an identical control experiment *without* spring, we suppress both the effect of friction, as well as the effect of gravity. We therefore have to do six experiments for every vertex. Here, in summary, we list this series of experiments. First, for the cone-like vertices we perform the following six experiments:

1. manipulating ρ_3 with and without spring attached, to obtain the spring constant, k_{spring} ;
2. manipulating ρ_1 , on the bistable branch ($\rho_3 > 0$), with and without spring attached, to probe the energy landscape of the bistable branch;
3. manipulating ρ_1 , on the monostable branch ($\rho_3 < 0$), with and without spring attached, to probe the energy landscape of the monostable branch.

Likewise, for the saddle-like vertices we perform the following six experiments:

1. manipulating ρ_1 with and without spring attached, to obtain the spring constant, k_{spring} ;
2. manipulating ρ_3 , on the bistable branch ($\rho_1 > 0$), with and without spring attached, to probe the energy landscape of the bistable branch;
3. manipulating ρ_3 , on the monostable branch ($\rho_1 < 0$), with and without spring attached, to probe the energy landscape of the monostable branch.

For each of these experiments we open and close the fold that we manipulate four times, using up and down sweeps of the angle with a ramp rate of 0.070 rad/s. The maximum opening and closing angle of the fold that is manipulated is determined when the first fold reaches its maximum angle of $\rho_i \approx 2.65$ rad, at which self-contact of the hinges limits the range of movement (see previous chapter), add the aluminium clamps that are holding the plates (indicated by the two dashed circles in Fig. 5.7.B), which can contact each other.

5.4.3 Torsion Experiments - Results

We now explain in detail how we deal with gravitational and frictional forces for the measurements where we probe the torsional spring on the $\epsilon = -\pi/60$ vertex. After correcting for these spurious signals, we find that the torque exerted by the spring as function of fold angle is close to linear, which gives confidences in our methodology. We then apply the same protocol to the remaining experiments that probe the torsional spring on the $\epsilon = \pi/60$ vertex in section 5.4.3, as well as the non trivial energy landscape at each branch, in sections 5.4.3 and 5.4.3.

We now first explain in detail how we determine the spring properties by actuating the fold where the spring is attached, and how we deal with gravitational and frictional forces. We both probe the torsional spring on the $\epsilon = -\pi/60$ vertex and on the $\epsilon = \pi/60$ vertex.

Torsional Spring on a Cone-like Vertex

As explained in the above section, to determine the spring properties, we clamp the $\epsilon = -\pi/60$ vertex such that the torque is directly applied to the two plates adjacent to the spring (ρ_3 fold), and compare data with and without a spring attached. As shown in Fig. 5.8A, even without a spring attached, the raw torque signal $T_0(\rho_3)$ is complex and exhibits hysteresis. This hysteresis is due to friction, and we obtain a signal \bar{T}_0 by averaging over up and down sweeps (Fig. 5.8B):

$$\bar{T}_0(\rho_3) = \frac{1}{2}(T_0(\rho_3 \uparrow) + T_0(\rho_3 \downarrow)) . \quad (5.7)$$

As shown in Fig. 5.8C-D, we follow the same procedure for a vertex where the spring is attached, and define \bar{T} as

$$\bar{T}(\rho_3) = \frac{1}{2}(T(\rho_3 \uparrow) + T(\rho_3 \downarrow)) . \quad (5.8)$$

After eliminating friction, the two signals \bar{T}_0 and \bar{T} have contributions from gravity (T_g), non-rigid deformations of the vertex (T_{VD}), and in the case of \bar{T} , from the spring T_{spring} . The gravitational signal is expected to be very similar in \bar{T}_0 and \bar{T} , and by subtracting these signals we obtain a signal that is the sum of T_{spring} and T_{VD} (Fig. 5.9). The non-rigid deformations are due to the vertex “popping” between two branches and are the cause of the

5.4. EXPERIMENTAL RESULTS

large torque spikes near $\rho_3 = 0$. The interval of the folding angles where these deformations can be expected with bounds $\pm\rho_{3,\min}$ is dependent on the surplus parameter ϵ , as can be seen from Fig. 5.2.C. For the $\epsilon = -\pi/60$ vertex we find $\rho_{3,\min} = \pm 0.27$ using our analytical model. Hence, for larger fold angles, the only signal is due to the spring, and indeed we observe that for $|\rho_3| > \rho_{3,\min}$, the signal is essentially linear. The excellent fit to a linear function (black) indicates that the spring follows the torsional variant of Hooke's law, and can be used to extract the torsional spring constant $k_{\text{spring}} = 46(1) \text{ mNm/rad}$, as well as the rest angle: $\rho_{\text{spring}} = 0.73(1) \text{ rad}$. We conclude that, even though the raw torque signal shows large amounts of hysteresis, a significant contribution due to gravity, and near $\rho_3 = 0$ a strong signal due to vertex deformation, we can deal with these effects to characterize the torsional spring.

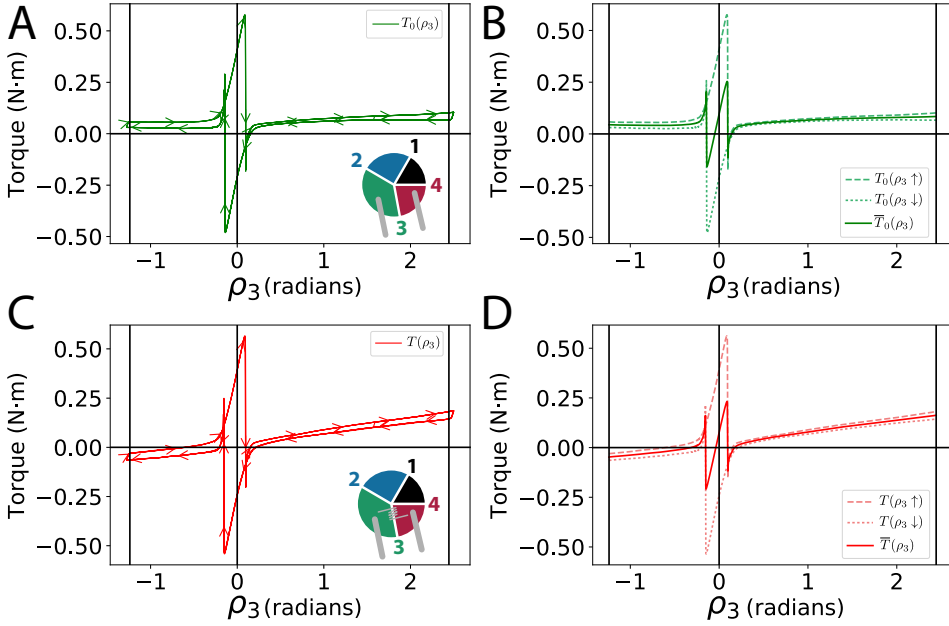


FIGURE 5.8: (A) Raw data T_0 for a measurement on a $< 2\pi$ vertex without spring attached (see inset). (B) Mean signal \bar{T}_0 eliminates friction but has contributions from gravity and vertex deformations. (C) Raw data T for a measurement on a $< 2\pi$ vertex with spring attached (see inset). (D) Mean signal \bar{T} eliminates friction but has contributions from gravity, vertex deformations and the spring.

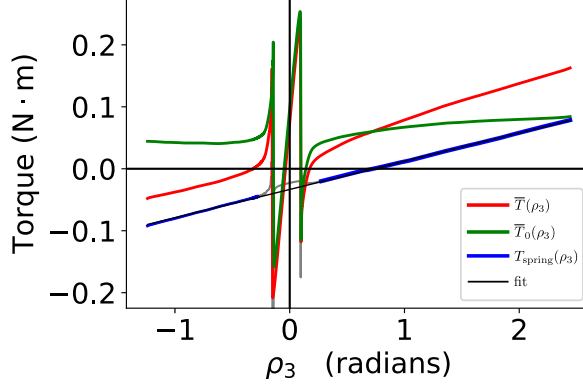


FIGURE 5.9: The difference between \bar{T} and \bar{T}_0 is the sum of the vertex deformations, confined near $|\rho_3| < 0.27$, and a nearly linear function, due to the spring (blue). The black line indicates a linear fit.

Torsional Spring on a Saddle-like Vertex

The same experiments were performed for the $\epsilon = \pi/60$, saddle-like vertex. Here we place the spring—which is the same spring as used before—on the ρ_1 fold. The measurements *without* spring is shown in Fig. 5.10.A, and the averaged signal $\bar{T}_0(\rho_1) = \frac{1}{2}(T_0(\rho_1 \uparrow) + T_0(\rho_1 \downarrow))$ is shown in Fig. 5.10.B. The average signal of the measurement *with* spring, $\bar{T}(\rho_1) = \frac{1}{2}(T(\rho_1 \uparrow) + T(\rho_1 \downarrow))$ is shown in Fig. 5.10.D. The two signals are then subtracted, to obtain $T_{\text{spring}} = \bar{T} - \bar{T}_0$, for $|\rho_1| > \rho_{1,\min}$, which is shown in Fig. 5.11. Here $\rho_{1,\min} = \pm 0.25$ rad indicates the boundary within which the signal due to vertex deformations, T_{VD} , can not be neglected (see previous section).

The black line in Fig. 5.11 indicates a linear fit of the form $T_{\text{spring}} = k_{\text{spring}} \cdot (\rho_1 - \rho_{\text{spring}})$. This produces a torsional spring constant of $k_{\text{spring}} = 47(1)$ mNm/rad, which is within errorbars of the of $k_{\text{spring}} = 46(1)$ mNm/rad obtained in the previous section, as this the same identical spring. However, the rest angle seems to have changed slightly: $\rho_{\text{spring}} = 0.65(1)$ rad compared to $\rho_{\text{spring}} = 0.73(1)$ rad as extracted from the fit in Fig. 5.9. This difference in rest angle might be attributed to a slightly different way the torsional spring is glued to the vertex, resulting in a different *effective* rest angle.

5.4. EXPERIMENTAL RESULTS

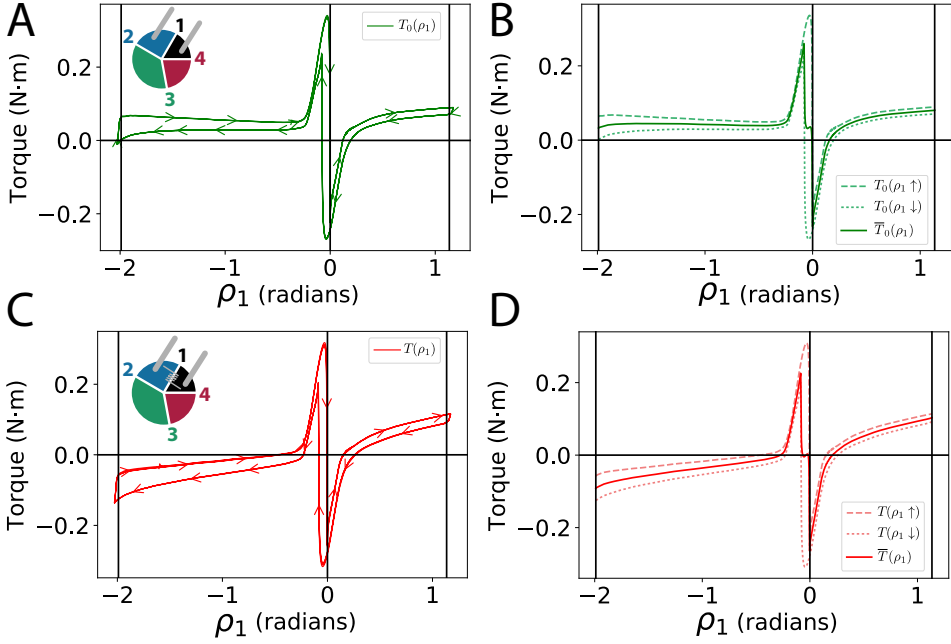


FIGURE 5.10: (A) Raw data T_0 for measurement on $> 2\pi$ vertex without spring attached (see inset). (B) Mean signal T_0 eliminates friction but has contributions from gravity and vertex deformations. (C) Raw data T for a measurement on $> 2\pi$ vertex with spring attached (see inset). (D) Mean signal \bar{T} eliminates friction but has contributions from gravity, vertex deformations and the torsional spring.

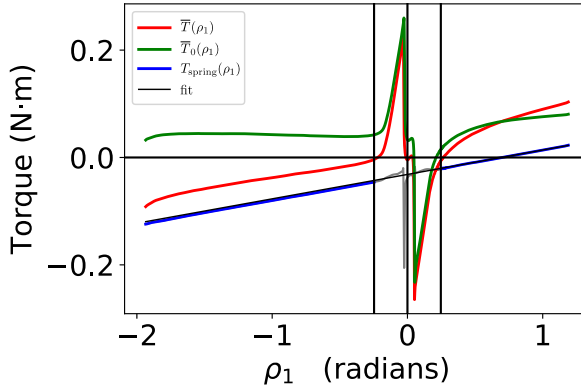


FIGURE 5.11: The difference between \bar{T} and \bar{T}_0 is the sum of the vertex deformations, confined near $|\rho_1| < 0.25$, and a nearly linear function, due to the spring (blue). The black line indicates a linear fit.

Monostable and Bistable Branch for a Cone-like Vertex

In order to probe the bi- and monostable branch of the $\epsilon < 0$ vertex we manipulate the ρ_1 fold, with the spring on the ρ_3 fold. The sign of the ρ_3 fold then determines whether we are dealing with the bistable branch ($\rho_3 > 0$), or the monostable branch ($\rho_3 < 0$), see Fig. 5.2.C.

To extract the torque signal associated with the monostable branch, where we first need to pop the vertex through by hand such that $\rho_3 < 0$. After having done this, we clamp the vertex in the torsion tester such that we can manipulate the ρ_1 fold. The raw data of the measurement without spring, $T_0(\rho_1)$, is shown in Fig. 5.12.A, and the averaged signal, $\bar{T}_0(\rho_1) = \frac{1}{2}(T_0(\rho_1 \uparrow) + T_0(\rho_1 \downarrow))$, in Fig. 5.12.B. The raw data of the measurement *with* spring is displayed in Fig. 5.12.C, whereas the averaged signal $\bar{T}(\rho_1) = \frac{1}{2}(\bar{T}(\rho_1 \uparrow) + \bar{T}(\rho_1 \downarrow))$ is displayed in Fig. 5.12.D. Finally, we subtract the two signals to yield $T_{\text{mono}}^{\epsilon < 0}(\rho_1) = \bar{T}(\rho_1) - \bar{T}_0(\rho_1)$, which is displayed in Fig. 5.13.

The same procedure is repeated for the bistable branch –where $\rho_3 > 0$ – we once again need two experiments. First, we measure *without* the spring attached, and manipulate the ρ_1 fold. The result of this measurement is shown in Fig. 5.14.A. The up and down sweeps are then averaged to suppress friction: $\bar{T}_0(\rho_1) = \frac{1}{2}(T_0(\rho_1 \uparrow) + T_0(\rho_1 \downarrow))$, see Fig. 5.14.B. Second, we measure *with* the spring on ρ_3 , where the averaged torque signal $\bar{T}(\rho_1) = \frac{1}{2}(T(\rho_1 \uparrow) + T(\rho_1 \downarrow))$ is displayed in Fig. 5.14.D. Finally, we subtract the two averaged signals to find $T_{\text{bi}}^{\epsilon < 0}(\rho_1) = \bar{T}(\rho_1) - \bar{T}_0(\rho_1)$, which is displayed in Fig. 5.15 as the orange curve.

5.4. EXPERIMENTAL RESULTS

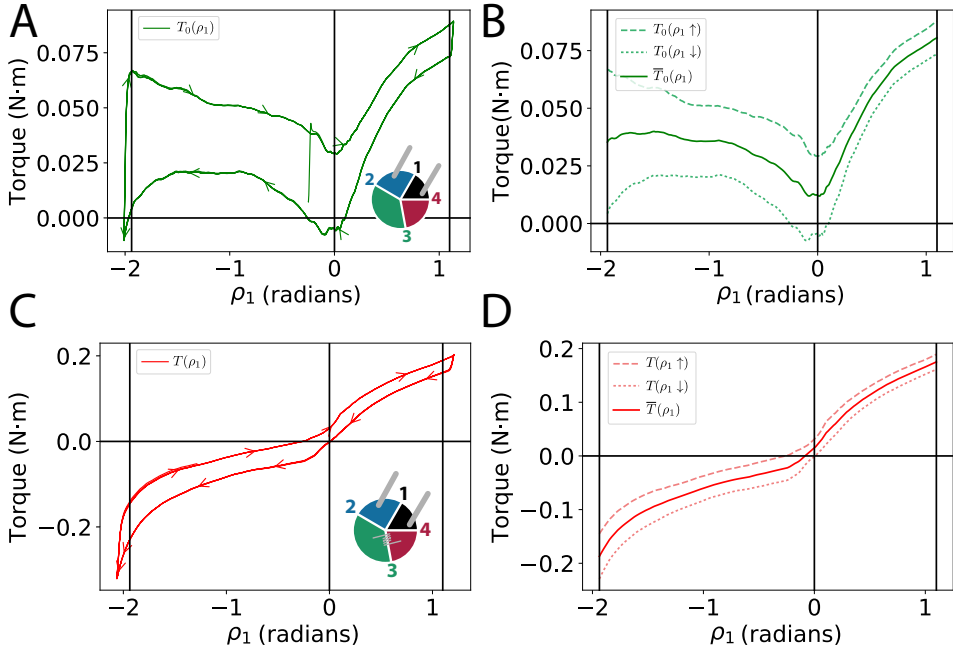


FIGURE 5.12: (A) Raw data T_0 of the the monostable branch of a $< 2\pi$ vertex, without spring attached (see inset). (B) Mean signal \bar{T}_0 eliminates friction but has contributions from gravity. (C) Raw data T of the monostable branch of a $< 2\pi$ vertex, *with* spring attached (see inset). (D) Mean signal \bar{T}_0 eliminates friction but has contributions from gravity as well as the spring.

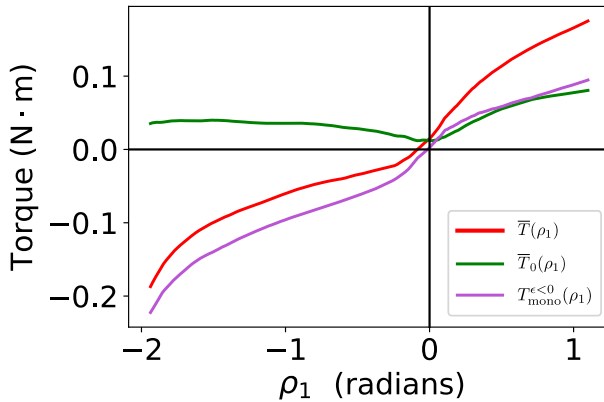


FIGURE 5.13: The difference between \bar{T} (red) and \bar{T}_0 (green), results in the torsion signal for the monostable branch: $T_{\text{mono}}^{\epsilon < 0}$ (purple).

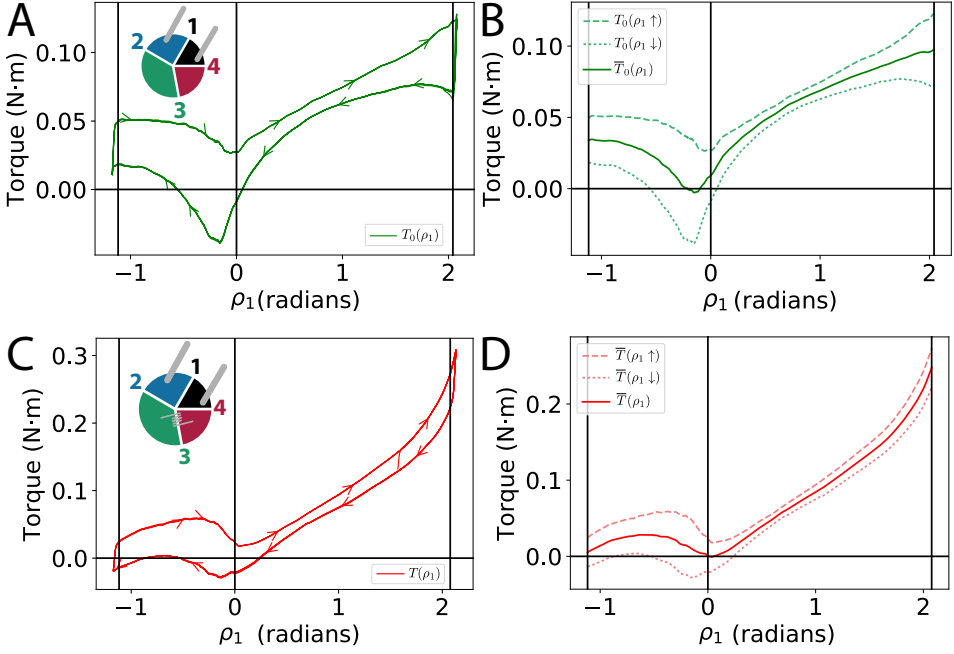


FIGURE 5.14: (A) Raw data T_0 of the the bistable branch of a $< 2\pi$ vertex, without spring attached (see inset). (B) Mean signal \bar{T}_0 eliminates friction but has contributions from gravity. (C) Raw data T of the bistable branch of a $< 2\pi$ vertex, *with* spring attached (see inset). (D) Mean signal \bar{T}_0 eliminates friction but has contributions from gravity as well as the spring.

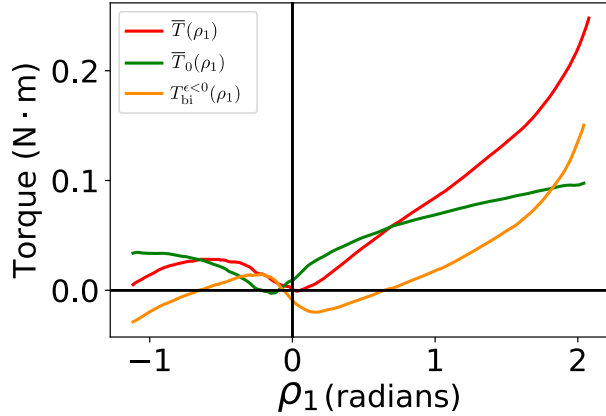


FIGURE 5.15: The difference between \bar{T} (red) and \bar{T}_0 (green), results in the torsion signal for the bistable branch: $T_{bi}^{\epsilon < 0}$ (orange).

Monostable and Bistable Branch for a Saddle-like Vertex

The torque measurements for the bi- and monostable branches for the $\epsilon = \pi/60$ vertex are shown in Fig. 5.18 and Fig. 5.16 respectively. The difference with respect to the cone-like, $\epsilon = \pi/60$ vertices is that the torsional spring is now put on the ρ_1 fold, whereas the plates connected by the ρ_3 fold are clamped. The torque measurements of the monostable branch, where the vertex is ‘popped through’ such that $\rho_1 < 0$, is summarized in Fig. 5.17, where we show $T_{\text{mono}}^{\epsilon>0}(\rho_3) = \bar{T}(\rho_3) - \bar{T}_0(\rho_3)$ in purple. The torque data of the bistable branch –where $\rho_1 > 0$ – is summarized by Fig. 5.19, where the gravity corrected signal $T_{\text{bi}}^{\epsilon>0}(\rho_3) = \bar{T}(\rho_3) - \bar{T}_0(\rho_3)$ is shown by the orange line.

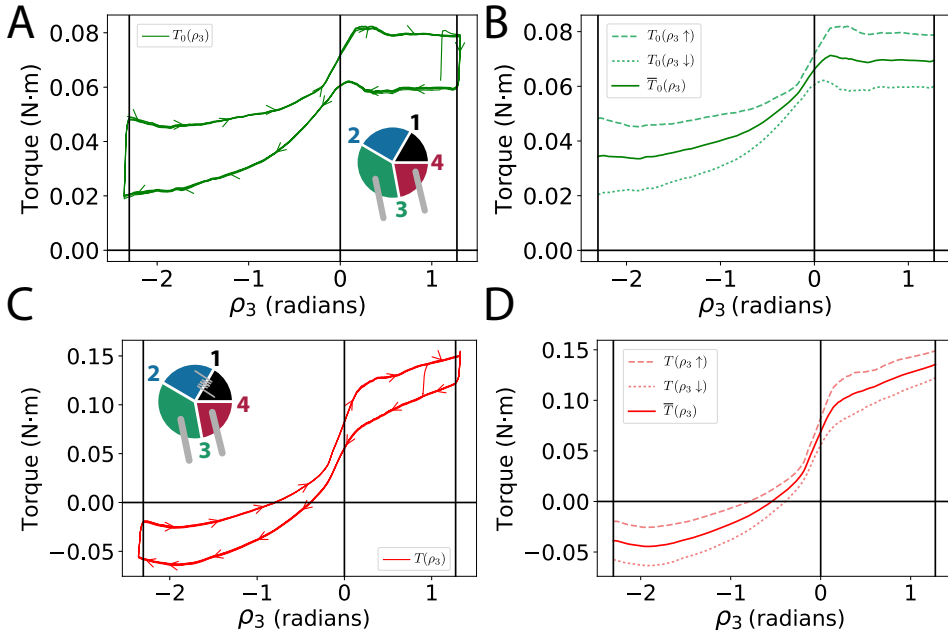


FIGURE 5.16: (A) Raw data T_0 of the monostable branch of an $\epsilon > 0$ vertex, without spring attached (see inset). (B) Mean signal \bar{T}_0 eliminates friction but has contributions from gravity. (C) Raw data T of the monostable branch of an $\epsilon > 0$ vertex, *with* spring attached (see inset). (D) Mean signal \bar{T} eliminates friction but has contributions from gravity as well as the spring.

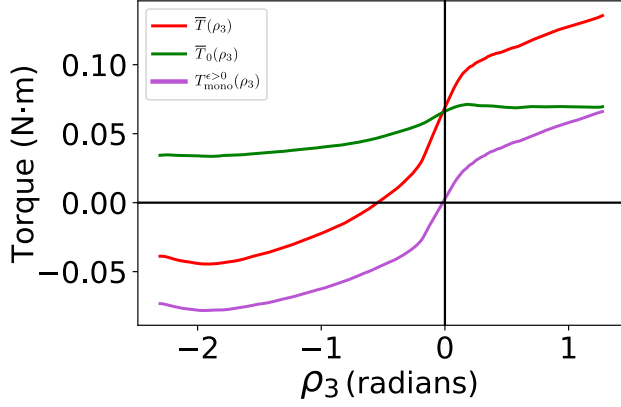


FIGURE 5.17: The difference between \bar{T} (red) and \bar{T}_0 (green), results in the torsion signal for the monostable branch: $T_{\text{mono}}^{\epsilon > 0}$ (purple).

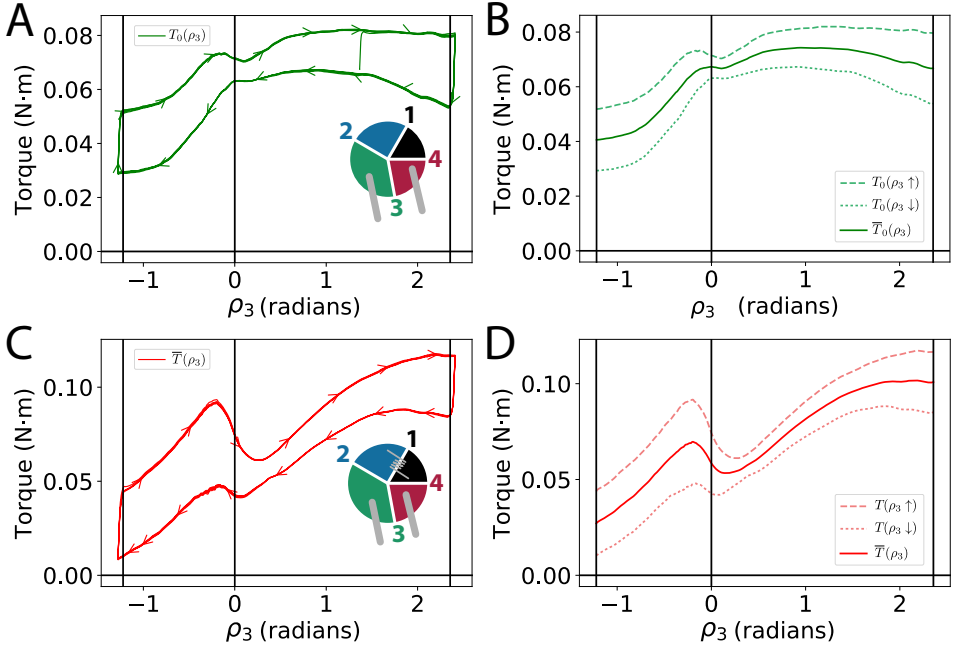


FIGURE 5.18: (A) Raw data T_0 of the bistable branch of an $\epsilon > 0$ vertex, without spring attached (see inset). (B) Mean signal \bar{T}_0 eliminates friction but has contributions from gravity. (C) Raw data \bar{T} of the bistable branch of an $\epsilon > 0$ vertex, *with* spring attached (see inset). (D) Mean signal \bar{T} eliminates friction but has contributions from gravity as well as the spring.

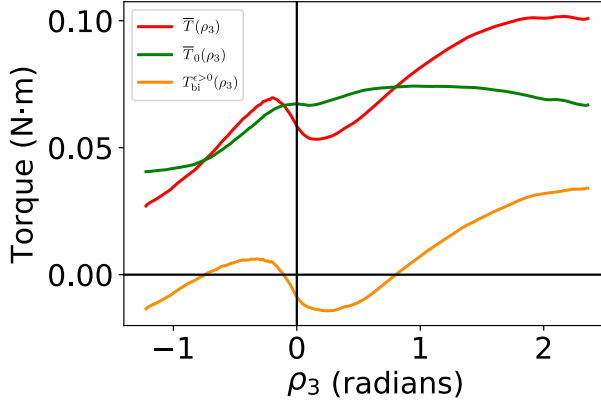


FIGURE 5.19: The difference between \bar{T} (red) and \bar{T}_0 (green), results in the torsion signal for the monostable branch: $T_{bi}^{\epsilon>0}$ (orange).

5.4.4 Experimental Energy Curves

In this section we translate our experimental data for the torque as function of fold angle to curves of the elastic energy as function of the fold angle. Subsequently we compare our experimental energy landscapes to our theoretical predictions of section 5.2.2. In addition, we experimentally characterize the energy barriers between the two folding branches, E_{pop} . In order for the three minima of our vertices to be stable, E_{pop} should be larger than the energy barrier separating the two global minima on the bistable branch, $E_{barrier}$, and also larger than the energy of the minimum on the monostable branch, E_{min} . We first discuss how to extract E_{min} from the spring potential. After this we show how we obtain the energy curves of the mono-, and bi-stable branches from the torque data, from which we can extract $E_{barrier}$. Finally, we perform an additional, linear compression experiment, which we use to characterize E_{pop} .

Together, our data shows good agreement to our theoretical model, and a clear separation of the two folding branches and the three stable states, for cone-like as well as saddle-like vertices.

Spring Potential

In this section we extract the spring potential from our experimental data, for both the cone-like vertices (section 5.4.3), and the saddle-like vertices

(section 5.4.3). In general, torque measurements can be integrated to obtain elastic energies:

$$E(\rho_i) = \int T(\rho_i) d\rho. \quad (5.9)$$

The data for $T(\rho_i)$ is shown in Fig. 5.9 and Fig. 5.11. We recall that the

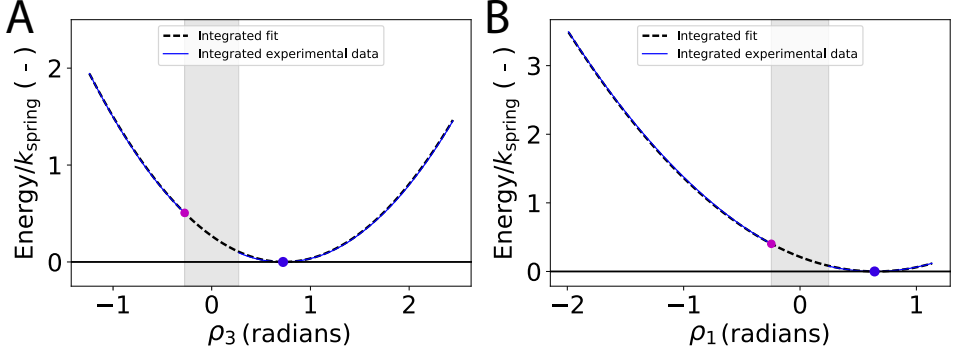


FIGURE 5.20: (A) Spring potential of the $\epsilon = -\pi/60$ vertex, extracted from the data in Fig. 5.9. (B) Spring potential of the $\epsilon = \pi/60$ vertex, extracted from the data in Fig. 5.11.

experimental data has a gap in the “forbidden” region, where ρ_3 , respectively ρ_2 , are pushed through the “pop-through” range where the vertex deviates from rigid-folding. Outside this gap, the torque data can be fitted well by a single linear function of the form $T = \kappa \cdot (\rho - \rho_0)$, where ρ_0 is the spring’s rest angle. Piecewise integration of the energy to the left and right of this gap, and fitting the energy offsets such that (i) $E = 0$ at $\rho_{1,3} = \rho_0$ and (ii) $E(\rho)$ is continuous, we obtain the energy curves shown in Fig. 5.20. Here we non-dimensionalize our data by the torsional spring constant, κ_{spring} .

Mono, and Bistable Energy Curves

In this section we extract the mono-, and bi-stable energy curves for both the cone-, and saddle-like vertices. First, we consider the cone-like, $\epsilon = -\pi/60$ vertex. In Fig. 5.21.A the solid purple line corresponds to the

experimental, dimensionless energy curve:

$$E_{\text{mono}}^{\epsilon < 0}(\rho_1) = \int [T_{\text{mono}}^{\epsilon < 0}(\rho_1)] d\rho_1, \quad (5.10)$$

where $T_{\text{mono}}^{\epsilon < 0}(\rho_1)$ is the torque signal displayed in Fig. 5.13. The bistable, dimensionless energy curve is displayed Fig. 5.21.B as the solid orange line:

$$E_{\text{bi}}^{\epsilon < 0}(\rho_1) = \int [T_{\text{bi}}^{\epsilon < 0}(\rho_1)] d\rho_1, \quad (5.11)$$

where $T_{\text{bi}}^{\epsilon < 0}(\rho_1)$ is the torque signal displayed in Fig. 5.15.

Second, we consider the saddle-like, $\epsilon = \pi/60$ vertex. In Fig. 5.21.C the solid purple line corresponds to the experimental, dimensionless energy curve:

$$E_{\text{mono}}^{\epsilon > 0}(\rho_3) = \int [T_{\text{mono}}^{\epsilon > 0}(\rho_3)] d\rho_3, \quad (5.12)$$

where $T_{\text{mono}}^{\epsilon > 0}(\rho_3)$ is the torque signal displayed in Fig. 5.17. The bistable, dimensionless energy curve is displayed Fig. 5.21.D as the solid orange line:

$$E_{\text{bi}}^{\epsilon > 0}(\rho_3) = \int [T_{\text{bi}}^{\epsilon > 0}(\rho_3)] d\rho_3, \quad (5.13)$$

where $T_{\text{bi}}^{\epsilon > 0}(\rho_3)$ is the torque signal displayed in Fig. 5.19.

The dashed lines in Fig. 5.21 indicate our theoretical predictions for the energy curves for the non-Euclidean vertices, using the appropriately determined spring potentials.

For the $\epsilon = -\pi/60$ vertex, we experimentally find that the minima B and C in Fig. 5.21.B are located at $\rho_1 \approx -0.66$ and $\rho_1 = 0.64$ respectively. Assuming a single spring located at ρ_3 with a rest angle of $0.73(1)$ rad (Fig. 5.9), theory predicts these minima to be located at $\rho_1 = \pm 0.73$ rad, which closely match the experiment. Furthermore, we find that the single minimum on the monostable branch is located at $\rho_1 \approx 0.01$ in the experimental data (Fig. 5.21.A), whereas we expect it to be located at $\rho_1 = 0.0$. While it is difficult to put a precise errorbar on our determination of the location of the minima, which is dominated by fabrication errors, play, clamping errors, and the shallowness of the minima, we estimate our errorbar to be larger than the signal, of the order of 0.1 rad.

For the $\epsilon = \pi/60$ vertex, we find that the minima E and F in Fig. 5.21.D are located at $\rho_3 \approx -0.74$ rad, and $\rho_3 \approx 0.80$ respectively. Based on theory –

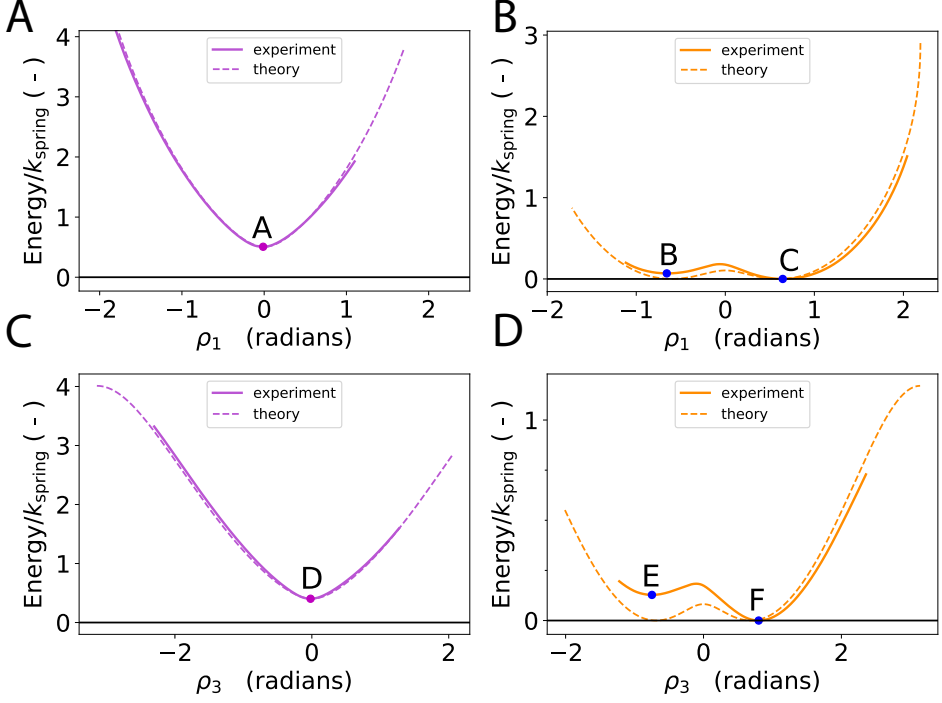


FIGURE 5.21: (A) Experimental and theoretical dimensionless energy curves for the monostable folding branch of the $\epsilon = -\pi/60$ vertex. The minimum energy is set to $E_{\min} = 0.51$, corresponding to the energy of the purple point in Fig. 5.20.A. (B) Energy curves for the bistable folding branch of the $\epsilon = -\pi/60$ vertex. (C) Energy curves for the monostable folding branch of the $\epsilon = \pi/60$ vertex. Hence the minimum energy is set to $E_{\min} = 0.40$, corresponding to the energy of the purple point in Fig. 5.20.B. (D) Energy curve for the bistable folding branch of the $\epsilon = \pi/60$ vertex. The letters indicating the various minima correspond those in Fig. 5.6.

assuming a single spring located at ρ_1 with a spring constant of $0.65(1)$ rad—we expect them to be located at $\rho_3 = \pm 0.69$. We suggest that the relatively large deviation of the location of the left minimum may be attributed to an offset in the torque signal of Fig. 5.19, which tilts the integrated potential shown in Fig. 5.21.D, and therefore also shifts the location of the minima. We note that the distance between the two minima is within 5% of what we expect from theory. Finally, the single minimum on the monostable branch

is located at $\rho_3 \approx 0.02$ in the experimental data (Fig. 5.21.C), whereas we expect it to be located at $\rho_3 = 0.0 \pm 0.1$.

We conclude that the four experimental energy curves shown in Fig. 5.21 demonstrate that theory and experiment agree closely, as the shape of the experimental mono- and bistable branches, as well as the location of the experimental minima, closely match the dashed theoretical curves.

5.4.5 Vertex Pop-Through

In this section we characterize the pop-through behavior of our vertices. The energy barrier for pop-through, E_{pop} , is presumably set by hinge stretching and plate bending. These two effects both directly influence the peak shown in Fig. 5.9 and Fig. 5.11. In these experiments we see that the torque signal rises (drops) relatively slowly, until it hits a peak value, after which the torque suddenly drops due to the pop-through instability, resulting in a near vertical slope. This is akin to the way the load-displacement curve of a simple von Mises truss becomes asymmetric when, instead of perfect displacement control, it is loaded with a spring, see Fig. 5.22 and p.278–p.285 of [75].

In order to quantify E_{pop} , we use a linear compression testing machine (Instron 3361) to measure the force required to flatten the vertex, without any torsional spring attached to the vertex. A schematic of our experiment is depicted in 5.22. We put our vertices on a flat surface, and measure the energy necessary to flatten it, which can be calculated from $\Delta E = \int F_z dz$, where F_z is the force exerted by the compression tester. When loading the vertex, F_z will rise to a maximum value $F_z = F_{z,\text{peak}}$, starting from $F_z = 0$ (Fig. 5.22.A,B). After this, F_z will drop back to $F_z = 0$ for the fully flattened vertex. On the contrary, E will monotonically increase, and we take the maximum value of E for the fully compressed vertex as the pop-through energy barrier, E_{pop} .

The setup that we use in the vertical Instron testing machine consist of single $\epsilon \approx -0.052$, cone-like vertex, with geometric parameters identical to the one used for the experiments in section 5.4. To this vertex we glue 4 truncated spheres: three to the bottom, at approximately 120° apart along the periphery of the vertex, and one to the top, near the center of the vertex – see Fig. 5.23.A. The vertex is then placed in between two parallel circular plates with a diameter of 20.0 cm, see Fig. 5.23.B. This setup creates a well defined contact on the top and the bottom, and avoids the need for any

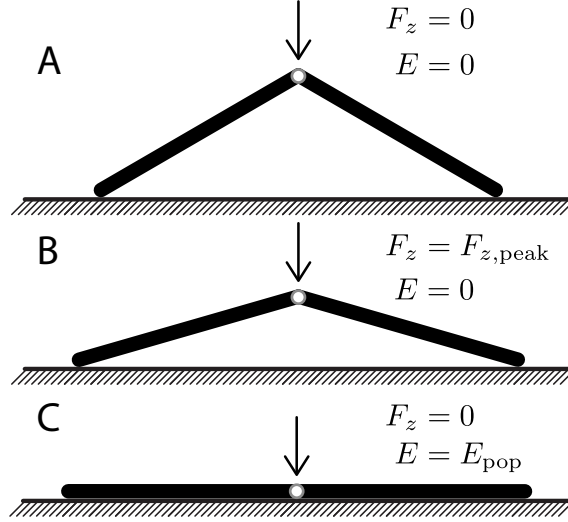


FIGURE 5.22: Side-view schematic of the setup used to measure the energy necessary to pop-through the vertex, E_{pop} . (A) Start of the experiment: the vertex is uncompressed, $E = 0$, and $F_z = 0$. (B) Approximately halfway the experiment, the force exerted in the z direction will hit a maximum F_z , $E > 0$. (C) The vertex is fully compressed. Vertically exerted force is once again $F_z = 0$, whereas the elastic energy is now maximal, $E = E_{pop}$.

precise parallel alignment of the top and bottom plate. Lastly, the spheres as well as the aluminum plates are all coated with silicone grease in order to minimize friction.

A similar setup is used for the $\epsilon \approx 0.052$, saddle like vertex. However, as the pop-through transition in this case transforms the vertex from one saddle configuration to another, pushing on the vertex on a single point near the center does not pop the vertex through. Therefore, we use a different arrangement of spheres: two spheres are glued to the bottom of the vertex, on opposite sides, and two on the top, also on opposite sides, where the two pairs approximately form a cross (Fig. 5.23.C). A picture of this configuration is shown in Fig. 5.23.D.

The result of the measurement for the $\epsilon \approx -0.052$ vertex is shown in Fig. 5.24.A. The measurement protocol consists of lowering the top plate until it is about to make contact with the top sphere, as depicted in Fig. 5.23.B. We then impose an up and down sweep of the z -displacement, Δz , where we use a strain rate of 0.1 mm/s, and a maximum Δz of 1.6 mm

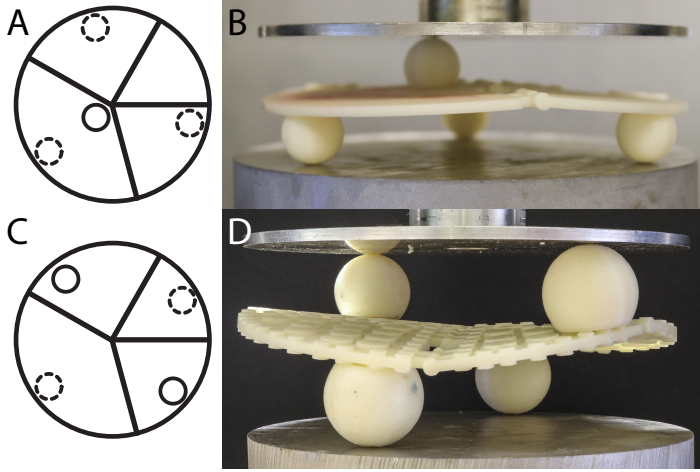


FIGURE 5.23: (A) Top-view schematic of the $\epsilon < 0$, hat-like vertex, where the position of the attached spheres is indicated by the circles; dashed lines indicate the spheres are attached to the underside of the vertex. (B) Side view of the $\epsilon < 0$ in our compression setup. (C) Top-view schematic of the $\epsilon > 0$, saddle-like vertex, where the position of the attached spheres is indicated by the circles; dashed lines indicate the spheres are attached to the underside of the vertex. (D) Side view of the $\epsilon > 0$ vertex in our compression setup.

(positive Δz means pushing down). This maximum is increased by 1.0 mm every second cycle to $\Delta z = 2.6, 3.6, 4.6, 5.6$ mm, and finally $\Delta Z = 6.6$ mm. On the last cycle we see that the vertex pops through, at $\Delta z \approx 6.28$ mm. We see that from $\Delta z \lesssim 3$ mm, F_z increases to a peak value, which we determine to be $F_{z,\text{peak}} = 19.5 \pm 0.5$ N, obtained by taking the average maximum over seven up sweeps – the error bar represents the standard deviation of seven maximum values. After hitting this peak value, F_z monotonically decreases all the way down to $F_z = 0$; the top plate staying in contact all the way till the pop-through point. The amount of work necessary to pop-through the vertex can now be calculated by integrating the signal of Fig. 5.24.A, as we have done in Fig. 5.24.B, and we find a value of $W_{\text{pop}} = 0.065$ J. Finally, we note the large discrepancy between F_z for the upward sweeps, and the downward sweeps. We attribute this discrepancy to friction in the hinges, which we also witnessed in our torsion experiments (section 5.4). Hence, the amount of work is not equal to the maximum elastic energy stored in the deformed configuration, E_{pop} .

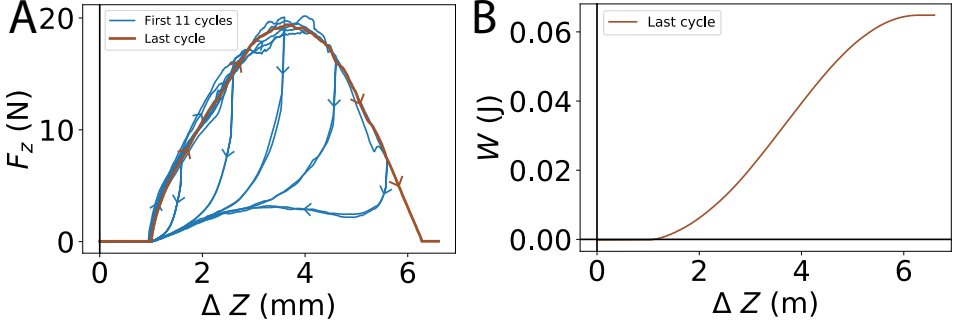


FIGURE 5.24: (A) Data of the compression experiment depicted in Fig. 5.23, for a $\epsilon \approx -0.052$ rad vertex. Top plate makes contact with the vertex $\Delta z = 1.0$ mm, and is further compressed until $\Delta z = 1.6$ mm using up an down sweeps of Δz , where the maximum Δz is increased by 1.0 mm every other sweep. The last sweep (brown) reaches a maximum of $\Delta z = 6.6$ mm, where we witness a pop-through event at $\Delta z = 6.275$ mm. (B) Integrated signal of (A); we find $W_{\text{pop}} = 0.065$ J.

The result of the measurement for the $\epsilon \approx 0.052$ vertex is shown in Fig. 5.25.A. In this experiment the top plate makes contact with the vertex at a z -displacement of around $\Delta z = 1.0$ mm, and is further compressed until $\Delta z = 6.2$ mm, which is just before the pop-through point, for three up an down sweeps. On next compression cycle we increase the maximum z -displacement to $\Delta z = 10$ mm, and we witness a pop-through event at $\Delta z = 7.37$ mm. The sudden drop in F_z at this point is where the vertex pops through, and the top plate loses contact. The fact this happens before F_z drops to zero, probably indicates the vertex is not perfectly flattened, which would require precise alignment of the four attached spheres (unlike in the $\epsilon > 0$ case, where the four contacts are self-aligning). The average peak load found in this case is $F_{z,\text{peak}} = 15.5 \pm 0.1$ N, which was determined by taking the average of the peak load over four up sweeps, and likewise for the errorbar, which corresponds to the standard deviation of these four peak loads. This peak load is of the same order as the peak load found for the $\epsilon \approx 0.052$ vertex. The integrated signal is equivalent to the amount of work necessary to pop the vertex through, and is displayed in Fig. 5.25.C. The ‘pop-through work’ is calculated from the total area under the curve in Fig. 5.25.A, which results in $W_{\text{pop}} = 0.072$ J, which is approximately 10% higher than the W_{pop} value found for the $\epsilon > 0$ case. Our data clearly shows that this barrier is significantly larger than the energy scales on a single

branch; hence once popped, the vertex will stay on one of these branches. We also note that W_{pop} for the $\epsilon > 0$ and $\epsilon < 0$ vertices are similar. This suggests that hinge stretching constitutes the main deviation from rigid folding; if instead plate bending would dominate, $\epsilon > 0$ vertices can easily be popped, but $\epsilon < 0$ vertices not². Finally, the monotonous increase of the “in plane” forces, while F_z goes to zero, suggests that frictional forces must be important, even if the friction coefficient is small.

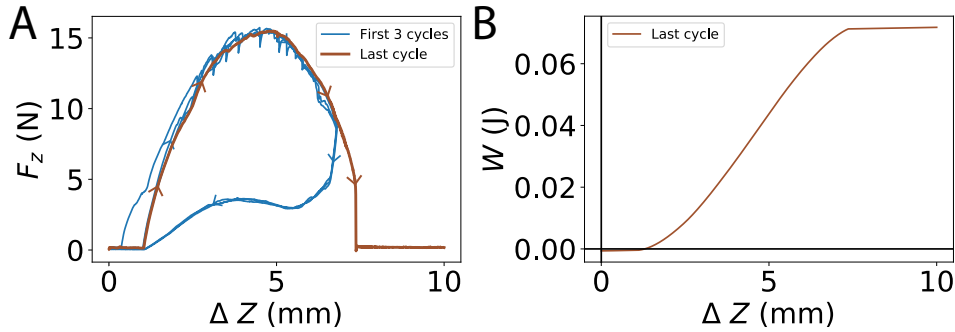


FIGURE 5.25: (A) Data of the compression experiment depicted in Fig. 5.23, for an $\epsilon \approx 0.052$ vertex. Top plate makes contact with the vertex at $\Delta z = 1.0$ mm, and is further compressed until a maximum of $\Delta z = 6.2$ mm using a triangular waveform, for 3 cycles. On the last cycle Δz is increased to $\Delta z = 10.0$ mm, where we witness a pop-through event at $\Delta z = 7.37$ mm. (B) Integrated signal of (A): we find $W_{\text{pop}} = 0.072$ J.

In order to determine how W_{pop} depends on the angular surplus (or deficit), we 3D printed four additional $\epsilon < 0$ vertices, for $\epsilon = -\pi/120 \approx -0.025$ rad, $\epsilon = -\pi/72 \approx -0.044$ rad, $\epsilon = -\pi/45 \approx -0.070$ rad, and $\epsilon = -\pi/30 \approx -0.105$ rad. The $\epsilon \approx -0.026$ rad vertex has a negligible bump, which in particular is not enough to support the vertex’s weight when put in a ‘cone up’ configuration on a flat surface – this is likely due to small but finite play of the hinges. On the other extreme, repeatedly popping through the $\epsilon \approx -0.105$ rad vertex breaks one of the outermost hinges of the vertex within ten cycles, indicating the stresses put on these hinges is beyond the yield stress of the material (ABS). The results of the compression tests of the remaining three vertices: $\epsilon \approx \{-0.044, -0.052, -0.070\}$, are shown in Fig. 5.26.A. The curves here correspond to the last compression cycle of

²This can readily be demonstrated by making non-Euclidean vertices out of paper, where the ‘pop-through’ transition is facilitated by bending the paper.

each test, where the brown curve in Fig. 5.26.A corresponds to the brown curve in Fig. 5.24.A. To characterize the increase in bump size as a function of surplus angle ϵ , we integrate each curve to find the energy underneath each curve, and plot this value as function of ϵ , as shown in Fig. 5.26.B. The points suggest there is a linear relationship between the amount of work, W_{pop} , and the surplus angle, ϵ . A fit of the form $W_{\text{pop}} = a \cdot \epsilon + b$ is displayed in Fig. 5.26.B as the black line. We find $a = -3.34 \text{ J/rad}$ and $b = -0.109 \text{ J}$, which translates to a cut-off point of $\epsilon \approx -0.033 \text{ rad}$. This is consistent with the observation that the $\epsilon \approx -0.026 \text{ rad}$ vertex has a negligible barrier. We note that this relationship is specific to this geometry and vertex size. Most hinge stretching and bending takes place around the periphery of the vertex, and the maximum stresses exerted on the hinges will decrease if we print a vertex with a smaller radius, but otherwise identical geometric parameters. We do expect however, to find a roughly similar relationship between W_{pop} and ϵ for $\epsilon > 0$ vertices, as W_{pop} for the $\epsilon = -0.052$ and $\epsilon = +0.052$ vertices differs by only 10%.

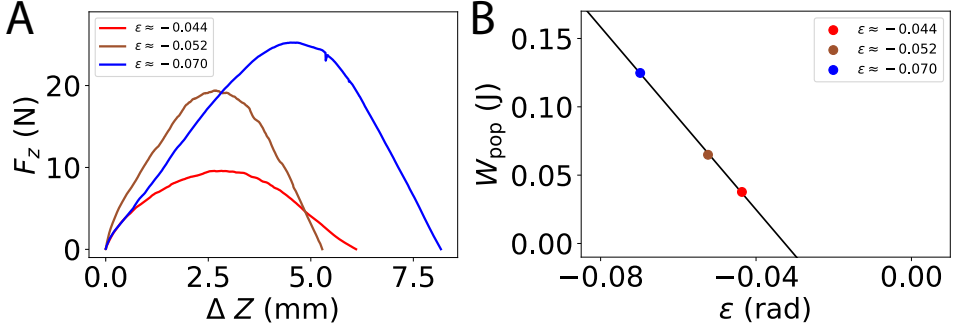


FIGURE 5.26: (A) Last compression cycle of three different vertices, with $\epsilon \approx -0.044$, $\epsilon \approx -0.052$, and $\epsilon \approx -0.070$. The brown, $\epsilon \approx -0.052$ curve corresponds to the brown curve displayed in Fig. 5.24.A. (B) W_{pop} found by integrating the three curves in (A), black line indicates a linear fit (see text).

Finally, we observe that W_{pop} , E_{min} and E_{barrier} can all be expressed in terms of dimensionless units, e.g:

$$\tilde{W}_{\text{pop}} = W_{\text{pop}}/k_{\text{spring}}, \quad (5.14)$$

which yields $\tilde{W}_{\text{pop}} \approx 1.43$ for the $\epsilon \approx -0.052$ vertex, and $\tilde{W}_{\text{pop}} \approx 1.57$ for the $\epsilon \approx 0.052$ vertex. From Fig. 5.21 we can see that $\tilde{E}_{\text{min}} \ll \tilde{W}_{\text{pop}}$ and

$\tilde{E}_{\text{barrier}} < \tilde{W}_{\text{pop}}$, which is consistent with our observation that both vertices are tri-stable.

5.5 Conclusion

In this chapter we have shown how to create experimentally robust *tristable vertex*. We use weakly non-flat 4-vertices that exhibit two folding branches that are separated by a finite energy barrier, controlled by a non-rigid “pop-through transition. By dressing one of the folds with a torsional spring, we can turn one of the two folding branches into a bistable branch, thereby creating tristable vertices. The fact that this same mechanism works for both cone-like ($\epsilon < 0$) as well as saddle-like ($\epsilon > 0$) vertices opens up the possibility to create corrugated sheets composed out of tristable non-flat vertices, for which we need both saddle-like and cone-like vertices.

FOLD ANGLES

In this appendix we will derive closed form expressions for the relations between the fold angles of a generic 4-vertex. Expressions in the literature are either in implicit form [48, 76], are for flat foldable vertices only [16, 35, 76], or fail to clearly distinguish between the two possible discrete folding branches [16, 48]. The derivation shown here is originally by Rémi Menaut, and was shortened by Scott Waitukaitis. In addition we will show how the fold angles of a given 4-vertex and its supplement relate to each other.

A Euclidean 4-vertex consists of four rigid plates with sector angles α_i connected by four folds or hinges, where $\sum \alpha_i = 2\pi$ and we assume that all sector angles are unequal and smaller than π (Fig. A.1.A). The non-flat, folded states are characterized by the folding angles ρ_i , defined as the deviation from in-plane alignment between adjacent plates i and $i + 1$ (modulo 4). 4-vertices are equivalent to non-intersecting spherical mechanisms, allowing to represent their folded state accordingly (Fig. A.1.B). The fold angles are equal to the angle between the great circles at the point they meet, see ρ_1 in Fig. A.1.B, where we note that ρ_1 here is positive, as it is oriented counterclockwise.

Folding Branches

It was first shown by Huffman that a folded Euclidean 4-vertex will always have one fold whose sign is *unique*, i.e. the angle is opposite in sign from the other folding angles [28, 48, 58]. We call these folds *odd folds*, and these odd folds always straddle a common *odd plate*. A necessary and sufficient condition for the sector angle of the odd plate is the inequality

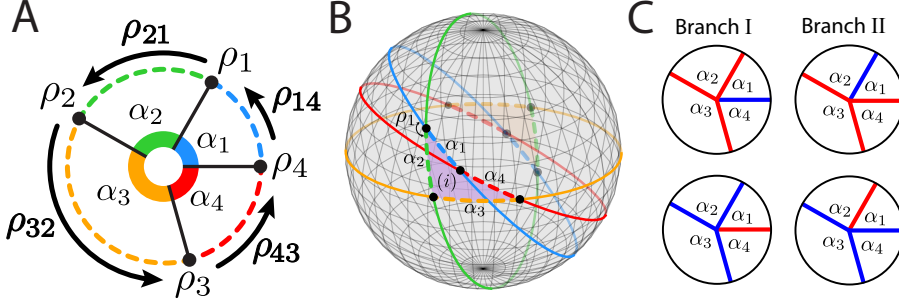


FIGURE A.1: (A) A generic 4-vertex with sector angles α_i , fold angles ρ_i , and fold operators $\rho_{i+1,i}$. (B) An origami vertex (i) can be modeled as a spherical mechanism. Dashed lines trace out the two vertices related by mirror symmetry, whereas the solid lines trace out supplemented vertices. (C) The four possible Mountain-Valley (colored red and blue respectively) arrangements of a generic Euclidean 4-vertex.

$\alpha_i + \alpha_{i+1} < \alpha_{i+2} + \alpha_{i+3}$. A generic 4-vertex always has two odd folds, which straddle a common *odd* plate [28]; we define our vertices such that ρ_4 and ρ_1 are the odd folds, and α_1 is the odd plate. Together with the $\{\rho_i\} \leftrightarrow \{-\rho_i\}$ symmetry, this yields four distinct mountain-valley patterns for a given 4-vertex, shown in Fig. A.1.C. We denote the folding branches where ρ_4 or ρ_1 has the opposite sign by I and II respectively.

Folding Operators

Along a given branch, 4-vertices have one continuous degree of freedom, and the relations between folding angles are anti-symmetric $\rho_i(-\rho_j) = -\rho_i(\rho_j)$ and bijective; we define folding operators $\rho_{i+1,i}^{I,II}$ which map the fold angles adjacent to plate i : $\rho_{i+1,i}^{I,II}(\rho_i) = \rho_{i+1}$, and suppress the index I and II when possible. Here we use the relations between the folding angles to show that the folding operators of a vertex, $\rho_{i+1,i}$ and its supplement, $\rho'_{i+1,i}$ are related as $\rho'_{i+1,i} = -\rho_{i+1,i}$.

We consider a folded state of a 4-vertex, and aim to express all fold angles as function of ρ_4 . We schematically represent the arc lengths and dihedral angles of the folded states as seen on the Euclidean sphere by diagrams such as Fig. A.2.B,C. We now consider the arc length λ_{41} between folds ρ_3 and ρ_1 , depicted in Fig. A.1.B,C. Using the spherical law of cosines,

we obtain:

$$\cos \lambda_{34} = \cos \alpha_4 \cos \alpha_1 - \sin \alpha_4 \sin \alpha_1 \cos \rho_4 . \quad (\text{A.1})$$

The arc length λ_{34} is part of two spherical triangles, one with dihedral angles $\pi - \sigma_4$, $\pi - \sigma_1$ and $\pi - \sigma_3$, and the other with $\pi - \tau_1$, $\pi - \tau_2$ and $\pi - \tau_3$. Making use of the shorthand notation,

$$A(a, b, c) \equiv \arccos \left(\frac{\cos a \cos b - \cos c}{\sin a \sin b} \right) , \quad (\text{A.2})$$

and repeatedly using the spherical law of cosines, the dihedral angles σ_i and τ_i are,

$$\begin{aligned} \sigma_1 &= A(\lambda_{34}, \alpha_1, \alpha_4) & \tau_1 &= A(\alpha_2, \lambda_{34}, \alpha_3) \\ \sigma_3 &= A(\alpha_4, \lambda_{34}, \alpha_1) & \tau_2 &= A(\alpha_3, \alpha_2, \lambda_{34}) \\ \sigma_4 &= A(\alpha_1, \alpha_4, \lambda_{34}) & \tau_3 &= A(\lambda_{34}, \alpha_3, \alpha_2) . \end{aligned}$$

These are all functions of ρ_4 through their dependence on λ_{34} .

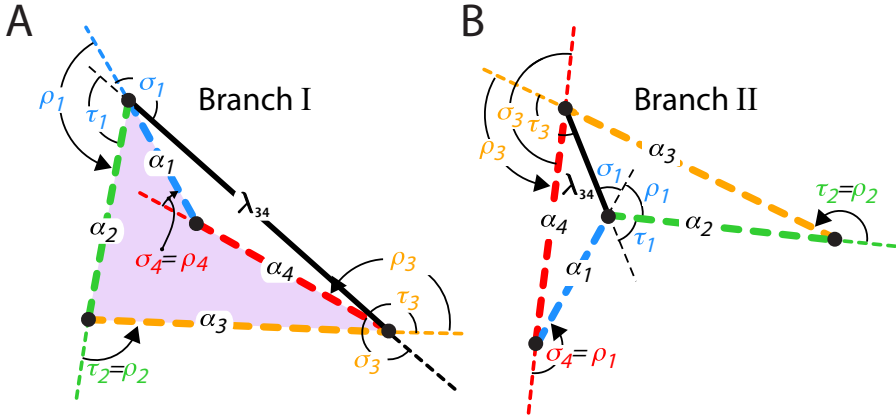


FIGURE A.2: (A) Simplified diagram of a 4-vertex (i) folded in Branch I, as in Fig. A.1.B. (B) Simplified diagram of a 4-vertex folded in Branch II.

We obtain the folding angles from σ_i and τ_i ; taking care regarding the relative signs of the fold angles on each branch, the exact equations for

$\rho_4 > 0$ are,

$$\rho_1^{I/II} = -\pi + \sigma_1 \mp \tau_1, \quad (\text{A.3})$$

$$\rho_2^{I/II} = \mp \tau_2, \quad (\text{A.4})$$

$$\rho_3^{I/II} = -\pi + \sigma_3 \mp \tau_3, \quad (\text{A.5})$$

where the minus sign in \mp corresponds to branches I , and the plus sign in \mp to branch II . Because of reflection symmetry in the flat-state plane, these equations are antisymmetric: $[\rho_i^{I/II}(\rho_4 < 0) = -\rho_i^{I/II}(\rho_4 > 0)]$. Similarly, we can obtain expressions for any fold angle as function of any other fold angle.

The operator ρ_{14} follows directly from Eq. A.3. Using these explicit expressions, we now show that $\rho'_{i+1,i} = -\rho_{i+1,i}$. For the supplemented vertex, we modify the sector angles from α_i to $\alpha'_i = \pi - \alpha_i$. First, note that the expression for $\cos(\lambda_{34})$, Eq. A.1, remains identical under this transformation, making use of the identity $\cos(-x) = \cos(x)$ and $\sin(-x) = -\sin(x)$. Second, note that we can write:

$$\begin{aligned} \sigma'_1 &= A(\lambda_{34}, \alpha'_1, \alpha'_4), \\ &= \arccos\left(\frac{-\cos \lambda_{34} \cos \alpha_1 + \cos \alpha_4}{\sin \lambda_{34} \sin \alpha_1}\right) \\ &= \pi - A(\lambda_{34}, \alpha_1, \alpha_4), \\ &= \pi - \sigma_1 \end{aligned} \quad (\text{A.6})$$

using the identity: $\arccos(-x) = \pi - \arccos(x)$. Likewise, we have $\tau'_1 = \pi - \tau_1$. We therefore find (dropping the branch notation),

$$\begin{aligned} \rho'_1 &= -\pi + \sigma'_1 \mp \tau'_1, \\ &= -\pi + (\pi - \sigma_1) \mp (\pi - \tau_1), \\ &= \pi - \sigma_1 \pm \tau_1, \\ &= -\rho_1. \end{aligned} \quad (\text{A.7})$$

Hence, $\rho'_{14} = -\rho_{14}$, and we can trivially extend this argument to show that $\rho'_{i+1,i} = -\rho_{i+1,i}$.

4-VERTEX AS A SPHERICAL MECHANISM

The operator symmetry $\rho'_{ij} = -\rho_{ij}$ derived in appendix A, can also be derived graphically. As shown before, a 4-vertex can be modeled as a spherical mechanism, which can be represented on the surface of a sphere (Fig. A.1.B). In Fig. B.1.A we schematically represent a 4-vertex (i) in a folded configuration, by using a pseudo-Mercator projection. Extending the arcs of vertex (i), we obtain four directed great circles. The intersection of circle i and $i + 1$ –indicated by the black circles– correspond to the hinges of spherical linkage (i), whereas their respective angle corresponds to fold angle ρ_i . We define the fold angles ρ_i as positive when ρ_i turns counterclockwise. The grey circles indicate the antipodal points of the black points of vertex (i). Along each directed circle we name the four arc lengths: $\alpha_i, \bar{\alpha}_i, \dot{\alpha}_i, \tilde{\alpha}_i$, where $\dot{\alpha}_i = \alpha_i$, $\bar{\alpha}_i = \tilde{\alpha}_i = \pi - \alpha_i$, and $\alpha_i + \bar{\alpha}_i + \dot{\alpha}_i + \tilde{\alpha}_i = 2\pi$ (also see Fig. B.1.A). Furthermore, any pair of great circles intersects at two locations, and because they are great circles, the angles around an intersection point are identical in magnitude to the angles around its antipodal point.

We first show that we can derive the relationship between the fold angles (and fold operators) of the four related vertices (i), (ii), (iii) and (iv) of Fig. 2.2. Our goal is to relate the fold angles of vertices (ii), (iii) and (iv) to the fold angles ρ_i of vertex (i) – shaded pink in Fig. B.1.A. First, vertex (ii) –shaded orange in Fig. B.1.A– can be found by connecting the four antipodal (grey) nodes, which consists of arc lengths $\dot{\alpha}_i$. When we

consider the fold angles of this vertex (running clockwise), we see that they are all oppositely oriented with respect to those of vertex (i), and therefore each pick up a minus sign. Thus, if a vertex can be in a configuration with folding angles $\{\rho_i\}$, it can also be in a configuration with folding angles $\{-\rho_i\}$, consistent with $\rho_j(-\rho_i) = -\rho_j(\rho_i)$

Second, we consider vertex (iii), which is shaded purple in Fig. B.1.B. This vertex consists of arc lengths: $\tilde{\alpha}_1, \tilde{\alpha}_2, \tilde{\alpha}_3, \tilde{\alpha}_4$, running clockwise. We see that in this case, only the fold angle around the antipodal (gray) nodes are reversed. The same holds true for vertex (iv) ($\bar{\alpha}_1, \bar{\alpha}_2, \bar{\alpha}_3, \bar{\alpha}_4$), which is shaded orange in Fig. B.1.B. As the resultant fold angles are alternating in sign for both vertex (iii) and (iv), and we find: $\rho_{i+1}(\rho_i) = -\rho_{i+1}(\rho_i)$, or $\rho'_{ij} = -\rho_{ij}$, using the operator notation. We finally note that vertex (i) in Fig. B.1.A depicts a vertex folded on branch I, where ρ_4 is opposite to the three other folds, but the relations above also hold on branch II (where ρ_1 is opposite in sign).

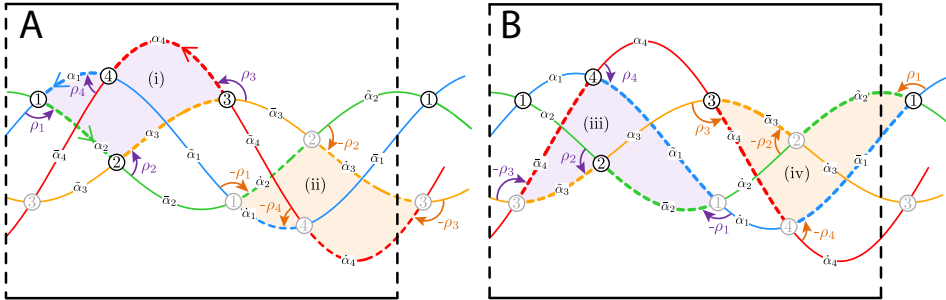


FIGURE B.1: (A) Simplified Mercator projection of a vertex (i) as shown in Fig. A.1, and its mirror image on the other side of the sphere (ii). (B) Simplified Mercator projection of two the two supplemented vertices, (iii) and (iv). Dashed line indicates periodic boundary. For details see text.

Besides the related Euclidean vertices (i)-(iv) and their representative spherical mechanisms (also termed ‘folding linkages’ [77]), there are an additional 12 related spherical mechanisms [78, 79]. All of these represent non-Euclidean vertices. Some of these mechanisms however, are self-intersecting, meaning they can not be converted into a 4-vertex as the plates would intersect. To study these additional spherical mechanisms in detail, we use the same pseudo-Mercator map as in Fig. B.1, in Fig. B.2. On this map we express all 16 arc lengths ($\alpha_i, \bar{\alpha}_i, \dot{\alpha}_i, \tilde{\alpha}_i$), as well as the

angles around each node (ρ_i and ρ'_i) in terms of the arc lengths and angles of the original counterclockwise oriented vertex (i), which is depicted by the dashed line.

An example of one the 12 non-Euclidean spherical mechanisms is shown in light-blue in Fig. B.2, which we denote as $\tilde{\alpha}_1\dot{\alpha}_2\bar{\alpha}_3\alpha_4$. When we consider the magnitude of the angles between consecutive links of this mechanism, we find that they are: $\rho'_1, \rho'_2, \rho'_3, \rho'_4$. The signs of these angles can be found by comparing the orientation of these angles to those of the original vertex (vertex (i) in Fig. B.1.A), where the orientation of the mechanism itself is set by the colors of the segments (blue \rightarrow green \rightarrow yellow \rightarrow red). In this case, the orientation of the angles in the mechanism $\tilde{\alpha}_1\dot{\alpha}_2\bar{\alpha}_3\alpha_4$ are respectively: counterclockwise, counterclockwise, clockwise, and counterclockwise. When comparing this to vertex (i), we see that both ρ'_3 and ρ'_4 are oppositely oriented, which is why they obtain a minus sign. The folding angles of this mechanism are therefore $\rho'_1, \rho'_2, -\rho'_3, -\rho'_4$. An example of a self-intersecting non-Euclidean mechanism is colored green in Fig. B.2. This mechanism is denoted as $\bar{\alpha}_1\tilde{\alpha}_2\dot{\alpha}_3\dot{\alpha}_4$. Comparison of the angles of this mechanism to those of vertex (i) yields: $\rho_1, \rho'_2, -\rho_3, \rho'_4$.

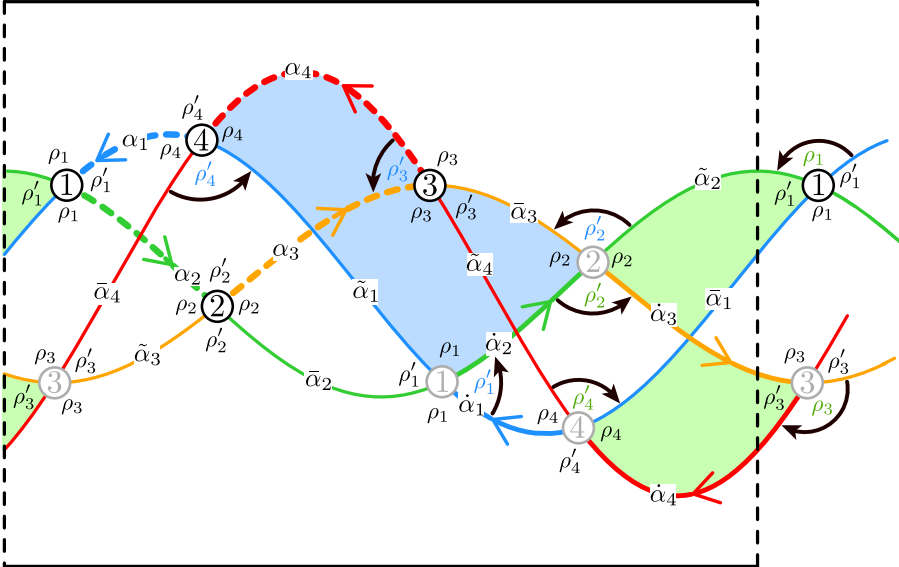


FIGURE B.2: Simplified mercator projection of the flat vertex shown in Fig. A.1 (dashed lines), folded on branch I. Dashed lines indicate periodic boundary.

In Table B.1 we list all 16 spherical mechanisms and their respective arc lengths (β_i), and fold angles (θ_i), expressed in terms of the arc lengths and fold angles of the vertex $\alpha_1\alpha_2\alpha_3\alpha_4$. Although the fold angles derived here are derived from Fig. B.2, which depicts a spherical mechanism on branch I (where the sign of ρ_4 on vertex $\alpha_1\alpha_2\alpha_3\alpha_4$ is opposite to the other three), we note that the expressions are valid for branch II as well (where the sign of ρ_1 on vertex $\alpha_1\alpha_2\alpha_3\alpha_4$ is opposite to the other three). In addition to the fold angles θ_i , we also display the sign of θ_i on both branch I and branch II. From the $\bar{\alpha}_1\tilde{\alpha}_2\dot{\alpha}_3\dot{\alpha}_4$ mechanism we know that self intersecting mechanisms have two consecutive positive fold angles, and two consecutive negative fold angles. We therefore see that mechanisms $\alpha_1\alpha_2\dot{\alpha}_3\bar{\alpha}_4$, $\tilde{\alpha}_1\bar{\alpha}_2\alpha_3\alpha_4$, $\dot{\alpha}_1\dot{\alpha}_2\bar{\alpha}_3\bar{\alpha}_4$, and $\bar{\alpha}_1\tilde{\alpha}_2\dot{\alpha}_3\dot{\alpha}_4$ are self-intersecting on branch I. On branch II we find that $\alpha_1\tilde{\alpha}_2\bar{\alpha}_3\alpha_4$, $\tilde{\alpha}_1\dot{\alpha}_2\dot{\alpha}_3\bar{\alpha}_4$, $\dot{\alpha}_1\bar{\alpha}_2\tilde{\alpha}_3\dot{\alpha}_4$, and $\bar{\alpha}_1\alpha_2\alpha_3\tilde{\alpha}_4$ are self intersecting. Other than the four Euclidean vertices $\alpha_1\alpha_2\alpha_3\alpha_4$, $\tilde{\alpha}_1\bar{\alpha}_2\tilde{\alpha}_3\bar{\alpha}_4$, $\dot{\alpha}_1\dot{\alpha}_2\dot{\alpha}_3\dot{\alpha}_4$, $\bar{\alpha}_1\tilde{\alpha}_2\bar{\alpha}_3\tilde{\alpha}_4$, this leaves four spherical mechanisms that represent non-Euclidean vertices which can fold from branch I to branch II, these are: $\alpha_1\tilde{\alpha}_2\dot{\alpha}_3\bar{\alpha}_4$, $\tilde{\alpha}_1\dot{\alpha}_2\bar{\alpha}_3\alpha_4$, $\dot{\alpha}_1\bar{\alpha}_2\alpha_3\tilde{\alpha}_4$, $\bar{\alpha}_1\alpha_2\bar{\alpha}_3\dot{\alpha}_4$.

Arc Lengths				Folding Angle				Sign (Branch I)				Sign (Branch II)			
β_1	β_2	β_3	β_4	θ_1	θ_2	θ_3	θ_4	θ_1	θ_2	θ_3	θ_4	θ_1	θ_2	θ_3	θ_4
α_1	α_2	α_3	α_4	ρ_1	ρ_2	ρ_3	ρ_4	+	+	+	-	-	+	+	+
α_1	$\tilde{\alpha}_2$	$\bar{\alpha}_3$	α_4	$-\rho'_1$	$-\rho_2$	$-\rho'_3$	ρ_4	-	-	-	-	+	-	-	+
α_1	α_2	$\tilde{\alpha}_3$	$\bar{\alpha}_4$	ρ_1	$-\rho'_2$	$-\rho_3$	$-\rho'_4$	+	-	-	+	-	-	-	-
α_1	$\tilde{\alpha}_2$	$\dot{\alpha}_3$	$\bar{\alpha}_4$	$-\rho'_1$	ρ'_2	ρ'_3	$-\rho'_4$	-	+	+	+	+	+	+	-
$\tilde{\alpha}_1$	$\tilde{\alpha}_2$	$\tilde{\alpha}_3$	$\bar{\alpha}_4$	$-\rho_1$	ρ_2	$-\rho_3$	ρ_4	-	+	-	-	+	+	-	+
$\tilde{\alpha}_1$	$\dot{\alpha}_2$	$\dot{\alpha}_3$	$\bar{\alpha}_4$	ρ'_1	$-\rho_2$	ρ'_3	ρ_4	+	-	+	-	-	-	+	+
$\tilde{\alpha}_1$	$\bar{\alpha}_2$	α_3	α_4	$-\rho_1$	$-\rho'_2$	ρ_3	$-\rho'_4$	-	-	+	+	+	-	+	-
$\tilde{\alpha}_1$	$\dot{\alpha}_2$	$\bar{\alpha}_3$	α_4	ρ'_1	ρ'_2	$-\rho'_3$	$-\rho'_4$	+	+	-	+	-	+	-	-
$\dot{\alpha}_1$	$\dot{\alpha}_2$	$\dot{\alpha}_3$	$\dot{\alpha}_4$	$-\rho_1$	$-\rho_2$	$-\rho_3$	$-\rho_4$	-	-	-	+	+	-	-	-
$\dot{\alpha}_1$	$\bar{\alpha}_2$	$\tilde{\alpha}_3$	$\dot{\alpha}_4$	ρ'_1	ρ_2	ρ'_3	$-\rho_4$	+	+	+	+	-	+	+	-
$\dot{\alpha}_1$	$\dot{\alpha}_2$	$\bar{\alpha}_3$	$\bar{\alpha}_4$	$-\rho_1$	ρ'_2	ρ_3	ρ'_4	-	+	+	-	+	+	+	+
$\dot{\alpha}_1$	$\bar{\alpha}_2$	α_3	$\bar{\alpha}_4$	ρ'_1	$-\rho'_2$	$-\rho'_3$	ρ'_4	+	-	-	-	-	-	-	+
$\bar{\alpha}_1$	$\tilde{\alpha}_2$	$\bar{\alpha}_3$	$\tilde{\alpha}_4$	ρ_1	$-\rho_2$	ρ_3	$-\rho_4$	+	-	+	+	-	-	+	-
$\bar{\alpha}_1$	α_2	α_3	$\tilde{\alpha}_4$	$-\rho'_1$	ρ_2	$-\rho'_3$	$-\rho_4$	-	+	-	+	+	+	-	-
$\bar{\alpha}_1$	$\tilde{\alpha}_2$	$\dot{\alpha}_3$	$\dot{\alpha}_4$	ρ_1	ρ'_2	$-\rho_3$	ρ'_4	+	+	-	-	-	+	-	+
$\bar{\alpha}_1$	α_2	$\tilde{\alpha}_3$	$\dot{\alpha}_4$	$-\rho'_1$	$-\rho'_2$	ρ'_3	ρ'_4	-	-	+	-	+	-	+	+

TABLE B.1: Table listing all 16 spherical mechanisms that can be linked to a generic Euclidean 4-vertex, and their fold angles.

Bibliography

- [1] P. Wang-Iverson, R. J. Lang, and M. Yim. *Origami 5: Fifth International Meeting of Origami Science, Mathematics, and Education*. A K Peters/CRC Press, New York, 2011. ISBN 9781439873502. doi:10.1201/b10971.
- [2] D. Lister. Some observations on the history of paperfolding in Japan and the West – a development in parallel. In K. Miura, editor, *Origami Science and Art: Proceedings of the Second International Meeting of Origami Science and Scientific Origami*, pages 511–524, Natick, Massachusetts, 1997. A K Peters.
- [3] Unknown. *Hidden Senbazuru Oriката* (“How to Fold a Thousand Cranes”). Japan, 1797.
- [4] Anonymous. *Aanhangzel van de volmaakte Hollandsche keuken-meid*. chapter: “de Wyze om allerhande Tafel-goed Konstig en cierlyk te vouwen”. Steven van Esvelde, Amsterdam, fourth edition, 1754.
- [5] (A) Wikipedia. *Hidden Senbazuru Oriката*. https://upload.wikimedia.org/wikipedia/commons/7/71/Hidden_Senbazuru_Orikata-S6-2.jpg. (B) F. J. Haffmans. *Uitvouwbare doopbrief, Duitsland, 1769*. <http://haffmansantiek.nl/peetvaderbrief-patenbrief-duitsland-18e-eeuw-doopsel.html>. (C) Brabants museum. *Kookboeken uit vroeger tijd*. <https://brabant-collectie.blogspot.nl/2014/12/kookboeken-uit-vroeger-tijd.html>.
- [6] C. Totman. *A history of Japan*. Wiley-Blackwell, 2nd edition edition, 2014. ISBN 9781405123594.

BIBLIOGRAPHY

- [7] N. Robinson. *The Origami Bible*. Collins & Brown Limited, London, 2004. ISBN 9781581805178.
- [8] R.C. Yates. *Geometrical Tools: A Mathematical Sketch and Model Book*. Educational Publishers, St. Louis, Missouri, 1949.
- [9] K. Kasahara and T. Takahama. *Origami for the Connoisseur*. Japan Publications, New York, New York, 1987. ISBN 9780870406706.
- [10] T. Kawasaki. On high dimensional flat origamis. In H. Huzita, editor, *Proceedings of the First International Meeting of Origami Science and Technology*, pages 131–141. Commune di Ferra and Centro Origami Duffusion, 1989.
- [11] T. C. Hull. On the mathematics of flat origamis. *Congressus numerantium*, pages 215–224, 1994.
- [12] J. Justin. Towards a mathematical theory of origami. In K. Miura, editor, *Origami Science and Art: Proceedings of the Second International Meeting of Origami and Scientific Origami*, pages 15–29, Natick, Massachusetts, 1997. A K Peters.
- [13] T. C. Hull. The combinatorics of flat folds: a survey. In T. C. Hull, editor, *Origami 3: Third International Meeting of Origami Science, Mathematics, and Education*, pages 29–38, Natick, Massachusetts, 2002. A K Peters.
- [14] E. D. Demaine and J. O’Rourke. *Geometric Folding Algorithms: Linkages, Origami, Polyhedra*. Cambridge University Press, Cambridge, 2007. doi:10.1017/cbo9780511735172.
- [15] J. Ginepro and T. C. Hull. Counting Miura-ori foldings. *J. Integer Seq.*, 17(2):3, 2014.
- [16] T. Tachi. Generalization of rigid foldable quadrilateral mesh origami. In A. Domingo Cabo and C. L. Lázaro Fernández, editors, *Symposium of the International Association for Shell and Spatial Structures (IASS): Evolution and Trends in Design, Analysis and Construction of Shell and Spatial Structures*, pages 2287–2294, Valencia, 2009. Editorial Universitat Politècnica de València.

- [17] R. J. Lang. Treemaker 4.0: A program for origami design, 1998. URL <http://www.langorigami.com/files/articles/TreeMkr40.pdf>.
- [18] T. Tachi. Origamizing polyhedral surfaces. *IEEE Trans. Vis. Comput. Graph.*, 16(2):298–311, 2010. doi:10.1109/tvcg.2009.67.
- [19] E. D. Demaine and T. Tachi. Origamizer: A practical algorithm for folding any polyhedron. In B. Aronov and M. J. Kat, editors, *33rd International Symposium on Computational Geometry (SoCG 2017)*, volume 77. Leibniz International Proceedings in Informatics, 2017. doi:10.4230/LIPIcs.SoCG.2017.34.
- [20] E. G. Rapp. Sandwich-type structural element, December 6 1960. US Patent 2,963,128.
- [21] L. C. Gewiss. Method for forming herringbone configurations for sandwich structures, March 18 1969. US Patent 3,433,692.
- [22] K. Miura. Zeta-core sandwich - its concept and realization. *ISAS report, University of Tokyo*, 37(6):137–164, 1972.
- [23] A. Lebé. From folds to structures, a review. *Int. J. Space Struct.*, 30(2): 55–74, 2015. doi:10.1260/0266-3511.30.2.55.
- [24] E. Baranger, P. Guidault, and C. Cluzel. Generation of physical defects for the prediction of the behavior of folded cores. In *Fourth European Congress on Computational Mechanics (ECCM IV)*, 2010.
- [25] E. Baranger, P. Guidault, and C. Cluzel. Numerical modeling of the geometrical defects of an origami-like sandwich core. *Compos. Struct.*, 93(10):2504–2510, 2011. doi:10.1016/j.compstruct.2011.04.011.
- [26] M. Schenk and S. D. Guest. Geometry of Miura-folded metamaterials. *Proc. Natl. Acad. Sci.*, 110(9):3276–3281, 2013. doi:10.1073/pnas.1217998110.
- [27] J. L. Silverberg, A. A. Evans, L. McLeod, R. C. Hayward, T. C. Hull, C. D. Santangelo, and I. Cohen. Using origami design principles to fold reprogrammable mechanical metamaterials. *Science*, 345(6197): 647–650, 2014. doi:10.1126/science.1252876.

BIBLIOGRAPHY

- [28] S. Waitukaitis, R. Menaut, B.G. Chen, and M. van Hecke. Origami multistability: From single vertices to metasheets. *Phys. Rev. Lett.*, 114(5):055503, 2015. doi:10.1103/physrevlett.114.055503.
- [29] S. Felton, M. Tolley, E. D. Demaine, D. Rus, and R. J. Wood. A method for building self-folding machines. *Science*, 345(6197):644–646, 2014. doi:10.1126/science.1252610.
- [30] A. Firouzeh and J. Paik. Robogami: A fully integrated low-profile robotic origami. *J. Mech. Rob.*, 7(2):021009, 2015. doi:10.1115/1.4029491.
- [31] C. D. Onal, M. T. Tolley, R. J. Wood, and D. Rus. Origami-inspired printed robots. *IEEE/ASME Trans. Mechatron.*, 20(5):2214–2221, 2015. doi:10.1109/tmech.2014.2369854.
- [32] K. Bertoldi, V. Vitelli, J. Christensen, and M. van Hecke. Flexible mechanical metamaterials. *Nat. Rev. Mater.*, 2(17066), 2017. doi:doi:10.1038/natrevmats.2017.66.
- [33] K. Miura. Method of packaging and deployment of large membranes in space. *ISAS report, University of Tokyo*, 618:1–9, 1985.
- [34] L. H. Dudte, E. Vouga, T. Tachi, and L. Mahadevan. Programming curvature using origami tessellations. *Nat. Mater.*, 15(5):583–588, 2016. doi:10.1038/nmat4540.
- [35] Arthur A. Evans, Jesse L. Silverberg, and Christian D. Santangelo. Lattice mechanics of origami tessellations. *Phys. Rev. E*, 92(1):013205, 2015. doi:10.1103/physreve.92.013205.
- [36] M. B. Amar and F. Jia. Anisotropic growth shapes intestinal tissues during embryogenesis. *Proc. Natl. Acad. Sci.*, 110(26):10525–10530, 2013. doi:10.1073/pnas.1217391110.
- [37] L. Mahadevan and S. Rica. Self-organized origami. *Science*, 307(5716):1740, 2005. doi:10.1126/science.1105169.
- [38] E. Couturier, S. C. Du Pont, and S. Douady. A global regulation inducing the shape of growing folded leaves. *PLoS ONE*, 4(11):e7968, 2009. doi:10.1371/journal.pone.0007968.

- [39] H. Kobayashi, B. Kresling, and J. F. V. Vincent. The geometry of unfolding tree leaves. *Proc. R. Soc. B*, 265(1391):147–154, 1998. doi:10.1098/rspb.1998.0276.
- [40] F. Haas and R. J. Wootton. Two basic mechanisms in insect wing folding. *Proc. R. Soc. B*, 263(1377):1651–1658, 1996. doi:10.1098/rspb.1996.0241.
- [41] T. Nojima. Origami modeling of functional structures based on organic patterns. Master’s thesis, Dept. of Engineering Science, Graduate School of Kyoto University, 2002.
- [42] V. Brunck, F. Lechenault, A. Reid, and M. Adda-Bedia. Elastic theory of origami-based metamaterials. *Phys. Rev. E*, 93(3):033005, 2016. doi:10.1103/physreve.93.033005.
- [43] A. E. Shyer, T. Tallinen, N. L. Nerurkar, Z. Wei, E. S. Gil, D. L. Kaplan, C. J. Tabin, and L. Mahadevan. Villification: how the gut gets its villi. *Science*, 342(6155):212–218, 2013. doi:10.1126/science.1238842.
- [44] F. Lechenault, B. Thiria, and M. Adda-Bedia. Mechanical response of a creased sheet. *Phys. Rev. Lett.*, 112(24):244301, 2014. doi:10.1103/physrevlett.112.244301.
- [45] S. Deboeuf, E. Katzav, A. Boudaoud, D. Bonn, and M. Adda-Bedia. Comparative study of crumpling and folding of thin sheets. *Phys. Rev. Lett.*, 110(10):104301, 2013. doi:10.1103/physrevlett.110.104301.
- [46] J. C. Maxwell. L. on the calculation of the equilibrium and stiffness of frames. *The London, Edinburgh, and Dublin Philosophical Magazine and Journal of Science*, 27(182):294–299, 1864. doi:10.1080/14786446408643668.
- [47] C. R. Calladine. Buckminster fuller’s “tensegrity” structures and Clerk Maxwell’s rules for the construction of stiff frames. *Int. J. Solids Struct.*, 14(2):161–172, 1978. doi:10.1016/0020-7683(78)90052-5.
- [48] D. A. Huffman. Curvature and creases: A primer on paper. *IEEE Trans. Comput.*, (10):1010–1019, 1976. doi:10.1109/tc.1976.1674542.
- [49] A. Kokotsakis. Über bewegliche polyeder. *Math. Ann.*, 107(1):627–647, 1933. doi:10.1007/bf01448912.

BIBLIOGRAPHY

- [50] H. Stachel. Flexible polyhedral surfaces with two flat poses. *Symmetry*, 7(2):774–787, 2015. doi:10.3390/sym7020774.
- [51] P. T. Barreto. Lines meeting on a surface: The “Mars” paperfolding. In K. Miura, editor, *Origami Science and Art: Proceedings of the Second International Meeting of Origami and Scientific Origami*, pages 343–359, Natick, Massachusetts, 1997. A K Peters.
- [52] T. Tachi. *Rigid Foldable Quadrilateral Mesh Origami Crease Pattern*. <https://www.flickr.com/photos/tactom/4053859811/>. Movie of the 3D-folding motion shown in: <https://www.flickr.com/photos/tactom/3725723541/>.
- [53] E. T. Filipov, T. Tachi, and G. H. Paulino. Origami tubes assembled into stiff, yet reconfigurable structures and metamaterials. *Proc. Natl. Acad. Sci.*, 112(40):12321–12326, 2015. doi:10.1073/pnas.1509465112.
- [54] E. T. Filipov, G. H. Paulino, and T. Tachi. Origami tubes with reconfigurable polygonal cross-sections. In *Proc. R. Soc. A*, volume 472, page 20150607. The Royal Society, 2016. doi:10.1098/rspa.2015.0607.
- [55] X. Liu, J. M. Gattas, and Y. Chen. One-dof superimposed rigid origami with multiple states. *Sci. Rep.*, 6:36883, 2016. doi:10.1038/srep36883.
- [56] K. Song, X. Zhou, S. Zang, H. Wang, and Z. You. Design of rigid-foldable doubly curved origami tessellations based on trapezoidal crease patterns. *Proc. R. Soc. A*, 473(2200):20170016, 2017. doi:10.1098/rspa.2017.0016.
- [57] T. A. Evans, R. J. Lang, S.P. Magleby, and L. L. Howell. Rigidly foldable origami gadgets and tessellations. *Roy. Soc. Open Sci.*, 2(9):150067, 2015. doi:10.1098/rsos.150067.
- [58] S. Waitukaitis and M. van Hecke. Origami building blocks: Generic and special four-vertices. *Phys. Rev. E*, 93(2):023003, Feb 2016. doi:10.1103/physreve.93.023003.
- [59] W. K. Schief, A. I. Bobenko, and T. Hoffmann. On the integrability of infinitesimal and finite deformations of polyhedral surfaces. In *Discrete differential geometry*, pages 67–93. Springer, 2008. doi:10.1007/978-3-7643-8621-4_4.

- [60] O. N. Karpenkov. On the flexibility of Kokotsakis meshes. *Geom. Dedicata*, 147(1):15–28, 2010. doi:10.1007/s10711-009-9436-4.
- [61] H. Stachel. A kinematic approach to Kokotsakis meshes. *Comput. Aided Geom. Des.*, 27(6):428–437, 2010. doi:10.1016/j.cagd.2010.05.002.
- [62] M. B. Pinson, M. Stern, A. Ferrero, C. Alexandra, T. A. Witten, E. Chen, and A. Murugan. Self-folding origami at any energy scale. *Nat. Commun.*, 8:15477, 2017. doi:10.1038/ncomms15477.
- [63] T. Tachi. Origamizer. URL <http://origami.c.u-tokyo.ac.jp/~tachi/software/>.
- [64] T. Tachi. Geometric considerations for the design of rigid origami structures. In *Proceedings of the International Association for Shell and Spatial Structures (IASS) Symposium*, volume 12, pages 458–460. Shanghai, 2010.
- [65] R. J. Lang. *Origami Design Secrets: Mathematical Methods for an Ancient Art*. AK Peters/CRC Press, New York, 2nd edition, 2011.
- [66] B. H. Hanna, J. M. Lund, R. J. Lang, S. P. Magleby, and L. L. Howell. Waterbomb base: a symmetric single-vertex bistable origami mechanism. *Smart Mater. Struct.*, 23(9):094009, 2014. doi:10.1088/0964-1726/23/9/094009.
- [67] F Lechenault and M Adda-Bedia. Generic bistability in creased conical surfaces. *Phys. Rev. Lett.*, 115(23):235501, 2015. doi:10.1103/PhysRevLett.115.235501.
- [68] J. L. Silverberg, J. Na, A. A. Evans, B. Liu, T. C. Hull, C. D. Santangelo, R. J. Lang, R. C. Hayward, and I. Cohen. Origami structures with a critical transition to bistability arising from hidden degrees of freedom. *Nat. Mater.*, 14(4):389–393, 2015. doi:10.1038/nmat4232.
- [69] E. D. Demaine, M. L. Demaine, V. Hart, G. N. Price, and T. Tachi. (non) existence of pleated folds: how paper folds between creases. *Graph. Combinator.*, 27(3):377–397, 2011. doi:10.1007/s00373-011-1025-2.
- [70] J. A. Faber, A. F. Arrieta, and A. R. Studart. Bioinspired spring origami. *Science*, 359(6382):1386–1391, 2018. doi:10.1126/science.aap7753.

BIBLIOGRAPHY

- [71] H. Yasuda and J. Yang. Reentrant origami-based metamaterials with negative poisson's ratio and bistability. *Phys. Rev. Lett.*, 114(18):185502, 2015. doi:10.1103/physrevlett.114.185502.
- [72] M. Schenk. *Folded Shell Structures*. PhD thesis, Clare College, University of Cambridge, 2011.
- [73] B. G. Chen and C. D. Santangelo. Branches of triangulated origami near the unfolded state. *Phys. Rev. X*, 8(1):011034, 2018. doi:10.1103/physrevx.8.011034.
- [74] S. Waitukatis, P. Dieleman, and M. van Hecke. Non-euclidean origami (unpublished). 2018.
- [75] L. Cedolin and Z. P. Băzant. *Stability of structures: Elastic, Inelastic, Fracture and Damage Theories*. World Scientific, 2010. doi:10.1142/9789814317047.
- [76] B. G. Chen, B. Liu, A. A. Evans, J. Paulose, I. Cohen, V. Vitelli, and C. D. Santangelo. Topological mechanics of origami and kirigami. *Phys. Rev. Lett.*, 116(13):135501, 2016. doi:10.1103/physrevlett.116.135501.
- [77] J. M. McCarthy and G. S. Soh. *Geometric Design of Linkages*, volume 11. Springer, 2nd edition, 2006. doi:10.1007/978-1-4419-7892-9.
- [78] C. H. Chiang. On the classification of spherical four-bar linkages. *Mech. Mach. Theory*, 19(3):283–287, 1984. doi:10.1016/0094-114x(84)90061-2.
- [79] F. L. Duditza and G. Dittrich. Die bedingungen für die umlauf-fähigkeit sphärischer viergliedriger kurbelgetriebe. *Industrie-Anzeiger*, 91(71):1687–1690, 1969. URL https://www.europeana.eu/portal/en/record/2020801/dmglib_handler_docum_2163009.html.

Samenvatting

Bij het vouwen van een vouwpatroon verandert men een tweedimensionaal plat materiaal in een vaak complexe driedimensionale vorm. Voorbeelden van zulke vouwpatronen kent men al eeuwenlang als ‘origami’, maar recent hebben materiaal- en natuurkundigen ontdekt dat sommige vouwpatronen in hun opgevouwen toestand exotische materiaaleigenschappen hebben. Een voorbeeld hiervan is het zogenaamde ‘Miura-ori’ vouwpatroon (zie hoofdstuk 1), dat in zijn opgevouwen toestand een negatieve Poisson-factor heeft, wat betekent dat het in meerdere richtingen krimpt als het wordt ingeduwd. Zulk soort eigenschappen hangen alleen af van de geometrie van het vouwpatroon en zijn dus toepasbaar op zowel hele kleine schaal, zoals voor insectenvleugels, als op hele grote schaal, zoals voor het opvouwen van zonnepanelen in satellieten. In het eerste gedeelte van dit proefschrift kijken we daarom naar de geometrie van vouwpatronen. In het bijzonder focussen we hier ons op vouwpatronen bestaande uit vier-vertices; dit zijn punten waar vier vouwlijnen samenkomen. Een enkele vier-vertex is het simpelste voorbeeld van een vouwpatroon dat kan worden gevouwen zonder het materiaal te verbuigen, en heeft een opmerkelijke eigenschap: ondanks zijn enkele vrijheidsgraad heeft hij twee verschillende vouwbewegingen. We maken gebruik van deze eigenschap, en laten zien hoe we willekeurig grote vier-vertex vouwpatronen kunnen ontwerpen die op twee of meer manieren op kunnen vouwen. Dit is in tegenstelling tot andere methodes, die vouwpatronen produceren die slechts op één manier vouwen. In het tweede gedeelte bekijken we enkele vier-vertices, en laten we een robuuste methode zien om een vertex te maken met drie energiminima, welke corresponderen met drie verschillende stabiele vouwtoestanden. Ook dit is in tegenstelling tot andere methodes, die slechts bistabiele vertices of patronen genereren.

De meeste vouwpatronen die bestaan uit vier-vertices zijn periodiek, en worden gemaakt door een enkele eenheidscel steeds te kopiëren, waardoor het patroon willekeurig groot kan worden gemaakt. Deze patronen voldoen aan de zogenaamde ‘starre-vouw voorwaarde’ die zegt dat de panelen tussen de vouwlijnen in –in dit geval vierhoeken– niet mogen ver-

vormen tijdens de vouwbeweging. Een dergelijk vouwpatroon kan beschouwd worden als een mechanisme, bestaande uit starre vierhoekige panelen verbonden door vrij bewegende scharnieren. Wij laten in dit werk een methode zien die op combinatorische wijze star-vouwbare vier-vertex vouwpatronen genereert, die op meer dan één manier kunnen vouwen, en bovendien aperiodiek kunnen zijn. We doen dit door vouwpatronen op te bouwen uit puzzelstukjes. Elk van deze puzzelstukjes representeert een minimaal vier-vertex vouwpatroon waarbij de vier hoeken van een vierhoek allen worden bezet door een vier-vertex. Door gebruik te maken van een set vertices die door symmetrie aan elkaar gerelateerd zijn, kan elk puzzelstukje op tenminste twee verschillende manieren star opvouwen. Daarnaast zijn deze puzzelstukjes zo ontworpen dat twee of meer aan elkaar passende puzzelstukjes automatisch leiden tot een star-vouwbaar patroon. De resulterende combinatorische vouwpatronen zijn in te delen in klassen, aangezien sommige puzzelstukjes wel samen binnen één en hetzelfde patroon kunnen voorkomen, en sommige niet. We tellen de hoeveelheid vouwpatronen van een bepaalde grootte binnen elke klasse, en het aantal mogelijke vouwbewegingen per patroon, dat varieert per klasse.

Hierna focussen we ons op een bijzondere klasse die precies twee vouwbewegingen heeft, ongeacht de grootte van het patroon. In deze klasse kan de vorm van beide vouwbewegingen onafhankelijk van elkaar aangepast worden, door specifieke puzzelstukjes te kiezen aan de zij- en bovenkant van het patroon. We demonstreren deze ontwerpstrategie door twee plastic vellen met identiek lasergesneden vouwpatronen op te vouwen tot twee verschillende vormen. Dit is voor zover wij weten de eerste (experimentele) demonstratie van een dergelijk tweevoudig vouwbaar vouwpatroon.

In het tweede gedeelte van dit proefschrift kijken we naar het gedrag van de enkele vier-vertex. Onze aandacht gaat in het bijzonder uit naar niet-euclidische vier-vertices. Dit zijn vertices die niet gevouwen kunnen worden uit een vlak stuk materiaal, omdat de vier hoeken tussen de vier lijnen van de vertex niet optellen tot 360 graden, maar juist meer, óf minder. Dit zorgt ervoor dat de twee vouwbewegingen –die voor een euclidische vier-vertex samenkomen in de vlakke toestand– van elkaar worden gescheiden door de starre-vouw voorwaarde. Deze scheiding maakt het onmogelijk te wisselen van vouwbeweging zonder de panelen te verbuigen. Echter, het is nog wel mogelijk van vouwbeweging te wisselen door de vertex dóór de vlakke toestand heen te duwen. Effectief hebben we zo

een energiebarrière gecreëerd tussen de twee vouwbewegingen, aangezien het materiaal van de vertex in de praktijk verbogen moet worden.

We laten zien hoe deze energiebarrière gebruikt kan worden om vier-vertices te ontwerpen die drie stabiele vouwtoestanden hebben door het toevoegen van één enkele torsiebeer op één van de vouwen. Deze beer zorgt ervoor dat op één van de twee vouwbewegingen twee stabiele vouwtoestanden ontstaan, die corresponderen met een globaal minimum in de energie. Op de andere vouwbeweging ontstaat daarentegen een lokaal minimum, dat stabiel is mits de bovengenoemde energiebarrière groot genoeg is. We geven een experimentele demonstratie van een dergelijk systeem door niet-euclidische vier-vertices te 3D-printen van plastic, en op een van de vouwen één enkele torsiebeer te plaatsen. We laten zien dat de verkregen vertices inderdaad drie stabiele vouwtoestanden hebben. Als laatste vergelijken we de theoretische energiecurves van de vouwbewegingen met experimentele energiecurves. Dit doen we door de geprinte vertices te testen in een torsietester, waarmee we het krachtmoment en de energie meten die nodig zijn om van de ene stabiele vouwtoestand naar de andere te schakelen.

De ontwerpstrategieën gepresenteerd in dit proefschrift kunnen worden gemaakt door gebruik te maken van nieuwe, computergestuurde productietechnieken, zoals lasersnijders en 3D-printers. Deze technieken kunnen worden toegepast om patronen te maken met vouwen ter grootte van enkele centimeters, zoals in dit proefschrift, maar zijn ook toe te passen op de kleinere schaal van micro- en millimeters. Daarmee komen materialen met geheel nieuwe functionaliteiten binnen handbereik.

Summary

When folding a crease pattern we change a two-dimensional, flat material into an often complex three dimensional shape. Examples of such crease patterns have been known for centuries as ‘origami’. Recently however, material scientists and physicists have discovered that some crease patterns have exotic material properties when folded. An example of this is the so called ‘Miura-ori’ pattern (see chapter 1), which has a negative Poisson’s ratio in its folded configuration, which means it shrinks in multiple directions when squeezed. Such properties depend solely on the geometry of the crease pattern, and can be applied on the very small scale, such as in insect wings, and on the very large scale, such as in solar panels for space-satellites. In the first part of this thesis we therefore study the geometry of folding patterns. Specifically, we focus on crease patterns consisting entirely of four-vertices; these are points where four fold lines come together. A single four-vertex is the simplest example of a foldable crease pattern that can be folded without bending the material in between the folds, and has a remarkable property: despite its single degree of freedom, it has two distinct folding motions. We make use of this property, and show how to design arbitrarily large four-vertex crease patterns, which can fold into two or more shapes. This is in contrast to other design methods, which produce patterns that can only fold into one specific shape. In the second part of this thesis, we study single four-vertices, and show a robust method to obtain four-vertices with three energy minima, which correspond to three different stable folded configurations. This too is in contrast to other experimental methods, which can only generate bistable vertices or patterns.

Most crease patterns consisting of four-vertices are periodic, and are designed by copying a single unit cell, which allows for the creation of arbitrarily large crease patterns. These crease patterns satisfy the so called ‘rigid-folding’ condition, which says that the panels in between the fold lines –quadrilaterals in this case– are not allowed to deform during the folding process. Such a crease pattern can be considered as a mechanism, consisting of rigid quadrilateral panels connected by freely moving

hinges. In this work we show a combinatorial method capable of generating arbitrarily large *aperiodic* crease patterns, which also have multiple distinct folding motions. We do this by representing crease patterns by puzzle pieces; each of these puzzle pieces represents a minimal four-vertex folding pattern where the four corners of a quadrilateral are each occupied by a four-vertex. By using a set of vertices that are related to each other by symmetry, the crease pattern associated with each puzzle piece can fold into at least two different configurations. Furthermore, these puzzle pieces are designed such that two (or more) puzzle pieces that fit together, automatically lead to a rigidly foldable pattern. The resulting combinatorial fold patterns can be categorized into different classes, since some puzzle pieces can appear within one and the same pattern, and some can not. We count the number of crease patterns of a given size within each class, and the number of folding motions for each pattern, which varies per class.

We then focus on a special class, which has exactly two folding motions, regardless of the size of the pattern. In this class the shape of both folding motions can be tuned independently of each other, by choosing which puzzle pieces are at the top- and left-side of the pattern. We demonstrate this design strategy by laser cutting two plastic sheets with identical crease patterns, and folding them up into two different shapes. As far as we know, this is the first (experimental) demonstration of such a bipotent folding pattern.

In the second part of this thesis we study the behavior of single four-vertices. Specifically, we focus our attention on non-euclidean four-vertices. These are four-vertices which can not be folded from a flat piece of material, as the four angles between the four fold lines of the vertex add up to less (or more) than 360 degrees. Because of this, the two folding branches of the single four-vertex –which come together at the flat configuration for a euclidean four-vertex– are disconnected from each other by the rigid folding condition. This separation makes it impossible to switch between the two folding branches without bending the panels. However, it is still possible to switch from folding branches by forcing the vertex through the flat configuration. Effectively we therefore created an energy barrier between the two folding branches, since the material of the vertex has to be bent.

We show that this energy barrier can be harnessed to design four-vertices with three stable configurations by adding a single torsional spring to one of the folds. This spring ensures that two stable configu-

rations are created on one of the two folding branches, which both correspond to a global energy minimum. On the other folding branch, we find a single stable configuration, corresponding to a local energy minimum. This minimum is stable, provided that the energy barrier mentioned above is high enough. We give an experimental demonstration of such a system by 3D-printing non-euclidean four-vertices of plastic, and placing a single torsional spring on one of the folds. We show that the resulting vertices indeed have three stable configurations. Finally, we compare the theoretical energy curves of the folding branches with experimental energy curves. We do this by testing the vertices in a torsion-tester, which can measure the torque and energy required to switch from one stable configuration to another.

The design strategies presented in this thesis can be applied by making use of new, computer-controlled manufacturing techniques, such as laser cutters and 3D-printers. These techniques can be applied to make patterns on the scale of centimeters, such as in this thesis, but are also applicable on the smaller scale of micro- and millimeters. This puts materials with completely novel functionalities within reach.

Publication List

Published work presented in this thesis:

- P. Dieleman, N. Vasmel, S. Waitukaitis, and M. van Hecke. ‘Design of Pluripotent Origami’, *in preparation*.
- S. Waitukaitis, P. Dieleman, and M. van Hecke. ‘Multistable Mechanisms of Non-Euclidean 4-vertex Origami’, *in preparation*.

Other published work:

- M.K. Jawed, P. Dieleman, B. Audoly, and P.M. Reis, ‘Untangling the Mechanics and Topology in the Frictional Response of Long Overhand Elastic Knots’, *Physical Review Letters*, **115**, 118302 (2015).

Curriculum Vitae

I was born in Rotterdam on the 31st of May in 1990, and grew up in the town of Oostvoorne, to the west of Rotterdam. I received my secondary education at the Scholengemeenschap Helinium, in Hellevoetsluis.

After graduating, I enrolled in the BSc program of Physics at *Leiden University*. During my third year, I followed courses at the *Erasmus University* to complete a pre-master program for *Econometrics & Management Science* as my minor. I finished my BSc program with a thesis on the measurement of the electrical conductance of a monolayer of gold nanoparticles in a hexagonal array, in the group of Prof. dr. ir. S. J. van der Molen.

Upon finishing my BSc, I continued in the MSc program *Research in Experimental Physics* at *Leiden University*. I spent seven months in the research group of Prof. dr. Martin van Hecke, where I used density matched hydrogel spheres floating in water to investigate the jamming transition. After this, I went abroad, to the group of Prof. dr. Pedro Reis at the *Massachusetts Institute of Technology*, where I investigated the relation between the mechanics, friction, and topology of knots. In July 2014, I received my MSc diploma cum laude.

Upon returning to the Netherlands, I continued in the group of Prof. dr. Martin van Hecke as a PhD candidate. Here I studied the folding behavior of four-vertices and patterns of four-vertices, the results of which are presented in this thesis. The research in this work has been performed at the Leiden Institute of Physics as well as the NWO-I institute AMOLF, as part of the dual appointment of Prof. dr. Martin van Hecke. I presented my work at various international conferences: the APS March meetings of 2015, 2016, 2017, and 2018 (USA), the MRS Fall meeting 2015 (Boston, USA), ESMC9 2015 (Madrid, Spain), Metamaterials 2015 (Oxford, UK), and the 2015 *Folding and Creasing of Thin Plate Structures* workshop at *ESPCI* (Paris, France).

Throughout my PhD and MSc studies I have assisted in teaching the courses of *Experimentele Natuurkunde 2* (fall 2014, 2015, 2017, and 2018), *Experimentele Natuurkunde 3* (spring 2015), *Fysica van Energie* (spring 2013), *Wiskunde Aan-sluiting* (fall 2012), and *Inleiding Natuurkunde* (fall 2012). In addition, I was employed by the university as a 1-to-1 tutor for a first year student, and worked at *Stichting Studiebegeleiding Leiden* during my BSc and MSc studies, where I assisted in teaching mathematics to high-school students.

After my PhD, I want to apply my research and analytical skills to challenging contemporary questions, in a position in industry.

Acknowledgments

This work would not have come together without the help and support of many people. First of all, I would like to thank my supervisor, Martin van Hecke. Thanks for giving me the opportunity to start this endeavor, letting me find my own way, but also pushing me when necessary. In addition I would like to thank two of my close collaborators: Scott Waitukaitis, who patiently answered many of my questions about origami, and Niek Vasmel, whose mathematical skill set gave us invaluable insight into some of the problems in this thesis.

Furthermore I would like to thank all the people that are part of the Mechanical Metamaterials group in both Leiden and AMOLF: Anne Meeussen, Luuk Lubbers, Nitin Singh, Song-Chuan Zhao, as well as those who left before me: Bastiaan Florijn, Merlijn van Deen, Matthieu Labousse, Corentin Coulais, Geert Wortel, and all the students who were part of the group throughout these last four years. Thanks for the scientific discussions and the enjoyable work atmosphere. A special thanks should go to the support staff, in particular: Jeroen Mesman-Vergeer, who taught me how to draw 3D objects in Autodesk and helped me with the many 3D prints I made during my PhD, Dion Ursem, who lasercut the sheets in chapter 4 and made the custom mounts for the experiments in chapter 5, and Daniëlle Duijn-ter Veer and Ellie van Rijsewijk, who helped to overcome some of my organizational shortcomings.

I would also like to thank the people of the soft matter community in Leiden and AMOLF, for the many interesting conversations during coffee and lunch breaks, all the people of the Kraft-group, and in particular Vera Meester, who spent three autumns together with me, supervising first-year students during their first open practicals.

Verder zou ik langs deze weg enkele dierbaren willen bedanken voor hun ondersteuning. Ten eerste mijn (stief)ouders, Zaïre, John, Wim, en Klazien. Bedankt dat je me altijd mijn eigen weg hebt laten kiezen. Klazien, je wordt gemist. Ook wil ik bedanken: mijn broer en zus, Lars en Roos, de rest van mijn familie, die te groot is om iedereen bij naam te noemen, en de vrienden waarmee ik tien jaar geleden naar Leiden vertrok, Frits, Onur, en Yasir. Als laatste, Melissa, jouw plotselinge verschijning in mijn leven kwam op precies het juiste moment, en heeft me geholpen positiever te kijken naar mijn eigen werk.